Florida Institute of Technology

Scholarship Repository @ Florida Tech

Theses and Dissertations

12-2019

Remote Sensing, Modeling, and Spectroscopic Studies of Gigantic Jets and Lightning Leaders

Levi Boggs

Remote Sensing, Modeling, and Spectroscopic Studies

of Gigantic Jets and Lightning Leaders

by

Levi Boggs

Master of Science
Florida Institute of Technology
Aerospace, Physics, and Space Sciences Department
2016

Bachelor of Science
University of Nebraska
Department of Earth and Atmospheric Science
2014

A dissertation
submitted to the College of Engineering and Science
at Florida Institute of Technology
in partial fulfillment of the requirements
for the degree of

Doctorate of Philosophy
in
Aerospace, Physics, and Space Sciences Department

Melbourne, Florida
December, 2019

We the undersigned committee
hereby approve the attached dissertation

Remote Sensing, Modeling, and Spectroscopic Studies
of Gigantic Jets and Lightning Leaders by Levi Boggs

_____

Hamid K. Rassoul, Ph.D.
Distinguished University Professor
Aerospace, Physics and Space Sciences
Committee Chair

_____

Ningyu Liu, Ph.D.
Professor
Physics and Space Science Center
University of New Hampshire

_____

Amitabh Nag, Ph.D.
Assistant Professor
Aerospace, Physics and Space Sciences

_____

Jeremy Riousset, Ph.D.
Assistant Professor
Aerospace, Physics and Space Sciences

_____

Steven Lazarus, Ph.D.
Professor
Meteorology

_____

Michael Splitt, M.S.
Assistant Professor
Aeronautics

_____

Daniel Batcheldor, Ph.D.
Professor and Department Head
Aerospace, Physics, and Space Sciences

ABSTRACT

Title:

Remote Sensing, Modeling, and Spectroscopic Studies

of Gigantic Jets and Lightning Leaders

Author:

Levi Boggs

Major Advisor:

Hamid K. Rassoul, Ph.D.

This dissertation focuses on four interrelated investigations with the ultimate goal of better understanding electrical phenomena in the lower and upper atmosphere. The four investigations utilized observations and data analysis for electrical discharges occurring in the troposphere, such as cloud-to-ground and intracloud discharges, and discharges occurring in the stratosphere/lower ionosphere, known as gigantic jets. The observations are from ground-based high-speed cameras and lightning locating systems, space-borne lightning imagers, and remote and in-situ meteorological instrumentation. Numerical modeling was also performed to study the lightning associated with gigantic jets by using a stochastic lighting propagation model. Finally, this dissertation focuses on the design and construction of a high-speed spectrograph that can be used for studying lightning and transient luminous events. Preliminary observations of lightning leaders using this state-of-art spectrograph will be presented and analyzed to characterize its performance for future observation campaigns.

Table of Contents

List of Figures

List of Tables

Acknowledgements

Throughout my time at as graduate student working on my masters and PhD at the Florida Institute of Technology, I have made countless colleagues and friends that have made large impacts on my life and career. From classmates I've studied with, to undergraduate students I've collaborated with, to professors I've learned from, the list is long. Undoubtedly, one individual who has had a tremendous impact is my academic research co-advisor Dr. Ningyu Liu. From day one, Ningyu took a chance on me to be his formal graduate student, even though my undergraduate grades were not the best and my undergraduate degree wasn't in Physics. For this I am extremely grateful, as other physics institutions were not so keen to accept me. Ningyu was always very encouraging with me, especially in terms of performing research and pursuing my own ideas. From his excellent guidance I have learned a tremendous amount over the last $5 \frac{1}{2}$ years, from creating meaningful research questions, to writing technically sound research papers, to describing complex topics in simple terms. He provided me with the research freedom many academics would envy, all while providing valuable feedback and fully supporting the ideas I came up with. Near the beginning of my graduate career, I'll never forget the time when he asked me to be the lead author on what would become my first peer-reviewed journal article. That was an exciting moment for me and a testament of

how supportive and confident Ningyu is with his graduate students. To this day we still collaborate on research, even though we are in different locations, and I look forward to continued collaboration on future projects.

Another person I am extremely grateful for is my other academic research co-adivsor, Dr. Hamid K. Rassoul. It's not every day a PhD student gets two research advisors, but if you play your cards right, you can end up with two that are experts in their field! It is hard to ignore Hamids intense and insatiable curiosity for science and his yearning for knowledge, something that I inherited from him. He is truly a master of his craft, and finds delight in deriving any complex equation he can get his hands on. This was a fantastic quality to have in a research advisor, as this made my education in physics enjoyable and something I looked forward to. Like Ningyu, Hamid always encouraged me to pursue my research ideas and was very supportive on any work I completed. One of the most important things I learned from him was to commit and perform good science, and everything else will fall into place. He also taught me the inner workings of academia and how to write effective proposals, which is something that I find to be a critical component of any graduate students career that seems to often be overlooked.

I have also been fortunate to have a PhD committee that has been very engaging in research and very open to collaborations. In my opinion, this led to important interdisciplinary research between the disciplines of atmospheric science, electrical engineering, and numerical modeling. This interdisciplinary work resulted from many interesting meetings and research opportunities with Dr. Steven Lazarus and Michael Splitt, who are experts in atmospheric science and meteorology. Dr. Amitabh Nag provided keen insight into the electrical nature of lightning discharges and the instrumentation used to measure their signals, while Dr. Jeremy Riousset

taught me the details of numerical modeling and how that relates to atmospheric electricity. Jeremy was another very influential figure in my academic career, and provided very helpful insight into the electrical nature of storms. He also taught me how to approach complex problems, and to think critically about first principles. His enthusiasm and passion for teaching and mentoring is something that I will remember throughout the rest of my career.

Finally, I would like to thank all my fellow graduate students at Florida Tech that made my graduate career so rewarding and fun. This includes students from the Geospace Physics Lab studying lightning and space weather, to astrophysics students studying the formation of black holes, to particle physicists learning how subatomic particles interact. To all of you, I will always remember our great times and conversations.

Chapter 1

Introduction and Scope

This dissertation focuses on the remote sensing and modeling of gigantic jet lightning and its parent thunderstorms, as well as high-speed spectroscopy of natural lightning leaders and return strokes. It combines rigorous data analysis of atmospheric and lightning datasets, numerical modeling, and instrumentation construction. In this chapter, the necessary background information to understand the basics of thunderstorms, lightning, and gigantic jets is presented. In closing, this chapter will introduce the scientific questions proposed by this research and how they were addressed for the completion of this dissertation.

1.1 Classic Thunderstorm Charge Structure and Lightning

Studies have found that thunderstorms commonly exhibit a tripolar thunderstorm charge structure, with upper positive, middle negative, and lower positive charge

[*Williams*, 1989]. The upper and middle charge regions usually dominate and are approximately the same size, with the lower charge region being much smaller in magnitude. An example of this charge structure is shown in Figure 1.1, with electric field lines overlaid. This figure is an idealized model of a thundercloud charge structure, with the charge regions shown as flat cylindrical plates. Another example of a tripolar charge structure is shown in Figure 1.2, which was derived from very high frequency (VHF) mapping measurements of lightning. Common altitudes for the upper positive charge region are between 8-12 km altitude, while the middle negative charge region resides around 6-8 km altitude. The lower positive charge region, if present, will reside between 4-5 km altitude. This vertical
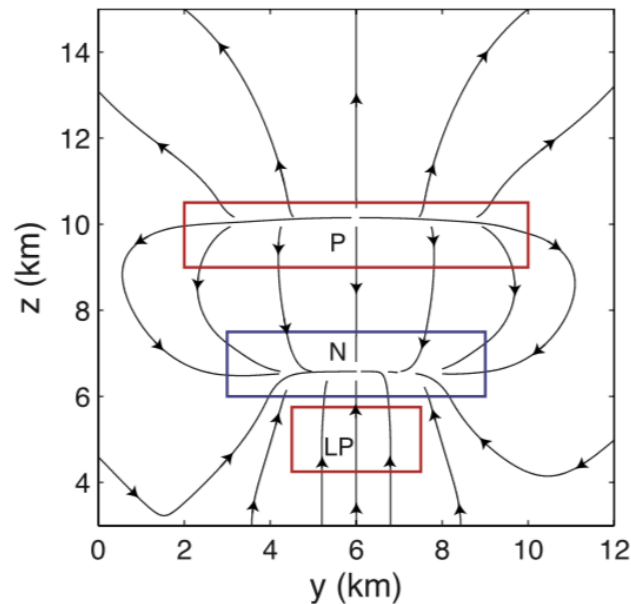
Figure 1.1: Generalized thunderstorm charge structure with electric field lines overlaid. The red rectangles represent the upper and lower positive charge regions, and the blue rectangle represents the middle negative charge region. This figure is taken from *Riousset et al.* [2007].

distribution of charges is typical of mid-latitude charge structures, but tropical and

oceanic thunderstorms can have the upper positive charge region extend to 15 km altitude or even higher [*López et al.*, 2019]. Also present are screening charge layers that form on the thundercloud cloud boundaries [*Krehbiel et al.*, 2008; *Riousset et al.*, 2010b]. These screening layers form due to the conductivity gradient between the cloud and open air. The cloud acts as a good insulator, with open air being more conductive, and thus charges attach and accumulate to the cloud boundary. But, due to the vertical conductivity gradient in the open atmosphere, screening charge layers at upper altitudes form more quickly than layers at lower altitudes. Thus, the screening layer at the upper cloud boundary forms the quickest, which has implications to escaped lightning discharges at cloud top. Typical charge densities for thundercloud charge regions have been found to be a few tenths to a few nCm^{-3} [*Winn et al.*, 1978, 1981; *Byrne et al.*, 1983].
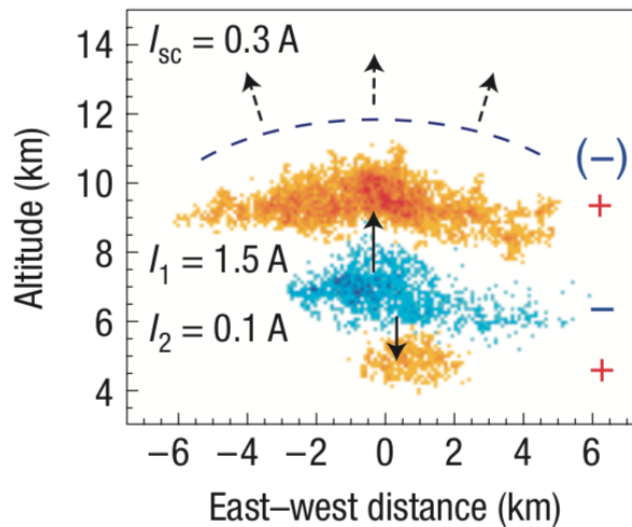
Figure 1.2: Thunderstorm charge structure obtained from VHF lightning mapping observations. The orange (blue) regions are the positive (negative) charge regions. This figure taken from *Krehbiel et al.* [2008].

Due to lightning being an electrical discharge that forms due to thundercloud

charge, the thunderstorm charge structure plays an important role in forming the different types of lightning discharges. Although the charge structure described above is the most common charge structure, the thunderstorm charge structure can take on different forms, depending on the environment and stage in the thunderstorms lifetime. Figure 1.3 shows different types of lightning flashes and their respective thunderstorm charge structures from modeling studies. Figure 1.3a shows an intracloud flash (IC) that occurs at low altitudes from a charge structure called a negative dipole. This flash occurs between a middle negative charge region
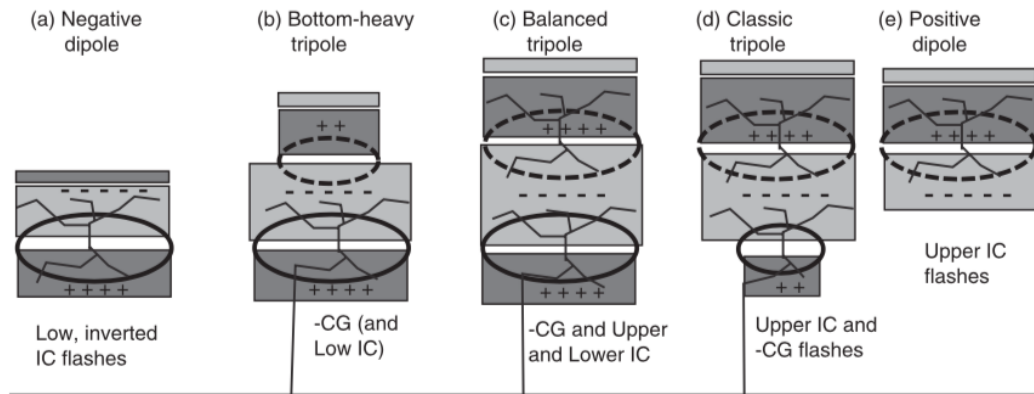
Figure 1.3: Fractal model simulations of different types of lightning associated with different charge structures. The dark gray (light gray) regions represent positive (negative) charge. The dashed (solid) oval represents areas where graupel is charged negatively (positively). This figure is taken from *Mansell et al.* [2010].

and a similar sized lower positive charge region, producing an inverted IC flash, which transfers negative charge downward (-IC). Figure 1.3b shows a bottom-heavy dipole charge structure that produces -IC discharges, similar to Figure 1.3a, but also with negative cloud-to-ground discharges (-CG), which are flashes that initiate between the middle negative and lower positive charge regions and continue propagating toward ground, transferring negative charge to the surface. Here the upper positive charge and upper negative screening layer are also present, but the middle

negative and lower positive charges dominate. Next, is a balanced tripole charge structure, shown in Figure 1.3c. This has the upper positive, middle negative, and lower positive charge regions all being similar sized, with a strong upper negative screening layer. Common discharges from this charge structure are -CG and -IC, but also with positive intracloud discharges (+IC), which are flashes between the middle negative and upper positive charge regions. Figure 1.3d shows the classic tripolar charge structure described in the paragraph above. The middle negative and upper positive charge regions are similar sized and dominate. Majority of the lightning is +IC and -CG. These two types of flashes dominate in most thunderstorms. Finally, Figure 1.3e shows a positive dipole charge structure, with similar sized upper positive and middle negative charge regions, and a strong negative screening layer. This produces mostly +IC discharges. These different types of thundercloud charge structures form due to different meteorological environments, and it is possible that a single storm can produce many of these charge structures during its lifetime. But, the duration of each charge structure for a single storm may be drastically different. The goal of this overview is to demonstrate that the thunderstorm charge regions, including their size, and location, dictate what type of lightning flash will occur. This has implications to how upward discharges known as gigantic jets are produced, which is a focus of this dissertation.

1.2   The Lightning Discharge

The bright flash of light that most people associate with lightning is only a small part of the entire process of a lightning flash, and is called the lightning return stroke. Before this, a very hot (thousands of Kelvins), conductive, ionized channel

[*Bazelyan and Raizer*, 1998, 2000; *Gallimberti et al.*, 2002; *Uman*, 2001] is formed that connects two regions of different electric potentials, allowing the return stroke to take place. This ionized channel is called a lightning leader. It is formed after the thunderstorm electric field exceeds a certain threshold [*Marshall et al.*, 1995; *Dwyer et al.*, 2003; *Behnke et al.*, 2005] and propagates at speeds of 10^4 m s^{-1} to 10^6 m s^{-1}, transferring charge between different charge regions in the cloud, or between a thundercloud charge region and the ground or the ionosphere. Below, a detailed description of a -CG discharge is provided.
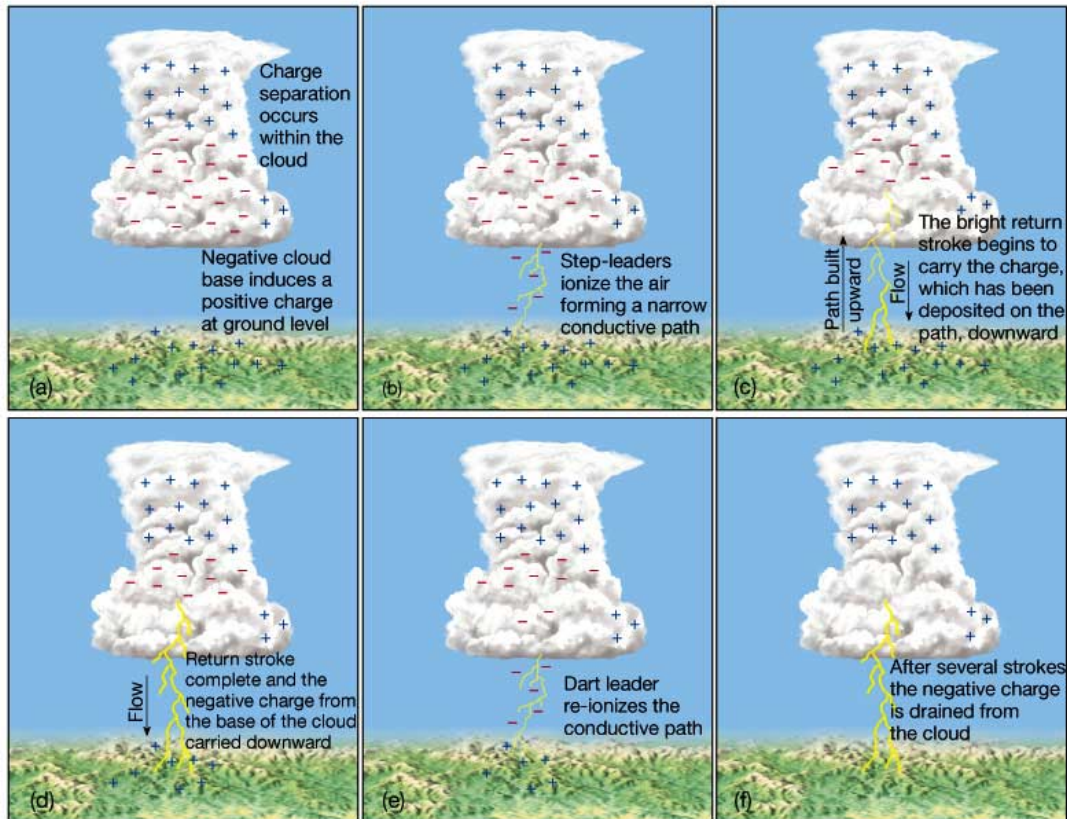
Figure 1.4: Overview of the cloud-to-ground lightning process.

A -CG discharge occurs between the middle negative charge region in a thundercloud and the ground. This process begins with thundercloud charge being

6

generated in the thunderstorm, commonly thought to be from the non-inductive riming of graupel by supercooled water, which, for the sake of simplicity, forms a middle negative and upper positive charge region, shown in Figure 1.4a. After the thundercloud electric field exceeds the breakdown threshold beneath the middle negative charge region, a negative stepped leader forms, propagating toward the ground (Figure 1.4b). The negative stepped leader ionizes the air, forming a thin, hot, conductive path between the cloud and the ground. When the leader reaches the ground, a bright return stroke occurs, which begins from the ground and propagates upward to the cloud, neutralizing the charge along the negative leader channel (Figure 1.4c). This is the bright flash commonly associated with lightning. The return stroke process results in net negative charge being transferred from the cloud to the ground (Figure 1.4d). Most -CG flashes have several return strokes, which are made possible by dart leaders. A dart leader is similar to a leader, but it is usually not stepped, and is faster than a stepped leader (10^6 m s^{-1} compared to 10^5 m s^{-1}). After the first return stroke, the dart leader re-ionizes the conductive path from the previous stroke, shown in Figure 1.4e. When the dart leader connects with ground, another return stroke ensues. This process usually repeats a few times for a typical -CG discharge.

1.3 Gigantic Jet Discharges

Gigantic jets (GJs) are a type of transient luminous event (TLE) above thunderstorms [*Pasko*, 2010; *Liu et al.*, 2015b]. They are electrical discharges that exit the tops of thunderstorms and reach 70-90 km altitudes [*Pasko et al.*, 2002; *Su et al.*, 2003], capable of transferring tens to hundreds of coulombs of charge between the

thundercloud and the ionosphere [*Cummer et al.*, 2009; *Lu et al.*, 2011; *Liu et al.*, 2015c]. Figure 1.5 shows images several gigantic jet discharges. Figure 1.5a is from low-light video footage from citizen scientist Frankie Lucena (reported on in *Boggs et al.* [2019]) and 1.5b is from *Su et al.* [2003]. The color images shown in 1.5c, d are from amateur photographers. GJs are unique in that they are a direct electrical coupling between the troposphere and lower ionosphere. They usually last longer than CG discharges, with continuing currents (CC) of up to several hundred ms.
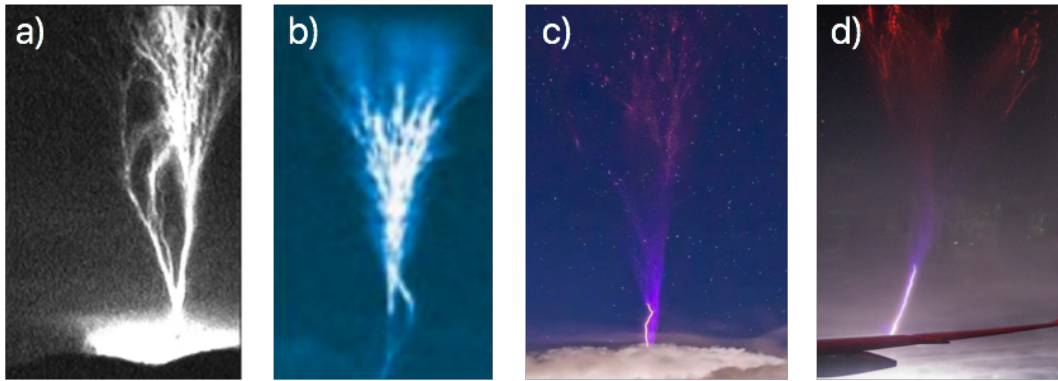
Figure 1.5: Gigantic jet video observations. a) Black and white low-light video from *Liu et al.* [2015c]. b) low-light video from *Pasko et al.* [2002]. c) a long exposure color photograph from an amateur photographer in Australia and d) a long exposure color photograph from a passenger on an airline.

Previous modeling studies have shown that for a normal polarity thunderstorm that has a classic tripolar charge structure, gigantic jets can be initiated between the middle negative and upper positive charge regions as a normal intracloud flash, with the negative leader subsequently escaping the upper positive charge [*Krehbiel et al.*, 2008; *Riousset et al.*, 2010b]. This is shown in Figure 1.6, which were simulated using a stochastic fractal lightning model. This formulation is

consistent with the observed gigantic jets being predominately of negative polarity and transferring negative charge to the ionosphere [*Pasko et al.*, 2002; *Su et al.*, 2003; *Cummer et al.*, 2009; *Lu et al.*, 2011; *Soula et al.*, 2011; *Huang et al.*, 2012; *Liu et al.*, 2015b,c]. In order for the negative leader to escape the cloud, the upper positive charge must be weakened - likely by mixing with the upper negative screening charge layer [*Krehbiel et al.*, 2008; *Riousset et al.*, 2010b]. This creates a charge imbalance between the main thundercloud charge regions, enabling the leader to escape.
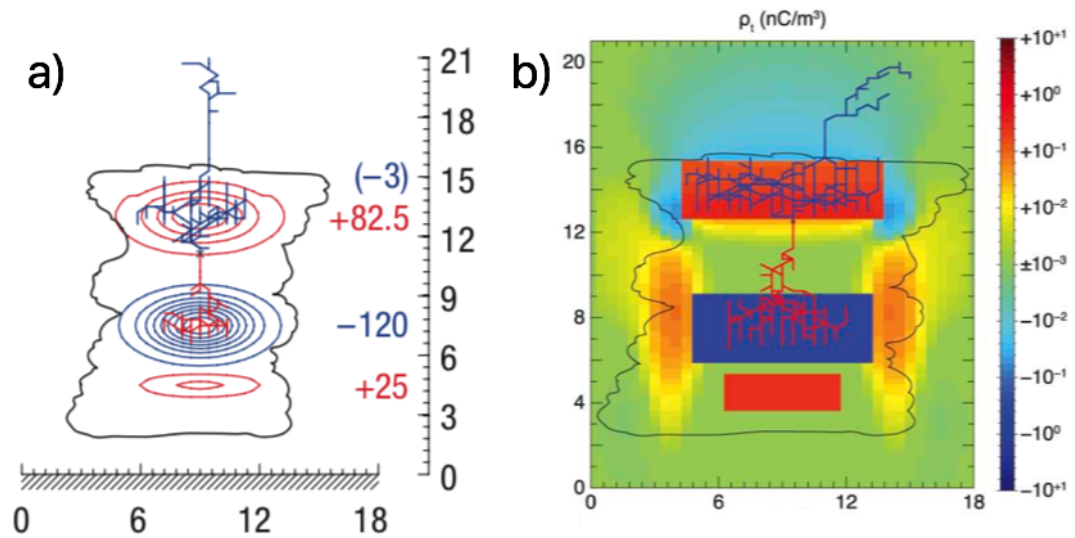
Figure 1.6: Modeling results of gigantic jet storms. a) Positive (negative) charge and leaders represented with red (blue) colors from *Krehbiel et al.* [2008]. b) same color scheme as in a) only with additional screening charge from *Riousset et al.* [2010b] The distance scales are listed in kilometer and the charge in a) is in Coulombs.

The charge structures used in those modeling studies were not formulated from direct observations of gigantic jet producing convection, but were assumed to resemble a classic tripolar charge structure [*Krehbiel*, 1986; *Williams*, 1989]. They featured a wide, weakened upper positive charge region over a similar sized middle

negative charge region [*Krehbiel et al.*, 2008; *Riousset et al.*, 2010b], augmented by a small lower positive charge region. The simulations were conducted with the top boundary set right above the cloud top, and their purpose was to determine if a lightning leader from a normal intracloud flash could escape the upper charge region. They did not answer where this leader would propagate once it left the upper charge and whether it would form a gigantic jet. These studies, however, successfully demonstrated that a charge imbalance inside the thundercloud is required for a leader to escape and provided excellent framework for future studies.

1.4   Scientific Contributions

The research questions considered for the scope of this dissertation are as follows:

1. What is the charge structure of thunderstorms producing gigantic jets and how are those charge structures formed?

2. Can gigantic jets be detected using space lightning mappers?

3. What instrumentation components are needed to advance our understanding of gigantic jets and lightning leaders?

4. What features are observed from the spectra of natural lightning leaders?

To answer the first research question, the parent thunderstorms of four gigantic jet producing systems are analyzed with a S-band radar data combined with very high frequency and low frequency lightning data. Using this data, the charge structure of gigantic jet storms is found, along with information about the evolution the parent storms charge structure before and after the gigantic jets. This charge structure is then tested with a numerical fractal lightning model. The second research

question is studied by using data from the Geostationary Lightning Mapper, with low-light-level ground-based video images of several gigantic jets serving as ground truth. The third research question involves studying the properties of lightning leaders and relating them to gigantic jets. These properties are used as guidance in the construction of an automated high-speed spectroscopy system, to capture lightning leaders and gigantic jets. The last research question involves analyzing the data obtained from the high-speed spectrograph, which includes analysis of lightning stepped leaders, dart leaders, and intracloud leaders.

Chapter 2

Data and Methodology for Remote Sensing Lightning and Thunderstorms

For remote sensing lightning and thunderstorms, several data sets were used in these studies. This data includes: ground based radar, very high frequency (VHF) and low frequency (LF) lightning, satellite infrared (IR) and optical, and ground based video data. For analyzing the storm structure and parent lightning of gigantic jet producing storms, a combination of radar variables was used along with VHF and LF lightning data. The radar variables aided in characterizing the thunderstorm structure and the turbulence and wind shear associated with the storm. The VHF lightning data allowed the parent lightning of gigantic jets and other lightning discharges to be mapped three dimensionally, allowing detailed study of the lightning discharge morphology. This provided information about the charge structure of the thunderstorm. The LF lightning data provided information about

the dominant charge regions of the thunderstorm, by studying the dominant polarity of intracloud (IC) and cloud-to-ground (CG) flash rates, as normally electrified thunderstorms will mostly produce positive IC flashes (moving negative charge upward between dominant middle negative and upper positive charge regions) and negative CG flashes (moving negative charge downward from the middle negative charge region to the ground), which fits the normal tripolar thunderstorm charge structure. The VHF and LF data also gave information about convective intensity, by studying the flash rates obtained from this data. The satellite IR data provided information about the storm top altitudes and aided in identifying overshooting cloud tops, a common feature among gigantic jet storms. The satellite optical lightning data provided flash characteristics of the parent lightning of gigantic jets and other discharges, such as optical energy, flash area, and lateral flash size. The low-light video camera data provided ground truth for gigantic jet detection, and allowed correlation with other data sources, such as optical satellite data to aid in identifying lightning characteristics associated with the gigantic jets. By combining these data sets, a clear picture of the thunderstorm charge structure and lightning discharge morphologies was accomplished with great detail. This chapter gives on overview of each of these datasets.

2.1   Weather Surveillance Radar, 1988, Doppler (WSR-88D)

The radar data used in this analysis was collected from the dual-polarization Weather Surveillance Radar 88-Doppler (WSR-88D) [*Crum and Alberty*, 1993] network. The radar locations used were Melbourne, FL (KMLB), Miami, FL

(KAMX), and Tulsa, OK (KINX). By analyzing the radar reflectivity, radial velocity, and spectrum width near the upper regions of the thundercloud, insight into the storm structure near the upper positive charge region was obtained. This aided in identifying the thundercloud charge structure of gigantic jets and provided information about the general storm structure, intensity, and evolution.

2.1.1 Reflectivity

Reflectivity (Z) is a measure of the power scattered back to the radar from a target [*Doviak et al.*, 2006] . Considering ice has a much lower dielectric constant than liquid water, ice hydrometeors have lower reflectivity values (< 30 dBZ) when compared to their liquid counterparts. Reflectivity can provide valuable insight into the structure of a thunderstorm, as updrafts and downdrafts will have an abundance of large, liquid hydrometeors. These features can be identified by large reflectivity values (35-60 dBZ). Low reflectivity values at high altitudes (cold temperatures, $< -40\,^{\circ}\mathrm{C}$) can be indicative of frozen hydrometeors. Dual polarization radars measure a vertical (Z_v) and horizontal component (Z_h) of reflectivity. These components are with respect to the radar, with the horizontal (vertical) component being parallel (perpendicular) to Earths surface. However, only (Z_h) is used when viewing reflectivity data alone, which is what was analyzed for this study.

2.1.2 Spectrum Width

Spectrum width was used in this study to identify areas of wind shear and turbulence. However, there are five factors that can attribute to large values of spectrum width [*Brewster and Zrnic*, 1986; *Fang et al.*, 2004; *Doviak et al.*, 2006]. The equation for spectral broadening is

$$\sigma_v^2 = \sigma_s^2 + \sigma_t^2 + \sigma_\alpha^2 + \sigma_d^2 + \sigma_o^2$$

where σ_v is the total spectrum width, σ_s is due to wind shear, σ_t is due to turbulence, σ_α is due to antenna motion, σ_d is due to terminal velocities of different hydrometeors, and σ_o is due to the orientations of hydrometeors. From *Brewster and Zrnic* [1986], all the terms on the right hand side of the above equation can be neglected except for σ_s and σ_t if the values of spectrum width are large (as was in this dissertation). *Melnikov and Doviak* [2009] found that when the total spectrum width was larger than 4 m s^{-1} the σ_s and σ_t terms dominate. Common values of large spectrum width for this study were on the order of 10 m s^{-1} or greater. Thus, the main contributions for large values of spectrum width were wind shear and turbulence. Wind shear and turbulent mixing played an important role in forming discharges that escape the upper regions of the cloud, such as jets and gigantic jets.

The use of spectrum width data can provide information about mixing near the upper cloud boundary, which can assist in determining the size and magnitude of the upper positive charge region. This mixing is especially strong when the storm is embedded in strong environmental wind shear or around an overshooting cloud top. For tall thunderstorms, the thundercloud develops a strong upper negative screening charge on the upper cloud boundary, due to a higher conductivity gradient [*Riousset et al.*, 2010a]. If this upper negative screening charge gets mixed with the upper positive charge, the upper positive charge can be reduced. By looking at patterns of spectrum width near the thundercloud top, one can estimate how turbulent the environment is at the thundercloud boundary. If spectrum width shows large values (>8-10 m s^{-1}) in the upper regions of the cloud (within a few

km of the thundercloud boundary) then strong mixing is likely taking place.

2.1.3   Radial Velocity

The radar can measure the velocities of hydrometeors toward or away from the radar. When the radial distance from the radar to a group of hydrometeors changes between two radar pulses, a phase shift takes place. The Doppler radar measures this phase shift and can estimate the velocity of the hydrometeors in a given radar sample volume. Radial velocity can be used to estimate storm top divergence and rotation of a convective system. By looking at the radial velocities near storm top, divergence can be estimated by adjacent values of incoming and outgoing velocities along a radial path from the radar and the storm. For the thunderstorms analyzed in this study, radial velocity differentials, defined as the absolute value of the maximum outbound minus the maximum inbound radial velocities, were on the order of 30-50 m s^{-1}.

2.2   Radio Measurements of Lightning

Lightning has been found to emit pulses in the radio spectrum, ranging from VLF to VHF [*MacGorman and Rust*, 1998; *Uman*, 2001; *Rakov and Uman*, 2003]. For this study, VLF/LF radio data was analyzed from Vaisala's National Lightning Detection Network (NDLN) [*Orville*, 2008; *Cummins and Murphy*, 2009] and Vaisala's Global Lighting Dataset GLD360 [*Said et al.*, 2013]. The VHF lightning data was from the Oklahoma Lightning Mapping Array [*Rison et al.*, 1999] and the Kennedy Space Center Lightning Detection and Ranging (KSC LDAR) network [*Poehler and Lennon*, 1979].

2.2.1 VLF/LF NLDN and GLD360 Data

Two dimensional (latitude, longitude) lightning activity for the contiguous United States is reported on by the NLDN, which detects VLF and LF electromagnetic radiation of lightning return strokes and IC pulses [*Orville*, 2008; *Cummins and Murphy*, 2009]. This data provides the latitude, longitude, polarity, and peak current of each lightning event. This information is provided by detecting the magnetic fields associated with the large current transfer of a vertically oriented lightning channel. The NLDN network was recently upgraded in 2013 with newly deployed localization algorithms that significantly improved the detection and spatial accuracy of IC pulses associated with each lightning flash [*Murphy et al.*, 2014]. The IC pulses are defined as transient, non-vertical current transfers associated with an IC flash - typically occurring when the negative or positive leader network propagates laterally through a horizontally expansive charge region. With this upgrade, multiple IC pulses can be detected for each discharge that can reveal the two dimensional spatial structure of a given IC flash. The NLDN network, due to detection primarily at LF, has a maximum detection range of a few hundred km from a given set of stations. It has a detection accuracy of about 92% and a location accuracy of about 300 m [*Nag et al.*, 2011]. The GLD360 detects lightning in a similar manner to the NLDN, but focuses on the VLF spectrum and detects lightning from thousands of km. However, it cannot discern IC from CG discharges and has a lower accuracy than the NLDN. It has a detection accuracy of about 70% and a location accuracy of 2-5 km [*Poelman et al.*, 2013]

By combining the above types of data, the approximate geometry and location of the main charge regions can be inferred. By analyzing the dominant polarity of NLDN events and IC/CG events, the general charge structure can be theo-

rized. The classic tripolar thunderstorm has upper positive charge around 10-14 km above sea level (asl), middle negative charge around 6-8 km asl, and a small lower positive charge around 3-4 km asl [*Krehbiel*, 1986]. For the remainder of this dissertation, the altitudes will reflect asl. This charge structure will be dominated by positive IC events and negative CG events. Positive IC events are indicative of negative charge moving upward (or positive charge moving downward), which generally represents IC flashes between the middle negative charge and upper positive charge regions. Negative CG events represents negative charge moving to the ground from the middle negative charge region. A convective cell with the classic tripolar charge structure will usually have majority IC lightning events with much less CG events throughout its lifetime [*Prentice and Mackerras*, 1977; *Mackerras et al.*, 1998]. If a convective cell exhibits a much larger percentage of negative CG events, this could mean: 1) the cell has a very weak upper positive charge and/or 2) the cell has a very strong lower positive charge. If the cell has a weakened upper positive charge and a strong lower positive charge, the highest field region in the cloud will often be between the middle negative and lower positive charge regions, which will initiate a large number of negative CG discharges. Occasionally a storm can have an anomalous charge structure, such as an inverted tripolar or bottom heavy dipolar charge structure. The inverted tripolar charge structure has upper negative charge, middle positive charge, and possibly lower negative charge [*Rust et al.*, 2005]. The bottom heavy dipolar charge structure will have the same arrangement as the classic tripolar charge structure, only with an extremely large lower positive charge [*Nag and Rakov*, 2009]. In both of these cases, the dominant NLDN event types will be negative IC and positive CG. For the inverted tripolar charge structure, negative IC events (negative charge moving downward) represent

discharges between the upper negative and middle positive charge regions. For the bottom heavy dipole, negative IC events represent discharges between the middle negative and lower positive charge regions, similar to negative CG events with the classic tripolar charge structure only the negative leader is contained inside the lower positive charge region. Both the inverted tripolar and bottom heavy dipolar charge structures will exhibit dominant positive CG NLDN events, which is indicative of positive charge moving to ground. Thus, by analyzing the NLDN data, an emerging picture of the overall charge structure of the storm can be obtained.

For the work presented in this dissertation, the NLDN data provided information about lightning discharges from the parent storm of gigantic jets. This included the polarity, peak current, and 2D location. This information was used to assess the convective intensity of the thunderstorm, by analyzing the IC and CG flash rates, determine the dominant charge structure of the storm, and provide information about the parent lightning of the gigantic jets. The parent gigantic jet storms had dominant positive IC and negative CG events, indicative of a normal tripolar charge structure. Also, the parent discharges of the gigantic jets were associated with positive IC events, suggesting the gigantic jets were of negative polarity, transferring negative charge upward.

2.2.2   VHF Lightning Mapping Data

Very High Frequency (VHF) lightning locating systems detect VHF pulses emitted by stepping lightning leaders in the 60 MHz frequency range. They use multiple detectors spread out in a network (usually tens of km) to detect the VHF emissions. By using time-of-arrival (TOA) algorithms, they locate VHF pulses spatially in three dimensions. This allows the discharge morphology and spatial extent of

each discharge to be analyzed in detail. Using characteristics inherent to how the VHF networks detects leader breakdown in negative and positive charge regions, negative and positive charge regions can be located within a thunderstorm [*Thomas et al.*, 2001; *Wiens et al.*, 2005]. This is done by determining the polarity of lightning leaders and assuming a lightning leader will propagate in a region of the opposite polarity. Thus, a negative leader will propagate into positive charge and visa versa. By inspecting where a discharge (or multiple discharges) propagates, the general altitude and geometry of the charge regions of the thunderstorm can be obtained. As a double check, one can compare these results with the NLDN data to confirm if the storm has a classic tripolar charge structure or something anomalous. The peak radiated power, leader speed, and processes intrinsic to how the VHF networks detect leader breakdown can allow negative leaders to be distinguished from positive leaders.

VHF networks tend to detect negative leaders much better than positive leaders, and may actually only detect the negative recoil leaders traversing along positive leaders, knowns as K-events [*Shao and Krehbiel*, 1996; *Rison et al.*, 1999]. Negative leaders radiate an order of magnitude more power than positive leaders and will generally travel at faster speeds [*Thomas et al.*, 2001]. If a leader exhibits strong radiated power relative to other leaders of the same flash and travels quickly (10^5 m s^{-1} -10^6 m s^{-1}) then it is very probable to be of negative polarity. For a given discharge, a VHF network also detects the VHF emissions from the negative leader first, followed by the K-events associated with the positive leader. The VHF source points associated with flash initiation are generally from a negative leader [*Krehbiel et al.*, 2000]. Considering most discharges will have a small vertical portion (from flash initiation) and then propagate horizontally in large, thin sheets,

a clear division of charge regions can be obtained. Since the common convective system has the classic tripolar charge structure, middle negative charge should be located around 6-8 km and upper positive charge around 10-14 km. The charge analysis from VHF data will usually support this, and should clearly show this vertical distribution of charge regions.

2.3 Video Image Data

For part of this study, a low-light level video camera was used to record several gigantic jets from Tropical Storm Harvey. The camera uses was a Watec 902H Ultimate, with a CCD of dimensions 768 × 494 pixels with a 12 mm F/1.2 lens. This results in a horizontal field of view of approximately 32°. The video camera is located in Cabo Rojo Puerto Rico and is operated by citizen scientist Frankie Lucena.

2.4 Satellite IR and Optical Data

The satellite data used in these studies were from the Geostationary Operational Environment Satellite (GOES) 16 instrument. This satellite is operated by a joint effort from National Aeronautical and Space Agency (NASA) and the National Oceanic and Atmospheric Administration (NOAA). GOES-16 is in geosynchronous orbit and positioned at 75.2° West, which provides a field of view centered on the Americas. Using its Advanced Baseline Imager (ABI), GOES-16 provides high spatial and temporal resolution imagery of the Earth through 16 spectral bands at visible and infrared wavelengths. GOES-16 can also detect optical pulses from lightning with its Geostationary Lightning Mapper (GLM), which is a high-speed

optical detector.

2.4.1   Advanced Baseline Imager (ABI)

The GOES-16 ABI is a radiometer that senses spectral bands ranging from visible to infrared portions of the electromagnetic spectrum [*Schmit et al.*, 2017]. For this study, only the channel 13 clean longwave IR was used (10.33 μm), which provides measurements of the cloud top temperature. By comparing this with atmospheric soundings, estimates of cloud top heights can be found. For this band, the nadir spatial resolution is 2 km, a significant improvement over past GOES instruments. In terms of time resolution, the ABI can provide a full disk view every 15 minutes, and the continental U.S. every 5 minutes. Two mesoscale images can be produced every minute, from a small subset of the ABI field of view, being 1,000 km by 1,000 km. For the work presented in this dissertation, the update times were 15 minutes, due to the thunderstorm being located south of Puerto Rico and away from the continental U.S.

2.4.2   Geostationary Lightning Mapper

GLM is a staring optical imager that records the transient optical pulses produced by lightning or other optical phenomena at 500 frames per second. Its high orbital altitude enables its charge coupled device (CCD) focal plane to continuously observe optical activity across the western hemisphere with a relatively consistent pixel resolution (8 km at nadir increasing to 14 km at the edge of its field of view) [*Goodman et al.*, 2013]. GLM observes optical emissions through a 1 nm bandwidth around the 777.4 nm neutral oxygen emission line (OI). Because lightning emits strongly at this wavelength [*Christian et al.*, 1989; *Walker and Christian*,

22

2017], lightning events can still be identified against high background radiances when the sun is overhead. GLM can thus detect lightning at all times of the day and night.

GLM detections are organized into event, group, and flash features [*Goodman et al.*, 2013; *Rudlosky et al.*, 2018]. These features describe the recorded lightning signals on temporal and spatial scales ranging from 1 pixel within 2 ms to tens to hundreds of pixels over multiple seconds. The features have associated optical energies, which result from the dissociation, excitation, and subsequent recombination of atmospheric constituents as they respond to the sudden heating in the lightning channel [*Goodman et al.*, 2012a]. Events are the smallest unit of detection and are defined as a single pixel detected above a dynamic threshold. Groups describe one or more events that occur in adjacent pixels in the same 2 ms frame. Groups that are close in space and time to one another are clustered into features that describe individual flashes. The clustering approach used with the GLM data was built on more than 20 years of space-based lightning detection with LIS and the Optical Transient Detector (OTD) [*Mach et al.*, 2007]. It uses the same Weighted Euclidean Distance approach as LIS to distinguish individual flashes, but with the OTD space and time thresholds to account for the increased size of GLM pixels. The maximum spatial separation for the radiance-weighted centroids of groups in the same flash is 16.5 km, while the maximum time difference between groups in the same flash is 330 ms. Periods of sustained strong optical emission over many GLM frames raise the dynamic background radiance of a pixel and thus inhibits continued detection of a pulse [*Goodman et al.*, 2012a, 2013], potentially resulting in shorter durations of GLM detections of GJ events lasting over several hundreds of milliseconds.

Chapter 3

Thunderstorm Charge Structures Producing Gigantic Jets

3.1 Background

Nearly all gigantic jets have been found to originate in tall (14-18 km altitude), intense thunderstorms featuring overshooting tops that form in maritime tropical environments [*Pasko et al.*, 2002; *Su et al.*, 2003; *Cummer et al.*, 2009; *Soula et al.*, 2011; *Huang et al.*, 2012; *Meyer et al.*, 2013; *Lazarus et al.*, 2015; *Liu et al.*, 2015c]. There has been one documented case of a gigantic jet emerging from a low topped (6.5 km altitude) winter thunderstorm over the Mediterranean Sea, but it also had an overshooting top as the environmental tropopause was near 6 km altitude [*Van Der Velde et al.*, 2010]. When the emerging location of gigantic jets at the storm top can be accurately determined, they appear to escape from or near the convective core of the thunderstorm [*Su et al.*, 2003; *Cummer et al.*, 2009; *Huang et al.*, 2012; *Meyer et al.*, 2013; *Lazarus et al.*, 2015; *Liu et al.*, 2015c]. Often

gigantic jets occur during or near the end of a convective 'pulse', which corresponds to a period of rapid thunderstorm intensification and very strong updrafts [*Soula et al.*, 2011; *Meyer et al.*, 2013; *Lazarus et al.*, 2015]. The overshooting tops of gigantic jet producing storms are associated with strongly divergent anvil level winds as the updrafts encounter the tropopause [*Witt and Nelson*, 1991; *Brown and Torgerson*, 2003; *Wang et al.*, 2010]. It has also been found that gigantic jets escape the thundercloud along an axis that marks the center of this divergent outflow [*Lazarus et al.*, 2015] and their parent storms form in environments with large horizontal wind speeds near the altitudes of their respective thundercloud tops [*Van Der Velde et al.*, 2010; *Lazarus et al.*, 2015; *Boggs et al.*, 2016].

Due to the difficulty of gigantic jet observations [*Chen et al.*, 2008] there has been little observational work completed on understanding the charge structures of gigantic jet producing thunderstorms. As mentioned in Chapter 1, modeling studies have indicated that GJs initiate between the upper positive and upper negative screening layer, leaving the thundercloud top as a negative leader. But, those modeling studies were formulated from thundercloud charge structure observations of classic New Mexican thunderstorms, instead of the parent storms of GJs.

This study reported in this dissertation attempts to identify the most probable thundercloud charge structure that produces gigantic jets, and aims to determine how a lightning leader develops after it leaves the thundercloud charge. The charge structure is directly formulated from lightning and radar data from multiple convective systems that produced multiple gigantic jets. It is then validated by a three dimensional probabilistic lightning model, with a larger simulation domain than those used in previous studies to observe where the escaped lightning leader propa-

gates. Simulations for two other thunderstorm charge structures, which are either proposed by previous studies or possibly formed during the parent storm of gigantic jets, are also performed to verify the facilitating features of the proposed charge structure for producing gigantic jets. Finally, this study seeks to understand the meteorological processes that form this charge structure. The work presented here has been published in the peer-reviewed journal *Nature Scientific Reports* [*Boggs et al.*, 2018].

3.2   Radar and Lightning Observations

To better understand the common thunderstorm features near cloud top during gigantic jets, base reflectivity, radial velocity, and spectrum width derived from Weather Surveillance Radar 88-Doppler (WSR-88D) radar scans were analyzed for four gigantic jet producing thunderstorms (Figure 3.1 and Table 3.1). Reflectivity is a measure of the power scattered back to the radar from the target, radial velocity is the inbound/outbound velocity along a radial path extending from the radar, and spectrum width is a measure of turbulence in a radar bin, with large spectrum width values being more turbulent [*Istok and Doviak*, 1986; *Kollias et al.*, 2001]. The parent thunderstorm dates, approximate times, and locations are listed in Table 3.1. Some of the storms analyzed here were studied in detail before concerning their meteorological features and lightning activity indicated by radar measurements and lightning detection data*Meyer et al.* [2013]; *Lazarus et al.* [2015]; *Lu et al.* [2011]. Here we focus on analyzing the meteorological and lightning data that gives information of the temporal and spatial properties of the charge structure of those storms.
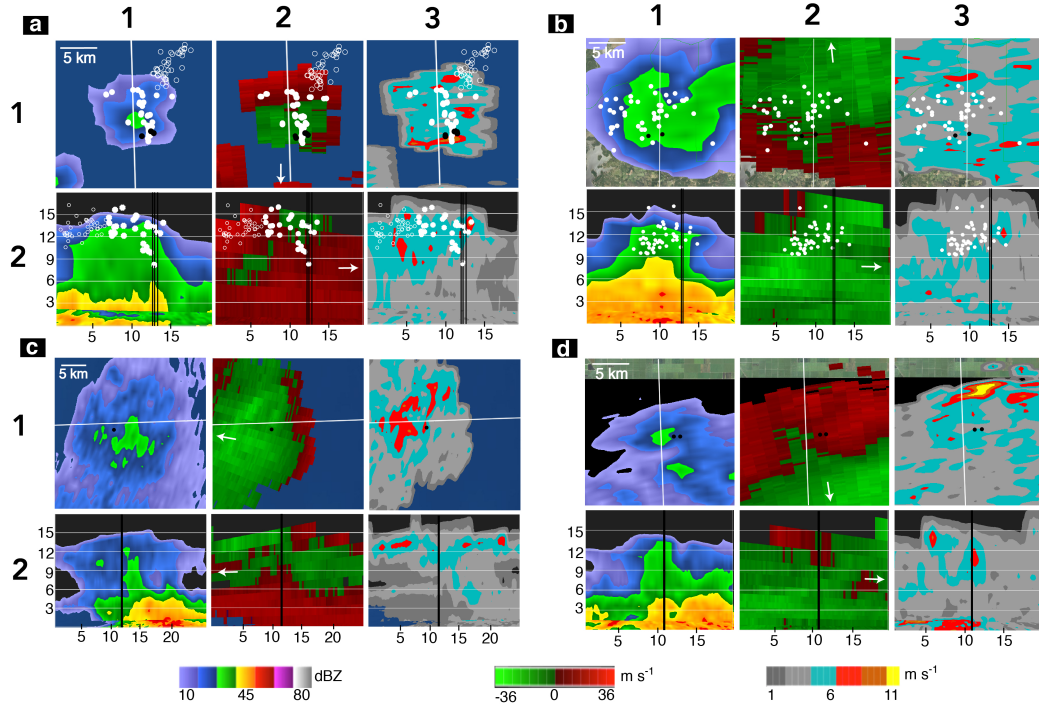
Figure 3.1: Common features of four gigantic jet producing storms. The top rows of each panel show horizontal elevation angle scans of base reflectivity, radial velocity, and spectrum width from the upper regions of the thundercloud (12-15 km). The bottom rows show vertical cross sections taken along the white lines of each radar variable from the top row. Radar and lightning data for the (a) Florida storm on 28 September 2010 [*Lu et al.*, 2011] (b) Oklahoma storm on 09 September 2010 [*Lu et al.*, 2011] (c) Florida storm on 03 August 2013 [*Liu et al.*, 2015c; *Lazarus et al.*, 2015] and (d) Florida storm on 12 September 2014 [*Boggs et al.*, 2016]. VHF lightning mapping data of the discharge activity in the upper positive charge region leading to each gigantic jet is shown (when available) as white circles and NLDN IC events as black circles or black vertical lines. The attempted bolt-from-the-blue is shown as open white circles [*Lu et al.*, 2011]. The white arrows in column 2 of each panel denote the direction pointing to the radar. Distance scales are listed in km.

All storms had reflectivity values greater than 30 dBZ at high altitudes (>12 km) and tall thundercloud tops (Figure 3.1a-d, column 1). Strong horizontally diverging winds near the thundercloud top were present in all cases (Figure 3.1a-d, column 2), with radial velocity differentials of 26-55 m s^{-1} (Table 3.1). The

Table 3.1: Overview of the gigantic jet storms shown in Figure 3.1. The radial velocity differential (RV Δ in m s^{-1}) is defined as the absolute value of the maximum outbound minus the maximum inbound radial velocities. The radial velocity differentials and maximum spectrum width (Max SW in m s^{-1}) values were taken from a radial at storm top passing through the region of largest reflectivity.

Date	Time (UTC)	Event (location)	RV	Max SW
09/09/2010	07:28	South OK, USA	38	11
09/28/2010	11:01	Northeast FL, USA	35	10
08/03/2013	04:11	Southeast FL, USA	55	9
09/12/2014	06:59	Southcentral FL, USA	26	11

vertical columns of high reflectivity were collocated with the centers of divergent outflow. Large values of spectrum width (9-11 m s^{-1}) were horizontally displaced from and just outside the convective core (Figure 3.1a-d, column 3). These large values of spectrum width indicate turbulent mixing [*Istok and Doviak*, 1986] near the thundercloud top, and are indicators of where upper negative screening charge may be mixed with upper positive charge [*Boggs et al.*, 2016]. These values are particularly large, as past studies have shown that spectrum width values greater than 4 m s^{-1} are considered turbulent [*Melnikov and Doviak*, 2009]. Lastly, the National Lightning Detection Network intracloud (NLDN IC) events and very high frequency (VHF) lightning sources associated with each gigantic jet were located near the axis of divergent outflow and near the convective core - except for the attempted bolt-from-the-blue (discussed in *Lu et al.* [2011] - open white circles in Figure 3.1a).

The charge structure producing gigantic jets was found from a combination of storm data, lightning data, and lightning simulations, but information about the charge structure was first obtained from re-analyzing available VHF lightning mapping data at different periods of the storms. The evolution of the VHF inferred charge structure for the 28 September 2010 Florida gigantic jet was investigated

at four time periods, each about one minute long (Figure 3.2 and Table 3.2). This case was chosen as it was closest to the VHF mapping system (about 60 km away). The details of determining the thundercloud charge are described in section 2.2.2. This storm underwent a convective surge or pulse near the time of the gigantic jet, as also identified by *Meyer et al.* [2013]. The VHF charge analysis times are: before the convective pulse (pre-pulse), near the beginning of the convective pulse (initial pulse), near the end of the convective pulse and during the time of the gigantic jet (final pulse), and after the convective pulse (post-pulse). The specific time periods analyzed are shown in Table 3.2, and each period corresponds to a panel in Figure 3.2. A similar analysis was completed for the 09 September 2010 Oklahoma thunderstorm that produced two gigantic jets [*Lu et al.*, 2011; *Meyer et al.*, 2013] and the 03 August 2013 Florida thunderstorm that produced four gigantic jets [*Liu et al.*, 2015c; *Lazarus et al.*, 2015], both of which had a charge structure evolution similar to the 28 September 2010 Florida thunderstorm. Before the convective pulse the storm had a wide, diffuse upper positive charge region over a similar sized middle negative charge region (Figure 3.2a). The large horizontal extent of the upper positive charge is indicated by the large azimuthal variation of VHF sources (ΔX), which was 25.5 km (Table 3.2). The mean altitude of VHF sources ($\overline{Z}$) in the upper positive charge region was 11.5 km altitude. The charge configuration during this time closely resembled a classic tripolar thunderstorm charge structure, but with a very small or nonexistent lower positive charge region as indicated by the lack of VHF sources at lower altitudes. Consistently, there were only three NLDN reported negative cloud-to-ground discharges in the time spanning fifteen minutes before the gigantic jet. There was a relatively weak divergence couplet present at storm top during this time, with a radial velocity

29
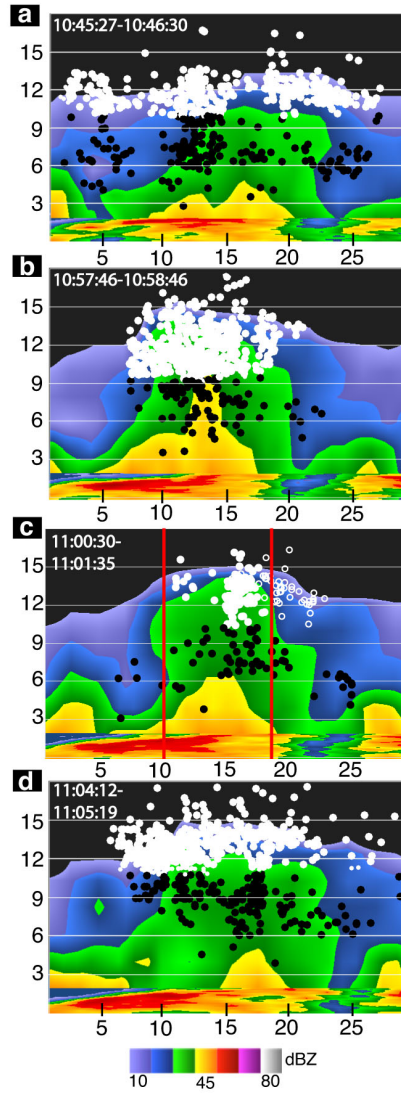
Figure 3.2: Charge structure evolution for the Florida gigantic jet on 28 September 2010. VHF inferred charge structure for the (a) pre-pulse (b) initial pulse (c) final pulse (gigantic jet) and (d) post pulse times. The white circles denote upper positive charge and the black circles denote middle negative charge as inferred from the VHF mapping system. The attempted bolt-from-the-blue is shown as open white circles [*Lu et al.*, 2011]. The red vertical lines in (c) denote the edges of large spectrum width values shown in Figure 3.1a, column 3. Distance scales are listed in km.

Table 3.2: Statistics describing the upper positive charge region for the Florida thunderstorm on 28 September 2010. ΔX represents one standard deviation about the mean of the VHF sources in the azimuthal direction, and $\overline{Z}$ represents the mean altitude of VHF sources.

	Time (UTC)	Δ X (km)	$\overline{Z}$ (km)
Pre-Pulse	10:45:27-10:46:30	25.5	11.5
Initial Pulse	10:57:46-10:58:46	5.8	11.7
Final Pulse (GJ)	11:00:30-11:01:35	4.9	13.2
Post-Pulse	11:04:12-11:05:19	12.7	12.9

differential of 29 m s^{-1} (Figure 3.3, upper left). During the onset of the convective pulse, the number of VHF sources in the upper positive charge increased, and the upper positive charge climbed higher in altitude (Figure 3.2b). The majority of VHF sources were contained within the relatively narrow reflectivity column ($>$ 30 dBZ). The intensity of the pulse was reflected by the altitude of the 45 dBZ echo, which reached a local maximum during this time (about 10 km, compared with 5 km before and after the pulse). The radial velocity differential at storm top increased to 38 m s^{-1}, shown in Figure 3.3, middle left panel. Near the end of the convective pulse and during the gigantic jet (Figure 3.2c), the upper positive charge reached its highest altitude ($\overline{Z}$ of 13.2 km) and became very narrow, with a ΔX of 4.9 km. The majority of the VHF sources were confined within the boundaries of maximum spectrum width (marked as vertical lines in Figure 3.2c) surrounding the reflectivity column ($>$ 30 dBZ), and there was a significant decrease in the number of VHF sources. The radial velocity differential at storm top reached its maximum during this time, with a value of 40 m s^{-1} (Figure 3.3, right middle panel). The open white circles shown in Figure 2c were from the 'attempted bolt-from-the-blue' [*Lu et al.*, 2011], which was part of the parent gigantic jet flash. After the convective pulse, the upper positive charge widened again (ΔX of 12.7
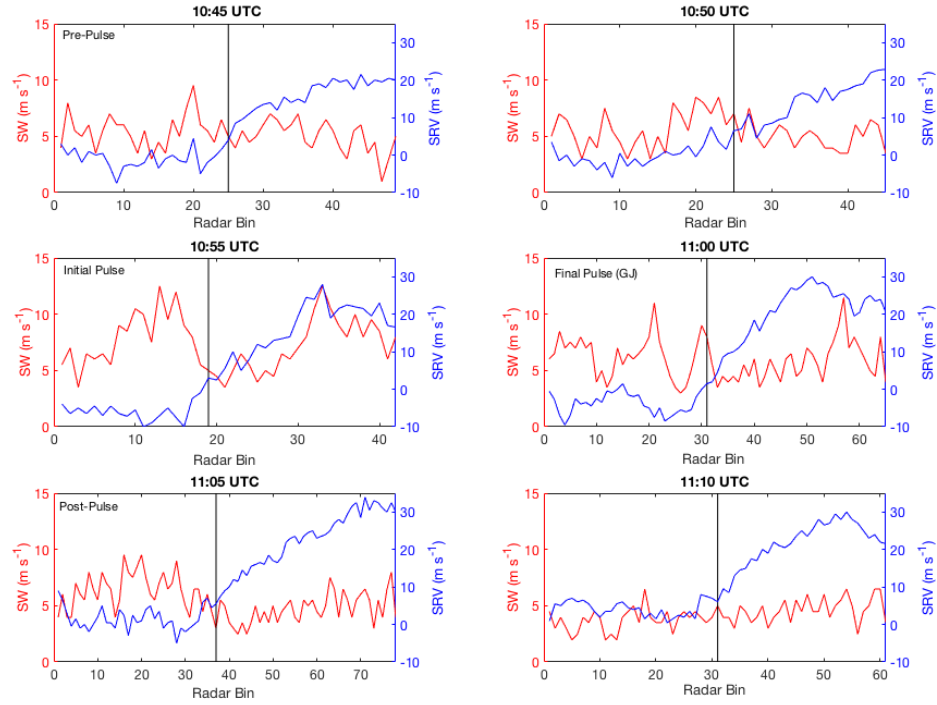
Figure 3.3: Evolution of storm top radial velocity and spectrum width for the storm on 28 September 2010. Spectrum width (SW) and Storm Relative Velocity (SRV) along a radial through the largest reflectivity at storm top. The radar bin numbers on bottom axis do not all begin at the same location, but are centered around the convective core for each time. The center line represents the center pixel of reflectivity > 30 dBZ.

km) and began to subside ($\overline{Z}$ of 12.9 km). However, the radial velocity differential at storm top remained large (39 m s^{-1}) until the next radar volume scan (four minutes later), when the radial divergence couplet disappeared altogether.

3.3 Probabilistic Lightning Simulations

Simulations using a three dimensional probabilistic lightning model [*Krehbiel et al.*, 2008; *Riousset et al.*, 2010b] were performed in conjunction with the data analysis

discussed above in order to find the charge structure of gigantic jet producing storms (Figure 3.4). Three charge structures were tested and simulations for each charge structure were run a total of ten times to find the discharge patterns that were most prevalent for each charge structure, so outliers were not reported on. If the discharge reaches the top boundary of the simulation domain, it is categorized as a possible gigantic jet. It should be noted that the model does not simulate the temporal evolution of the discharges, but the spatial characteristics of the discharges are simulated, similar to previous studies [*Mansell et al.*, 2002; *Riousset et al.*, 2007; *Krehbiel et al.*, 2008; *Riousset et al.*, 2010b].

The three dimensional probabilistic fractal model used has been described in detail in other studies [*Riousset et al.*, 2007; *Krehbiel et al.*, 2008; *Riousset et al.*, 2010b]. The simulations presented here used equidistant grid points of 400 m in the x, y, z directions and used open boundaries [*Riousset et al.*, 2007] over a perfectly electrically conducting flat ground plane with zero potential. Simulations with a smaller or larger grid size gave similar results. When a smaller (larger) grid size was used, the net amount of negative charge needed to form an escaped leader was less (more). This is due to the leader trees with fine resolution being able to occupy the regions of thundercloud charge better than the leader trees with coarse resolution, which resulted in more charge on the leader tree for the fine resolution cases (this effect of the grid resolution was noted previously by *Mansell et al.* [2002]). The simulation also uses an internal channel field of $1.0\,\mathrm{kVm^{-1}}$ to account for leader resistivity [*Williams and Heckman*, 2012], which is similar in magnitude to other lightning modeling studies [*Mansell et al.*, 2002]. The internal electric field is assumed to scale with neutral density as $\frac{N}{N_0}$, as it has been shown that the reduced electric field in the channel formed after streamer-to-leader transitions is
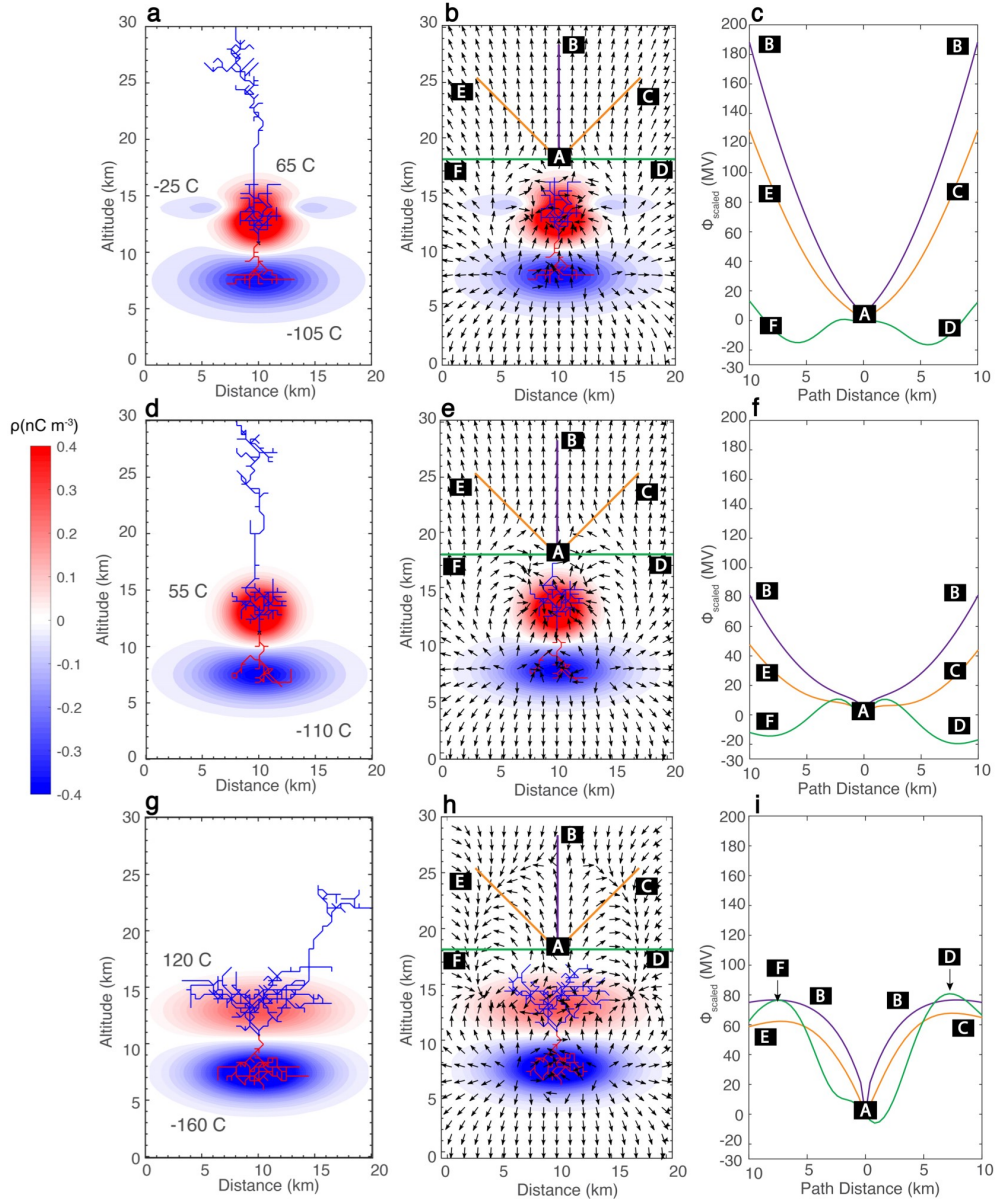
Figure 3.4: Modeling results of potential gigantic jets. (a-c) Simulated discharge trees overlaid on Gaussian thunderstorm charge structures. Positive (negative) charges and leaders are colored in red (blue). Charge amounts are in Coulombs. 'X's denote location of discharge initiation. Electric field magnitude and the direction of -**E** near the upper positive charge region before the flash (d-f) and as the discharge escapes the cloud (g-i). Simplified charge distributions are overlaid as rectangles. Distance scales are listed in km. Z denotes height above ground and X denotes horizontal distance.

about the same at 20 km and 40 km altitudes (Figure 16 of *da Silva and Pasko* [2013]), but it should be noted that the scaling law of the leader channel field has not been well studied. A larger vertical domain was also used (30 km altitude) compared to previous simulations of gigantic jets [*Krehbiel et al.*, 2008; *Riousset et al.*, 2010b]. The upper terminal altitude was chosen because the model can only simulate a conducting leader channel, and the gigantic jet is predominantly composed of leaders below this altitude [*da Silva and Pasko*, 2013].

The constraints to determine the amount of charge in each region were (**1**) the leader discharge is initiated at the location where the electric field exceeds by 1-10% of the threshold value of the ambient field for leader initiation (about 200 kV m^{-1} at ground pressure) [*Marshall et al.*, 1995; *Dwyer*, 2003; *Behnke et al.*, 2005; *Williams*, 2006] (**2**) the charge densities must be less than the maximum values found from observations [*Winn et al.*, 1978, 1981; *Byrne et al.*, 1983; *Marshall and Rust*, 1991] (a few tenths to a few nCm^{-3}), and (**3**) the charge structures must have the minimum amount of net negative charge in the thundercloud for a negative leader to escape. The minimum amount of net negative charge is chosen because any additional amount of negative charge would always produce an escaped leader. This results in net charges of -65 C for Figure 3.4a, -55 C for Figure 3.4d, and -40 C for Figure 3.4g. The minimum amount of net negative charge is different for each charge structure due to the different charge region geometries.

Two charge structures feature narrow upper positive charge (Figure 3.4a,d), but one has a distribution of upper negative screening charge around the top of the upper positive charge (Figure 3.4a). The charge structure with upper negative screening charge is considered because it is probable that upper negative screening charge exists around the highest cloud tops of convective cells that produce negative

gigantic jets. Considering the relaxation time at storm top is very short (about 15 s at 15 km altitude [*MacGorman and Rust*, 1998; *Riousset et al.*, 2010b]), negative screening charge can form quickly at high storm tops. But, the strong storm top diverging winds should push away the screening charge from the center axis of the convective core, which would make a 'hole' in the upper negative screening charge. In nature this screening charge is likely not perfectly symmetric, but for the sake of simplicity, perfect axial symmetry is assumed. The altitudes and dimensions of the upper positive and middle negative charge regions in Figure 3.4a,d are set according to the lightning and radar data in the previous section during the time of the gigantic jets. A charge structure with a wide upper positive charge region, similar to previous modeling studies of escaped leaders [*Krehbiel et al.*, 2008; *Riousset et al.*, 2010b] is also considered (Figure 3.4g), which models the charge structure shown by Figure 3.2a,d. Lower positive charge is likely very small immediately preceding and during gigantic jets [*Meyer et al.*, 2013; *Boggs et al.*, 2016], as shown in Figure 3.2 and discussed above, and therefore are not included in the charge structures. However, simulations with lower positive charge were also completed, and the results indicate that the inclusion of the small lower positive charge does not change the conclusions of this study. Considering the convective systems producing gigantic jets are very wide (about 40 - 60 km for the storms presented here), the lateral cloud edges are far from the parent GJ flash, so the lateral screening charges are not included in the simulations.

The discharge patterns shown in Figure 3.4a,d closely resemble the parent lightning both inside and outside the thunderstorms producing gigantic jets. Within the confines of the cloud, the parent lightning has little lateral extension inside the upper positive charge region, which is consistent with the observations of the

36

initial in-cloud discharge activity of gigantic jets [*Lu et al.*, 2011], as also shown by Figure 3.2c. Upon exiting the thundercloud, the discharges escape as negative leaders extending upward above the convective core, similar to observations [*Su et al.*, 2003; *Cummer et al.*, 2009; *Huang et al.*, 2012; *Meyer et al.*, 2013; *Liu et al.*, 2015c; *Lazarus et al.*, 2015]. Finally, the discharges reach the upper boundary of the simulation domains. All ten (100%) simulations for each charge structure produced results closely resembling the discharge patterns presented in Figure 3.4a,d, demonstrating the effectiveness of these charge structures to produce upward negative leaders with the capability to form gigantic jets.

The discharges simulated with a wide upper positive charge region (Figure 3.4g) have large lateral extension and significant branching inside the upper positive charge region. The negative leader network in the upper positive charge extends significantly farther horizontally than the positive leader network in the middle negative charge, which contrasts with the initiating lightning observed by VHF sensors for gigantic jets [*Lu et al.*, 2011]. When the discharge exits the upper positive charge, it bends significantly and terminates on the lateral boundary of the simulation domain. This is the dominant discharge pattern for this charge structure, with seven out of ten (70%) simulations giving such a discharge pattern. This indicates that this charge structure is conducive to propagating discharges laterally above the cloud instead of directly upward, possibly turning into a bolt-from-the-blue. The other three simulations (30%) did reach the top boundary of the simulation domain, but the discharge still showed significant bending, terminating near the upper corners of the domain. The charge structure shown by Figure 3.4g also often produced multiple leaders exiting the upper positive charge, contrary to observations of gigantic jets.

Figure 3.4b,e,h shows the direction of -**E** overlaid on the thundercloud charge structure and discharge trees as the negative leaders exit the upper charge regions (note: in order to clearly show the direction of -**E** at every point the length of the arrow does not scale with its magnitude). We choose to show -**E** because its direction shows where a negative leader is most likely to propagate. The colored lines in these panels correspond to Figure 3.4c,f,i and denote paths to calculate scaled electric potential (discussed below). In Figure 3.4b,e, -**E** above the upper charge points toward the vertical symmetry axis (Distance = 10 km), and then upward, constraining the escaped negative leaders to propagate directly upward above the thundercloud. For the charge structure with wide upper positive charge (Figure 3.4h), -**E** points outward from the vertical symmetry axis, encouraging the escaped negative leader to propagate laterally above the cloud.

Profiles of scaled electric potential (ϕ_{scaled}) above the upper charge regions is shown in Figure 3.4c,f,i, with the paths indicated by the colored lines in Figure 3.4b,e,h. Since the lightning propagation threshold field is linearly dependent on air density [*Marshall et al.*, 1995; *Dwyer*, 2003; *Behnke et al.*, 2005; *Williams*, 2006], the potential along each path is normalized to ground pressure to allow for meaningful comparisons of leader propagation along different paths. This scaled potential is calculated by

$$\phi_{scaled} = \int_{path} -\frac{N_0}{N}\mathbf{E} \cdot \mathbf{dl} \qquad (3.1)$$

with all paths beginning at the box marked A and ending at the corresponding boxed letter, with N (N_0) the density at a given altitude (ground). Each path was 10 km in length. The path from $A \rightarrow B$ is plotted twice in panels c,f,i for ease of viewing. For the charge structure with narrow upper positive charge and

upper negative screening charge (Figure 3.4a), two minima in ϕ_{scaled} exist along the lateral paths of $A \rightarrow F$ and $A \rightarrow D$ (Figure 3.4c). Considering the escaping leader is of negative polarity, it propagates towards increasing potential. Thus, the escaping leader avoids the lateral paths ($A \rightarrow F$ and $A \rightarrow D$). The diagonal paths ($A \rightarrow E$, $A \rightarrow C$) and the vertical path ($A \rightarrow B$) have large values of ϕ_{scaled}, so the negative leader travels in the upward direction. But, the largest potential difference occurs along the vertical path ($A \rightarrow B$), which prompts the escaped negative leader to propagate along the vertical symmetry axis. Figure 3.4f shows the scaled potential profile for the charge structure with narrow upper positive charge. The variation of ϕ_{scaled} along each path is similar to the previous case, but the vertical and diagonal paths have a smaller potential difference when compared to the charge structure of Figure 3.4a. The escaped negative leader still propagates along the vertical symmetry axis where the largest potential difference is.

The charge structure with wide upper positive charge has a scaled potential profile above the cloud (Figure 3.4i) that is significantly different from the charge structures with narrow upper positive charge. The largest directional derivative and largest potential difference occur for the lateral paths ($A \rightarrow F$, $A \rightarrow D$). Thus, the escaping negative leader propagates in the lateral direction above the cloud, instead of upward. Also, notice that the vertical and horizontal paths have a narrower spread of values in ϕ_{scaled} for this charge structure, compared with the other two cases, which increases the probability for the escaped leader to propagate in a random direction. However, the largest potential differences are along the lateral directions producing a dominant discharge pattern that extends laterally above the cloud.

Considering the amount of net charge is different among the three cases, addi-
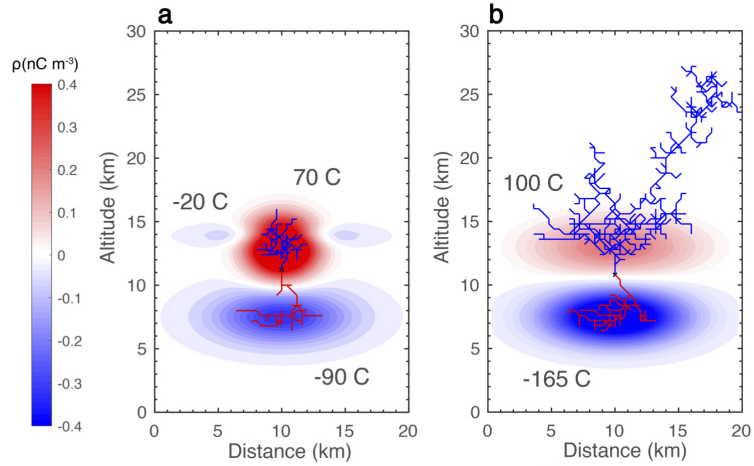
Figure 3.5: Simulations with different net charge amounts. (a) Same as Figure 3.4a except with a net charge of -40 C. (b) Same as Figure 3.4g only with a net charge of -65 C.

tional simulations were completed for the charge structures of Figure 3.4a,g, only with the net charge amounts switched (Figure 3.5) to investigate the effect of net charge on the discharge leader discharge tree. The charge structure in Figure 3.5a does not produce any escaped negative leaders out of the additional ten simulations, forming positive IC discharges for every simulation. For the charge structure in Figure 3.5b, the escaped negative leader terminates on the lateral boundary of the simulation domain. This is the dominant discharge pattern for this charge structure, which occurs for seven (70%) of the simulations and is similar to the charge structure presented in Figure 3.4g. From the results shown in Figure 3.4 and 3.5, wide, weakened upper positive charge can produce escaped leaders at a smaller amount of net charge than narrow, weakened upper positive charge, but those escaped leaders propagate in the lateral direction once they escape. Narrow, weakened upper positive charge requires more net negative charge for a leader to escape, but once a negative leader escapes, it will propagate upward. This is also

40

true when there is more net negative charge than shown in Figure 3.4a,d. Thus, whether a successfully escaped leader will propagate upward, not laterally, to potentially form a gigantic jet is primarily determined by the geometry of the charge structure and not by the amount of net charge.

3.4   Discussion

The charge structures in Figure 3.4a,d both formed upward negative leaders that reaches the top of the simulation domain. An approach for investigating if the escaped leader will develop into a gigantic jet is to determine if the leader tip is able to reach the jump altitude, h_{jump}. The jump altitude is the altitude from which the streamers preceding the leader tip can extend all the way to the lower ionosphere. The jump altitude depends on the leader tip potential, and a larger leader tip potential gives a lower jump altitude. The ionospheric potential is about 250-300 kV [*Uman*, 1974; *Markson*, 1976], and is much smaller than the potential of the escaped leaders. The absolute value of the leader tip potential is 24 MV (Figure 3.4a) and 18 MV (Figure 3.4d) when it reaches the top boundary of the simulation domain. Figure 3.4d of *da Silva and Pasko* [2013] indicates these values correspond to jump altitudes of 42 km and 45 km, respectively, if the streamer zone of a negative leader consists of negative streamers only. This means if the simulated leaders cease propagating upward, a negative jet is formed. It is possible the leaders continue propagating upward, and if their potentials are not reduced significantly when the leaders reach 42 km or 45 km, a gigantic jet will be formed. In addition, as discussed by *Liu et al.* [2015c,a], the streamer zone of a negative leader may consist of both positive and negative streamers, so the jump altitudes

for the two leaders in Figure 3.4a,d can be potentially lower.

Due to the short time scale of screening charge formation at high altitudes [*MacGorman and Rust*, 1998; *Riousset et al.*, 2010b], the upper negative screening charge can approach the magnitude of the upper positive charge [*Riousset et al.*, 2010b], indicating the negative screening charge in Figure 3.4a could potentially be much stronger. Simulations indicate (not shown) that when the upper negative screening charge in Figure 3.4a is doubled to -50 C, the absolute value of the leader tip is about 60 MV when the ascending negative leader reaches the top boundary of the simulation (30 km altitude), which corresponds to a jump altitude of about 36 km (for negative streamers). This is similar to the jump altitudes of the last two gigantic jets produced by tropical depression Dorian [*Liu et al.*, 2015c], which were about 35 km. Other things being equal under the constraints on the amount of charge in each region discussed in the previous section, the charge structure in Figure 3.4a can allow accumulation of more net negative charge in the system, making it potentially easier to produce gigantic jets for this charge structure.

The wide, weakened upper positive charge structure (Figure 3.4g) has a leader network above the cloud that extends significantly in the lateral direction. This charge structure assumes relatively uniform mixing of the upper negative screening charge throughout the entire volume of the upper positive charge, with a fully symmetrical configuration of the charge regions. Such a perfect symmetry likely does not occur in nature. A similar charge structure to that in Figure 3.4g but with laterally displaced, weakened upper positive charge has been shown to produce bolt-from-the-blue discharges (BFB) [*Boggs et al.*, 2016], and the leader network shown in Figure 3.4g resembles a bolt-from-the-blue discharge, consistent with that study.
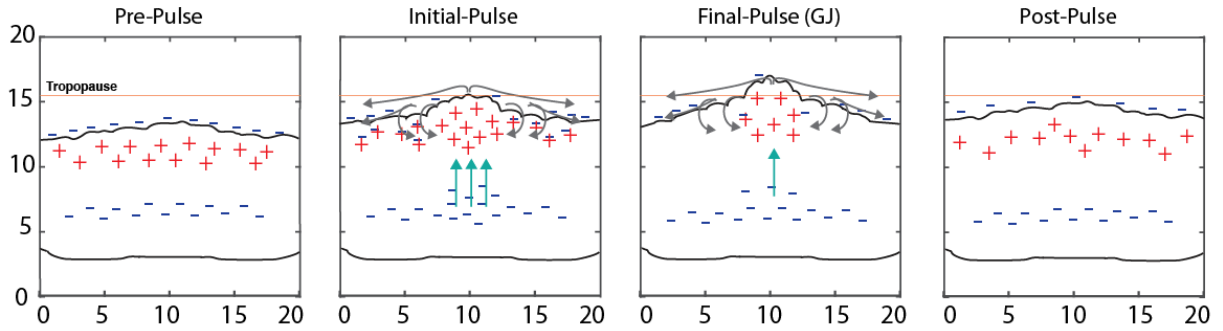
Figure 3.6: Conceptual illustration showing the formation of the gigantic jet charge structure. Plus's (+) and minuses (−) indicate positive and negative charge, the green arrows represent the updraft, and the gray arrows the wind flow near cloud top. The horizontal orange line is the tropopause.

The charge structure producing negative gigantic jets seems to be a result of the convective pulse. Before the convective pulse, the thunderstorm is in a quasi-steady state, with a dominant dipolar charge structure consisting of upper positive and middle negative charge, with a relatively strong upper negative screening layer (Figure 3.6, Pre-Pulse). During the onset of the convective pulse, an intense up-draft produces strong storm top divergence and turbulence at cloud top. This is supported by the large radial velocity differentials and spectrum width values in Figure 3.3, with the maximum spectrum width values located on the outer edge of the convective core (convective core as defined by reflectivity > 30 dBZ). We theorize that the diverging winds push the negative screening charge away from the center axis of the highest cloud tops, and large turbulent eddies form around the convective core mixing negative screening charge with upper positive charge, weakening the upper positive charge. This process is shown in Figure 3.6 (middle two panels). But, during the initial-pulse, the strong updraft continuously replen-ishes upper positive charge (large charging current), reducing the charge imbalance between the upper positive and middle negative charge. Near the end of the pulse

(Figure 3.6, Final-Pulse) the updraft has weakened (small charging current), but the storm top turbulence persists for a couple of minutes, mixing negative screening charge with upper positive charge. During this time, the largest charge imbalance exists in the thundercloud, providing an ideal time to initiate a GJ. This process may explain how the narrow upper positive charge region found in Figure 3.2c is formed. After the convective pulse, the intense updraft collapses, and the storm top divergence and storm top mixing subsides, returning to the quasi-steady state from the Pre-Pulse stage. The upper positive charge widens again and the charge imbalance between the upper positive and middle negative charge decreases.

This hypothesis is supported by the electrical measurements made at high altitudes by U-2 airplanes above thunderstorms with high cloud tops [*Vonnegut et al.*, 1966; *Blakeslee et al.*, 1989]. These measurements show the vertical component of the electric field becomes increasingly positive as the airplane passes above the highest cloud tops of the thunderstorm. This suggests (for a normal polarity storm) the upper negative screening charge is being pushed to the sides of the overshooting top, creating a 'hole' in the screening charge layer, which reveals the upper positive charge (see Figure 9 of *Vonnegut et al.* [1966]). Mixing of upper negative screening charge with upper positive charge near high cloud tops has been hypothesized before, from observations of anomalous VHF activity in the upper regions of thunderstorms [*Krehbiel et al.*, 2000; *Bruning et al.*, 2010; *Emersic et al.*, 2011; *Calhoun et al.*, 2013; *MacGorman et al.*, 2017]. The authors of those studies speculated that this was caused by the upper negative screening layer being folded into the top of the thunderstorm [*Emersic et al.*, 2011; *Calhoun et al.*, 2013; *MacGorman et al.*, 2017]. This motion near cloud top is similar to the entrainment studies described by *Blyth et al.* [1988] and *Stith* [1992].

The findings reported here suggest that convective pulses creating overshooting tops are a primary driver in creating the charge structures that produce negative gigantic jets. However, convective pulses and overshooting tops are commonly found in supercell and multicell convection throughout the mid-latitudes, where gigantic jet observations are infrequent. The question is then: why are there not more gigantic jet observations from mid-latitude convection where intense updrafts and overshooting tops are commonplace? The answer to this question is likely related to the differences between the charge structures of mid-latitude and maritime tropical convection that have intense, pulsating updrafts that produce overshooting tops. The analysis reported here indicates that maritime tropical convection with overshooting tops that produce gigantic jets exhibit charge structures similar to the normal tripolar configuration with upper positive charge, middle negative charge, and possibly augmented by a small lower positive charge. This is supported by the dominant positive IC and negative CG discharges from gigantic jet producing storms [*Meyer et al.*, 2013; *Lazarus et al.*, 2015; *Liu et al.*, 2015c] and detailed VHF mapping of topical maritime thunderstorms located near Columbia [*López et al.*, 2019]. In contrast, the charge structures in supercell convection have been found to be very complex, with anywhere from three to twelve charge regions existing simultaneously. These charge regions are often adjacent to each other, which results in small intracloud flashes that occur at very high rates, with total flash rates in supercell convection often reaching several hundred per minute [*MacGorman et al.*, 2008; *Bruning et al.*, 2010; *Calhoun et al.*, 2013; *Wiens et al.*, 2005]. Total flash rates from gigantic jet producing convection have been found to be an order of magnitude lower [*Meyer et al.*, 2013; *Lazarus et al.*, 2015; *Liu et al.*, 2015c] or even less. Mid-latitude supercell and multicell convection often have anomalous charge

45

structures that have huge areas of middle/lower positive charge [*Lang et al.*, 2004; *Tessendorf et al.*, 2007; *Weiss et al.*, 2008]. These storms exhibit large percentages of positive CG discharges (50-100% compared with $< 10\%$ for normal convection [*Orville*, 1994]) and IC discharges between the middle negative and middle/lower positive charge regions (-IC). The middle/lower positive charge often participates in the majority of discharges, so few discharges take place in the upper parts of the thundercloud. Thus, for mid-latitude supercell and multicell convection that have intense updrafts and overshooting tops, other forms of discharges often win the competition to neutralize charge, rather than the normal positive IC flash that is associated with the initiation of gigantic jets [*Krehbiel et al.*, 2008; *Riousset et al.*, 2010b; *Lu et al.*, 2011].

Chapter 4

Satellite and Video Observations of Gigantic Jets

4.1 Background

Typical ground-based observations of GJs are made by using low-light-level video cameras. This observation method is not ideal for monitoring GJ activity, as the camera must have a clear view of the region above thunderclouds. An optimal viewing condition is often unavailable during potential GJ producing storms, because those storm systems (tropical systems at low latitudes) are normally accompanied by substantial areas of stratiform clouds.

GJs have also been observed by space-based instruments including the Imager of Sprites and Upper Atmospheric Lightning (ISUAL) onboard the FORMOSAT-2 satellite [*Chen et al.*, 2008]. The FORMOSAT-2 satellite is in a sun-synchronous orbit with a mean altitude of approximately 890 km, which corresponds to an orbital period of about 102 minutes. ISUAL was designed to provide a limb view

of the Earth's surface around local midnight, and its instrument consists of an intensified charged coupled device imager, a six-channel spectrophotometer, and a dual-band array photometer. Tens of GJs were observed during a five year operational period (from 2004 to 2009) [*Chou et al.*, 2010], and have been analyzed to obtain the information on the discharge processes, electric fields, and streamer polarities in GJs by *Kuo et al.* [2009] and *Chou et al.* [2010]. A global occurrence rate of 0.01 events per minute was also estimated for GJs [*Chen et al.*, 2008], which indicates that a space instrument with a larger coverage will detect many more events. This same issue also exists for other low earth orbit space-based lightning observation systems, such as the Lightning Imaging Sensor (LIS) [*Christian et al.*, 1999]. However, with the establishment of geosynchronous instrumentation such as the Geostationary Lightning Mapper (GLM) [*Rudlosky et al.*, 2018], new opportunities are available to detect and observe TLEs and GJs.

This chapter presents the first observations of GJ lightning signatures from a detector on a geostationary orbiting satellite. The GJs occurred during Tropical Storm Harvey when it was located approximately 500 km south of Puerto Rico on 19 August 2017. Low-light-level video footage indicated Harvey produced at least fourteen GJs, and possibly a few more that cannot easily be identified in the video. Most of the GJs produced distinguishable signatures in the GLM data. Unlike typical GLM flashes that radiate discrete optical pulses, GJ flashes contain long periods of sustained optical emission over a single location and have higher peak group and flash optical energies. They are different from spider flashes and K-processes [*Peterson et al.*, 2017b, 2018; *Peterson and Rudlosky*, 2018] that produce long periods of sustained emission, because there is a lack of lateral development between groups in the GJs. Instead, the largest optical energy is located in the

same GLM pixel in all frames of the GJ. The optical energy of the pixel increases with time as the GJ discharge propagates upward, reaches its peak when the upward discharge connects to the ionosphere, and then decreases and fades away. The work presented in this chapter has been published in the peer reviewed journal *Geophysical Research Letters* [*Boggs et al.*, 2019].

4.2 Video Observations

On the evening of 19 August 2017 Tropical Storm Harvey passed approximately 500 km south of Puerto Rico with 35 kt (18 m s^{-1}) sustained surface winds and a central pressure of 1005 mb [*Blake and Zelinsky*, 2017]. During its transit south of the island, the storm underwent a nocturnal convective burst between 0400-0900 UTC during which the anvil substantially increased in areal extent and the storm produced more than 25,000 flashes as observed by Vaisala's GLD360 lightning network [*Said et al.*, 2013]. GOES-R infrared satellite (band 13) brightness temperatures were as low as 190 K, indicating high cloud tops (15-18 km altitude). During this period, a low-light level Watec 902H Ultimate camera system (768 × 494 pixels, 12 mm F/1.2 lens, 32° horizontal field of view (FOV)) operated by Frankie Lucena in Puerto Rico recorded many TLEs, including sprites, elves, and fourteen clearly-identifiable GJs. Despite the intense convection, Harvey was weakening due to the strong northeasterly shear, and later became a tropical wave. The environment, while unfavorable for storm intensification and hurricane development, provided an unobstructed view (as seen from Puerto Rico) of the convective storm tops during the GJ events with the anvil debris displaced away from the ground-based camera. Most of the early (0400-0700 UTC) GJs occurred

in association with the deep convection near the storm center, while the last two (just before 0900 UTC) occurred within a convective region 250 km north of the center of circulation.
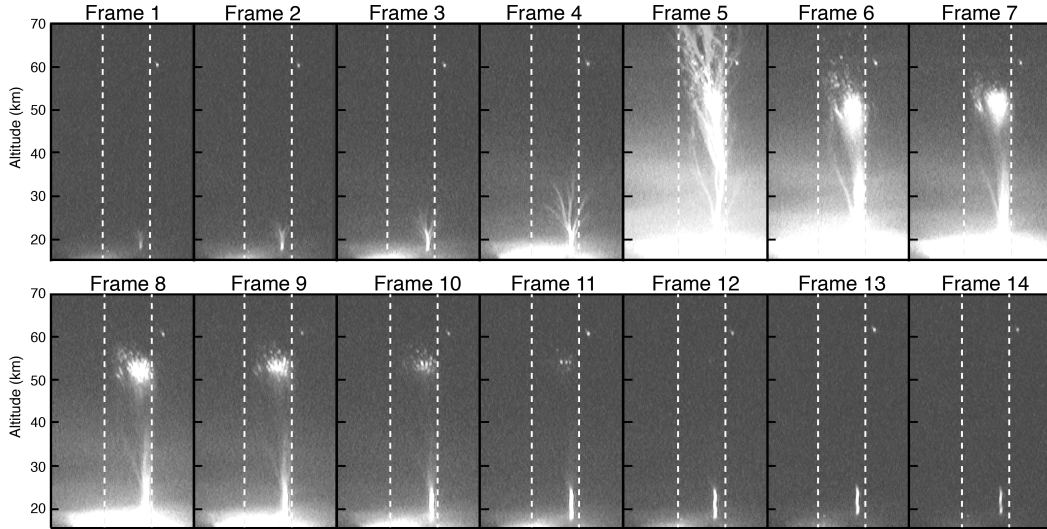
Figure 4.1: Low-light-level images of the 08:46 UTC gigantic jet on 19 August 2017. Frame 1 corresponds to 08:46:02.864 UTC with each successive frame corresponding to an additional 33 ms. The dashed white lines denote the width of the Geostationary Lightning Mapper pixel with the largest optical energy (white outlined pixel in Figure 4.2). The altitude scale is in kilometers. Note that each panel of Figure 4.1 has a smaller horizontal FOV (8°) than the camera's FOV (32°), and the width of each panel is approximately 30 km. FOV = field of view.

Out of all the recorded GJs, the last two were closest to the camera (< 250 km), leading to the best video data. Both of them had similar morphologies, and here we present the video images of the first event only, which occurred at 08:46 UTC. Figure 4.1 shows low-light level images of this GJ, which is visible for fourteen video frames (462 ms). The region bounded by the two white dashed lines in Figure 4.1 corresponds to the location of the GLM pixel with the largest optical energy during the duration of the GJ, and the GJ is primarily contained within this pixel. The

azimuthal positions of the vertical white lines were calculated using the relative azimuthal angles of two stars in the video images (Achernar, absolute magnitude -1.46; and α ret, absolute magnitude -0.17). Achernar is the bright white dot on the right side of the vertical dashed lines and α ret is out of the FOV in Figure 4.1 . The relative azimuths of the two stars allowed calculation of the azimuth per pixel in the video images. Then the azimuthal angle between the camera site and the GJ was calculated using the location of the brightest GLM detection, and this azimuth was mapped to the video images. Assuming the location error of a GLM detection is negligible, the uncertainty in the azimuthal positions of the vertical white lines is 0.2 km, which is from the estimation of the azimuthal angle between the camera and the high-energy GLM pixel. However, the location error of GLM detections has been found to be up to a few km. [*Buechler et al.*, 2018].

Frames 1-4 show the ascending discharge before its jump to the ionosphere. The speed of the GJ during this time increased from 9.1×10^4 m s^{-1} to 1.8×10^5 m s^{-1}, similar to past GJs [*Liu et al.*, 2015c]. The highest altitude reached before the jump to the ionosphere is approximately 34 km. The altitude of the GJ was calculated using the same method described above, only with the elevation angle instead of the azimuthal angle, which allowed calculation of the elevation angle per pixel. The altitude was then calculated by using the elevation angle and the distance from the camera to the brightest GLM pixel. If GLM's location accuracy is one half a GLM pixel, the altitude uncertainty is 1.02 km. From frame 4 to 5, the discharge connects to the ionosphere, and it reaches at least 70 km altitude. Frame 5 is also the brightest video frame, with much of the image saturated. For frames 6-11, the altitude of the visible top is 56 km, with the top and base of the channel being illuminated the most. The top of the discharge also exhibited a filamentary

structure during this time. Frames 12-14 are the final images of the GJ, with only the base of the channel remaining illuminated, and a maximum altitude of 26 km. The visible part of the discharge during this time resembles a singular, branchless structure.

4.3   GLM Observations

The GJ signatures were found in the GLM data by first identifying the GLD360 [*Said et al.*, 2013] events that matched the Global Positioning System (GPS) time stamp and the azimuth provided by the ground-based video images. Then, the GLM data was filtered spatially to match the GLD360 detections and temporarily to match the GPS time stamp of the video images. Most of the GJs from the video images were found in the GLM data, and the mean GLD360 peak current for each GJ was 20 kA, with each GJ having on average about three GLD360 detections. GLM observations of the 08:46 UTC GJ are shown in Figures 4.2 and 4.3. Figure 4.2 shows the GLM pixels of the GJ signature overlaid on GOES-R infrared imagery. Each panel in Figure 4.2 corresponds to a video frame from Figure 4.1, and shows every GLM detection for the duration of the respective video frame. The GLM signature of the GJ only lasted for 6 video frames (frames 3-8). This is likely due to the dynamic detection threshold employed by GLM (discussed below) [*Goodman et al.*, 2012a, 2013; *Bitzer*, 2017]. Figure 4.3 is a time series of the GLM optical energies for the pixels shown in Figure 4.2. The vertical white lines in Figure 4.3 separate each video frame, and the video frame numbers are indicated at the top. Note, that because GLM has a much finer time resolution than the ground-based video frames, many GLM detections exist for a single video frame.

The pixel outlined in white in Figure 4.2 and 4.3 corresponds to the location of the area bounded by the two white dashed lines in Figure 4.1. The different color pixels correspond to different GLM optical energies, which are arbitrarily defined as < 10 fJ (blue), 10-20 fJ (green), and > 20 fJ (red).
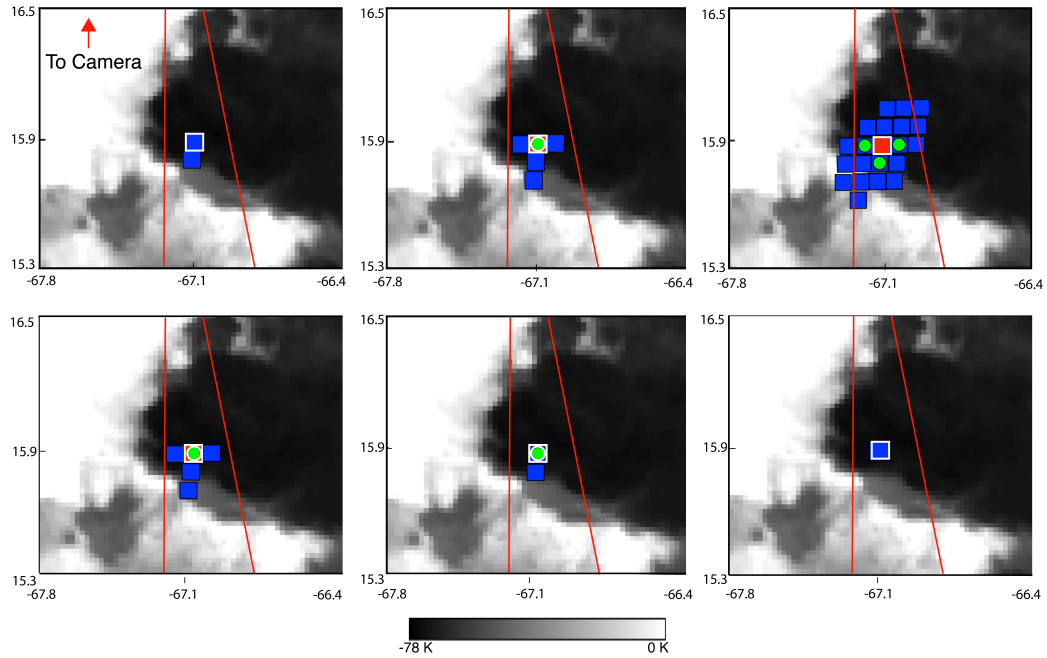
Figure 4.2: Geostationary Lightning Mapper events (colored shapes) overlaid on GOES-R infrared (channel 13) images for video frames 3-8 of Figure 4.1. The colors correspond to different optical energies, with large optical energies in red (> 20 fJ), medium optical energies in green (10-20 fJ), and small optical energies in blue (< 10 fJ). The vertical axis of each panel corresponds to latitude and the horizontal axis to longitude. The video camera is located to the north (approximately 18° latitude, -67° longitude). The lines indicate the camera field of view associated with each panel in Figure 4.1.

The GLM signature of the GJ occurs near the coldest cloud tops (Figure 4.2), which are around 195 K. In Figure 4.2, frame 3, only two GLM pixels are illuminated and they are adjacent to each other, both being of small optical energy (<10 fJ). Most of the detections come from the pixel outlined in white (Figure 4.3,

frame 3), which corresponds to the azimuth of the GJ. During frame 4, which is the last video frame before the GJ jumps to the ionosphere, the GLM detections with larger optical energies come from the pixel outlined in white.
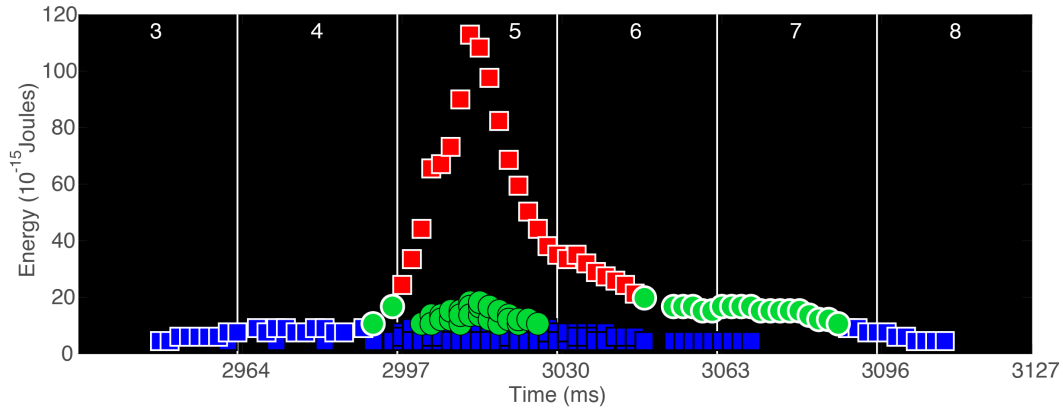
Figure 4.3: Time series of GLM optical energy for the 08:46 UTC gigantic jet. The colors correspond to different optical energies, with large optical energies in red (> 20 fJ), medium optical energies in green (10-20 fJ), and small optical energies in blue (< 10 fJ). The markers outlined in white correspond to the GLM pixel in Figure 4.2 that is outlined in white. GLM = Geostationary Lightning Mapper.

When the GJ connects with the ionosphere (frame 5), a maximum in GLM event detections is observed with a spread of optical energies across a large region of the cloud top. The largest optical energies (> 20 fJ) are again located in the pixel outlined in white. Adjacent to this pixel are events with the next highest optical energies (10-20 fJ). Finally, the remainder of the GLM events are of lower optical energy (< 10 fJ) and surround the higher optical energy pixels. The optical energy peaks at the location of the pixel that corresponds to the azimuth of the GJ (white outlined pixel), then decreases radially outward away from this pixel. Figure 4.3 shows a drastic spike in the optical energy of the white outlined pixel, reaching a value approximately 115 fJ, which occurs during the connection between the upward discharge and the lower ionosphere shown in frame 5 of Figure 4.1.

Although the optical energies of the surrounding pixels are also increased during this time period, the optical energy of the pixel outlined in white is increased by a factor of 20.

After the connection with the ionosphere (frame 5), the number of detections and their associated optical energies decrease, but the majority of the detections still come from the pixel outlined in white. Finally, this pixel is the only illuminated pixel starting midway in frame 7, and then the detections cease during frame 8. Interestingly, frames 9 and 10 do not appear much dimmer than frame 8 from the video images (Figure 4.1) and they also appear brighter than frames 1-3, but they do not have any GLM detections. As mentioned previously, this is most likely due to the fact that GLM has a dynamic detection threshold, which changes based upon past detections [*Goodman et al.*, 2013; *Bitzer*, 2017]. Future analysis of GLM level 0 data (without the operational ground processing) will need to be analyzed to verify this. Also, the GJ and cloud top are saturated in frames 4-10 of the video images (Figure 4.1), so it is impossible to reliably evaluate the relative optical brightness during these times, so frames 9 and 10 could actually be much less bright than the preceding frame.

GLM properties for all the distinguishable GJ signatures from Tropical Storm Harvey are shown in Table 4.1. Also shown are the properties for all other GLM flashes detected for the day of 19 August 2017, and some properties of oceanic lightning reported by *Rudlosky et al.* [2018]. Most of the GLM properties presented in Table 4.1 are standard data products of GLM [*Goodman et al.*, 2013], except for maximum series duration and maximum group separation distance. Maximum series duration is defined as the duration of continuous GLM detection for a flash and maximum group distance is defined as the farthest lateral distance between

Table 4.1: GLM properties of gigantic jet flashes, all other flashes from 19 August 2017, and oceanic flashes from *Rudlosky et al.* [2018]. Also shown is the mean peak current (I_{pk}) from GLD360 detections associated with each GJ. The values in parentheses to the right of the UTC times are the durations of the visible GJs obtained from the video images in ms.

Gigantic Jet Flashes

UTC Time	Max Series Duration (ms)	Max Event energy (fJ)	Flash area (km^2)	Flash energy (fJ)	Max Group distance (km)	Flash duration (s)	GLD360 mean I_{pk}
4:19:54 (333)	44	21.3	652.5	494.4	10.1	0.486	21
4:21:15 (133)	42	16.7	801.8	828.6	10.1	0.224	52
4:24:46 (300)	168	48.8	726.1	1362.7	12.7	0.708	33
6:12:39 (341)	52	28.9	804.9	862.1	2	1.18	12
6:39:01 (234)	56	16.4	499.7	117.5	3.7	0.044	13
7:01:53 (197)	20	41.2	1179.4	1039.2	2	0.64	18
7:18:33 (234)	18	24.4	1254.3	682.1	2.8	0.886	16
7:25:41 (240)	16	13.7	821.9	225.8	20.4	0.196	21
8:14:38 (267)	24	16.7	502.7	57.9	12.9	0.028	9
8:46:02 (462)	160	112.9	1709.2	3067.2	2.5	0.724	15
8:50:16 (467)	100	28.5	879.8	1030	6.4	0.444	14
Mean:	64	33.6	893.8	887.9	7.8	0.505	20
SD:	55	28.5	359.5	833.1	6	0.364	12
08/19/2017							
Mean:	7	23.8	1003.6	377.5	16.8	0.295	-
SD:	10	34.6	609.02	632.6	12.4	0.262	-
Rudlosky et al. 2018							
Mean:	-	-	570	420	-	0.345	-
SD:	-	-	-	-	-	-	-

groups for a flash [*Peterson et al.*, 2017b,a]. Considering most flashes detected from space based detectors appear as a set of many groups, maximum group distance is an estimate of the lateral size of the lightning flash [*Peterson et al.*, 2017b]. For each GLM property in Table 4.1, the mean and standard deviation are included when possible.

Table 4.1 shows the GJ signatures exhibit longer maximum series and flash durations, larger maximum event and flash optical energies, and smaller maximum group distances when compared with other flashes detected by GLM. The most pronounced difference between the GJ and the other flashes is the maximum series duration. The mean for GJs is nearly ten times larger than that of the

other flashes. The GJ flashes also exhibit about two times greater maximum flash optical energy. The mean maximum group distance for the GJ flashes is about one half the values for other flashes detected on that day. The mean flash area of the GJ signatures and other flashes was about the same, but the mean flash area reported by *Rudlosky et al.* [2018] was about one half of these values. The study of *Rudlosky et al.* [2018] documented the GLM lightning distributions during the initial 9 months in the operational GOES-East position (December 2017 to August 2018). The discrepancy may be a result of the relatively small sample size of the flashes from 19 August 2017 ($\approx$ 600,000) compared to the flashes presented in *Rudlosky et al.* [2018] ($\approx$ 237,000,000). In summary, the GLM GJ signatures exhibit long continuous emissions, large optical energies, and short lateral propagation distances in comparison with other flashes detected by GLM.

4.4 Summary and Discussion

The GJ GLM signatures of long continuous emissions, large optical energies, and short lateral propagation distances are consistent with the fact that GJs generally have long continuing current and charge transfer over a relatively long period of time [*Cummer et al.*, 2009; *Liu et al.*, 2015c]. In contrast, ordinary flashes observed by space based lightning detectors [*Peterson et al.*, 2017a] often have short durations of continuous emission and have relatively large group propagation distances. For flashes observed by GLM on 19 August 2017 that have large optical energies, they also have large group propagation distances (large lateral flashes). The GJ flashes typically have their brightest pixel stationary over long periods of time (multiple GLM frames or tens of ms), while the location of the brightest pixel

57

of a typical flash changes rapidly, which is due to the laterally propagating leader in the horizontally expansive thundercloud charge regions.

The duration of continuous emissions (maximum series duration) should have been larger for the GJs identified, but due to the dynamic detection threshold employed by GLM, the later stage of the GJs was often not detected. The dynamic detection threshold continuously updates the background scene by averaging over several frames on a pixel-by-pixel basis, and then subtracts the background estimate from the current signal [*Goodman et al.*, 2012a]. If the current signal is larger than the background estimate, then it is considered to be a detection. This detection method works well for ordinary lightning, as it emits discrete pulses that last less than a few GLM frames. However, for GJ lightning the signal lasts for tens of GLM frames and the peak in optical energy (when connection with the ionosphere occurs) happens well before the end of the optical emissions of the GJ. Thus, the background estimates that include the peak in optical energy would significantly raise the detection threshold, and the signals detected after this will most likely not be considered detections. In addition, the signals may not have exceeded the individual pixel threshold for detection. This may explain why no GLM detections occurred after video frame 8 (Figures 4.1 and 4.2), even though the subsequent video frames of the GJ (and cloud top) appeared much brighter than the first video frame with GLM detections (video frame 3).

Other lightning flashes that also exhibit continuous emissions as detected by space based imagers are cloud-to-ground discharges (CG) with long continuing current [*Bitzer*, 2017]. Future work may characterize the GLM detections of continuing current CG discharges, and compare/contrast this to GJ signatures. Even if ground-based video observations are unavailable, it may be possible to com-

bine GLM data with other lightning measurements to distinguish GJs from long continuing current CGs. For example, lightning detection systems such as the National Lightning Detection Network do not register a lightning event when the GJ connects to the ionosphere, but only detect the initial intracloud pulses associated with the GJ. Thus, if a potential GJ or a continuing current CG is detected by GLM and it only has associated IC pulses and no CG strokes, it is likely to be a GJ. Reliably detecting GJs from geostationary orbit could greatly increase our knowledge of how frequently they occur, where they occur, and what storm systems produce them. This will also allow comprehensive studies on the meteorological and electrical properties [*Meyer et al.*, 2013; *Lazarus et al.*, 2015; *Boggs et al.*, 2018] of the parent storms.

As shown in Figures 4.2 and 4.3, the detections with the largest optical energies come from the pixel outlined in white, which corresponds to the azimuth of the GJ (dotted lines in Figure 4.1). This is true for every video frame for the duration of the GJ signature. A possible implication is the large optical energies are being emitted by the GJ channel above the cloud, or at least the base of it, rather than the in-cloud lightning leaders associated with the GJ. Interestingly, the cloud top from frames 4-8 in Figure 4.1 is lit up very bright, similar to the GJ above the cloud, and the lateral width of the bright cloud top is around 40 km, which corresponds to multiple GLM pixels. If the bright cloud top was producing the large optical energies, then GLM would have detected multiple pixels with optical energies > 20 fJ, instead of just one pixel. It would be reasonable that detections of the GJ above the cloud are optically bright, because there is no cloud to scatter and attenuate the light. Also, considering GJs are composed of a vertically oriented channel, localized GLM detection is expected and integration of the emission source along

the vertical channel will also contribute to increasing the contrast between that pixel and the surrounding pixels. From the video images (Figure 4.1), the bright channel segment reaching 26 km altitude in frames 11-14 resembles a bright return stroke channel. If GLM indeed observes the GJ above the cloud, this would indicate that at least some portion of the GJ channel emits at the 777.4 nm band. ISUAL detected GJs also showed some emissions at the 777.4 nm band [*Kuo et al.*, 2009; *Chou et al.*, 2010], but it is difficult to tell if these emissions were from the GJ or the lightning inside the cloud. Considering streamers do not emit at this band in the upper atmosphere [*Kanmae et al.*, 2007, 2010] these results may indicate some portion of the GJ above the cloud is composed of a leader.

Chapter 5

Past Studies in Lightning Spectroscopy

Studies on lightning spectroscopy have been performed for nearly a century, using slit and slitless spectrographs, and using time-integrated and time-resolved techniques. These past studies focused on cloud-to-ground (CG) discharges, as CG discharges are primarily oriented vertically and act as their own slit. To create the spectra, prisms, gratings, or a combination of the two (termed 'grisms') were placed in front of a camera or recording device. The dispersion was usually set horizontally, as the CG lightning channel was oriented vertically. Many of the first spectra obtained were from astronomical observatories studying the aurora and faint stars, with the astronomers pointing their equipment at nearly storms out of curiosity.

The first photographs of the lightning spectrum were obtained in the early twentieth century by placing a prism in front of an astronomy telescope [*Pickering*, 1901]. This spectrum was time-integrated and was slitless, recording the

lightning spectra between 380-600 nm. Another study similar to *Pickering* [1901] was also performed using a time-integrated slitless spectrograph, finding similar results [*Fox*, 1903]. These studies were not able to accurately attribute the emissions to specific wavelengths due to not using a slit, as when the emission source position in a slitless spectrograph changes relative to the spectrograph the spectrum is shifted, making it difficult to understand which emission lines belong to which wavelengths. From the emissions they observed, they assumed certain lines coincided with the Balmer series of hydrogen. A study published in 1917 [*Slipher*, 1917] used a slit for the first time to obtain the spectrum of lightning, and with a comparison spectrum, was able to make accurate wavelength determinations of the emission lines. That study concluded the spectrum was consistent with emissions of spark discharges in dry air, which were obtained from lab experiments. The first study to capture and correctly identify the H-alpha (Balmer Series) emissions from lightning was published in 1941 [*Israel and Wurm*, 1941]. The authors this time reported on the visible spectra up to 660 nm, allowing them to observe the strong H-alpha emission at 656.3 nm due to the dissociation of water vapor in the atmosphere.

Optical lightning spectroscopy saw a dramatic increase in studies during the 1960's and 1970's [*Salanave*, 1961; *Prueitt*, 1963; *Uman*, 1964; *Uman and Orville*, 1965; *Krider*, 1965; *Orville*, 1968a,b, 1975]. These studies sought to resolve the spectral features of the components in the lightning flash, which the previous studies had failed to do. The work in *Salanave* [1961] published the optical spectrum of lightning ranging from 400 to 620 nm using a slitless, time-integrated spectrograph. This study correctly identified all the dominant spectral emission lines from lightning in this region, which primarily consisted of singly ionized atomic Nitro-

gen and Oxygen. *Prueitt* [1963] was the first to use the spectra of lightning to estimate physical properties of the lightning channel, studying five return strokes with a time-integrated spectrograph. From the spectra, the author was able to estimate the peak temperature of the lightning channel (more detail below). From here on, much of the work focused on using the results of emission spectroscopy to determine physical parameters of the lightning channel, such as the temperature and electron density, and the assumptions needed to carry out this work [*Uman*, 1964; *Uman and Orville*, 1965]. The first time-resolved spectroscopy studies on the lightning channel were performed in *Krider* [1965] and *Orville* [1968a]. *Krider* [1965] obtained time-resolved spectra by using using filters centered around specific spectral lines with narrow bandwidth and used photocells to measure the intensity as a function of time. The work in *Orville* [1968b] used a combination of a high-speed streaking camera, a grism, and a horizontal slit (shown in Figure 5.1) to isolate a narrow part of the vertical channel, and gave the first time-resolved temperature and electron density estimates of a lightning return stroke.

Modern day spectrographs have recently been constructed to image lightning using a combination of high-speed charge coupled device (CCD) or complementary metal-oxide semiconductor (CMOS) cameras and gratings/prisms/grisms [*Warner et al.*, 2011; *Qu et al.*, 2011; *Cen et al.*, 2015; *Chang et al.*, 2017; *Walker and Christian*, 2017]. The significant advances in high-speed cameras have led to new capabilities for imaging the lightning spectrum. Not only are these instruments very sensitive, allowing dimly lit features to be observed, but the whole lightning channel can also be recorded while the spectra is time-resolved. Previously, time-resolved spectra used a slit to capture the spectra of a small channel segment due to the imaging unit being a rotating drum. With modern high-speed cameras the
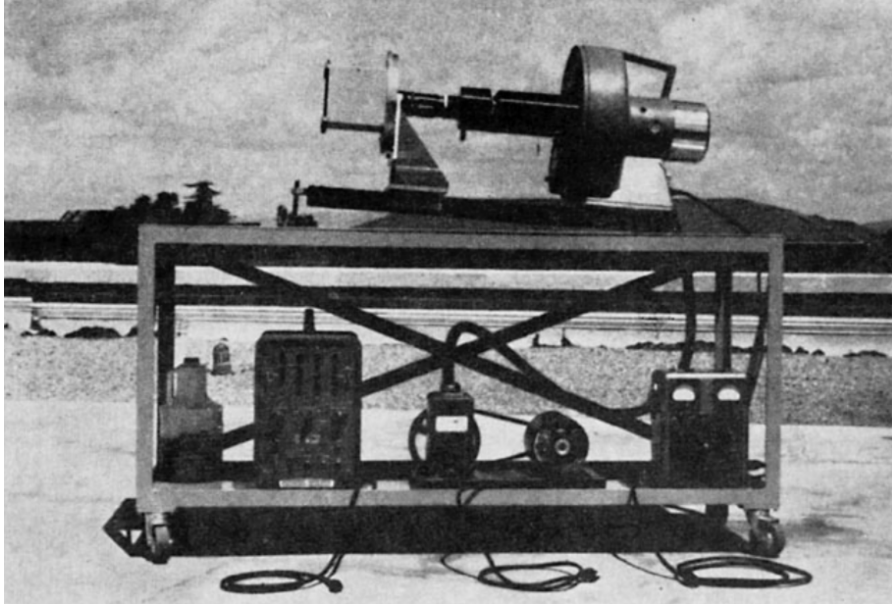
Figure 5.1: High-speed spectroscopy system from *Orville* [1968a].

imaging unit is a 2D pixel plane with fast update times (a few to hundreds of microseconds), allowing the camera to capture the entire discharge channel with fine time resolution.

5.1 Methods for Calculating Lightning Channel Parameters

As mentioned above, it is possible to estimate lightning channel parameters, such as temperature and electron density, from the lightning spectra. To estimate the temperature, this is done by comparing the ratio of intensities of two spectral lines that are from the same atomic species [*Prueitt*, 1963; *Uman*, 1966; *Orville*, 1968b]. Some intensity ratios as a function of temperature are shown in Figure 5.2 for neutral emission lines. This method has the following assumptions: the
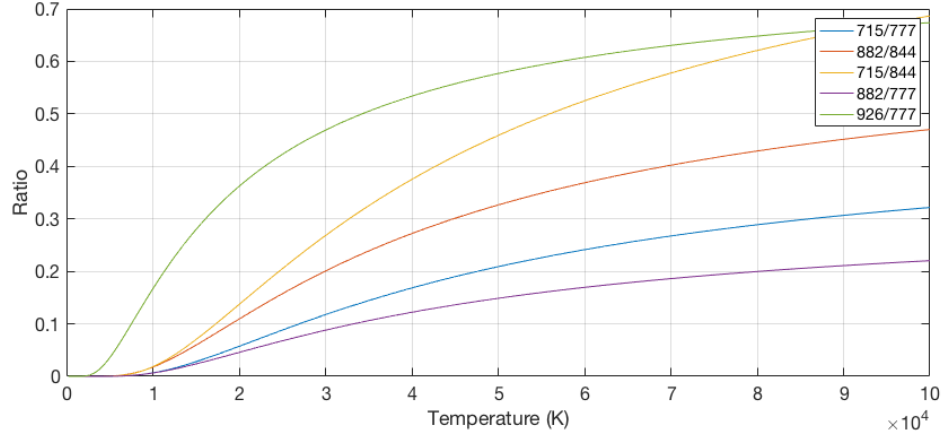
Figure 5.2: Temperature as a function of intensity ratio for multiple spectral lines. The spectral line ratios in the legend are wavelengths in nm.

lightning channel is optically thin, the cross-section of the channel has uniform temperature, and the discrete energy levels of a spectral line used to calculate the temperature must follow Boltzmann statistics (local thermodynamic equilibrium or LTE) [*Uman*, 1966; *Walker and Christian*, 2019].

For the temperature calculation, under conditions of LTE the atomic energy levels within an ionization state are populated according to Boltzmann's statistics:

$$N_n = \frac{N_0 g_n}{B(T)} exp\left(\frac{-E_n}{kT}\right) \tag{5.1}$$

where N_n is the number of atoms in energy level n, N_0 is the total number of atoms, E_n is the excitation energy of the nth level, k is the Boltzmann constant, T is the electron temperature, g_n is the statistical weight of the level, and $B(T)$ the partition function. With the assumption that the lightning channel is optically thin, which is the case for neutral and singly ionized Nitrogen and Oxygen [*Uman and Orville*, 1965], the intensity of an emission line from a gas per unit volume at

65

uniform temperature and density due to transitions from energy level n to r is

$$I_{nr} = KN_n A_{nr} h\nu_{nr} \qquad (5.2)$$

where A_{nr} is the Einstein coefficient for transition probability, ν_{nr} is the frequency of the emitted photon, h is Plancks constant, and K is a geometric factor. A similar equation can be written for a gas with transitions from energy levels m to p

$$I_{mp} = KN_m A_{mp} h\nu_{mp}. \qquad (5.3)$$

By combining equations 5.1 and 5.2, the intensity is written as

$$I_{nr} = K\left[\frac{Ng_n}{B(T)} exp\left(\frac{-E_n}{kT}\right)\right] A_{nr} h\nu_{nr}. \qquad (5.4)$$

Similarly, equation 5.3 can be written as

$$I_{mp} = K\left[\frac{Ng_m}{B(T)} exp\left(\frac{-E_m}{kT}\right)\right] A_{mp} h\nu_{mp}. \qquad (5.5)$$

After dividing equation 5.4 by equation 5.5, an expression is found relating the intensities of two emission lines to the temperature:

$$\frac{I_{nr}}{I_{mp}} \cdot \frac{A_{mp}\nu_{mp}g_m}{A_{nr}\nu_{nr}g_n} = exp\left(\frac{E_m - E_n}{kT}\right) \qquad (5.6)$$

and by solving for T, the following expression is found:

$$T = \frac{E_m - E_n}{kln\left[\frac{I_{nr}A_{mp}\nu_{mp}g_m}{I_{mp}A_{nr}\nu_{nr}g_n}\right]}. \qquad (5.7)$$

66

This is the expression to calculate the electron temperature from the lightning channel, which is only a function of the ratio of the intensities of two spectral lines, as $E, A, g,$ and ν are constants that can be found in tables from the National Institute of Standards and Technology (NIST, website: https://www.nist.gov/pml/atomic-spectra-database). To estimate an accurate temperature, $|E_m - E_n|$ should be greater than kT [*Uman*, 1966]. When the spectral resolution of a spectrograph is not able to separate individual spectral lines for the intensity ratio, as in the case of multiplets, the following expression is used for the intensity ratio [*Walker and Christian*, 2019]:

$$\frac{I_T}{I_3} = \frac{I_1 + I_2}{I_3} = \frac{g_1 A_1 \nu_1 exp(\frac{-E_1}{kT}) + g_2 A_2 \nu_2 exp(\frac{-E_2}{kT}) + g_3 A_3 \nu_3 exp(\frac{-E_3}{kT})}{g_4 A_4 \nu_4 exp(\frac{-E_4}{kT})}. \quad (5.8)$$

When Equation 5.8 is plotted with intensity as a function of temperature (all over terms are constant in this equation), a relationship between intensity ratio and temperature is found (similar to Figure 5.2), which allows estimation of the temperature from spectral measurements. To estimate the uncertainty in temperature, error propagation is performed on equation 5.7, with $\frac{I_{nr}}{I_{mp}} = R$ and $\frac{\nu_{mp}g_m}{\nu_{nr}g_n} = G$.

$$T = \frac{E_m - E_n}{kln(RG\frac{A_{mp}}{A_{nr}})} \quad (5.9)$$

But, G is assumed to have a much smaller uncertainty than the intensity ratio and Einstein coefficients, giving an equation of the uncertainty as

$$\delta T^2 = \left(\frac{\partial T}{\partial R}\right)^2 \delta R^2 + \left(\frac{\partial T}{\partial A_{mp}}\right)^2 \delta A_{mp}^2 + \left(\frac{\partial T}{\partial A_{nr}}\right)^2 \delta A_{nr}^2. \quad (5.10)$$

By taking each partial derivative of Equation 5.9, which has the form of

$$\frac{\partial T}{\partial X} = \frac{\partial}{\partial X}\left(\frac{C}{ln(aX)}\right) \rightarrow \frac{\partial T}{\partial X} = \frac{-C}{Xln^2(aX)} \qquad (5.11)$$

where X is either R, A_{mp}, or A_{nr} and C and a are constants, equation 5.10 can be written as

$$\delta T^2 = \left(\frac{-C\delta R}{ln^2(aR)R}\right)^2 + \left(\frac{-C\delta A_{mp}}{ln^2(aA_{mp})A_{mp}}\right)^2 + \left(\frac{-C\delta A_{nr}}{ln^2(a/A_{nr})A_{nr}}\right)^2. \qquad (5.12)$$

After factoring out the common terms and substituting back in for C and a and taking the square root, the uncertainty in the temperature is

$$\delta T = \left(\frac{E_m - E_n}{kln^2(RG\frac{A_{mp}}{A_{nr}})}\right)\sqrt{\left[\left(\frac{\delta R}{R}\right)^2 + \left(\frac{\delta A_{mp}}{A_{mp}}\right)^2 + \left(\frac{\delta A_{nr}}{A_{nr}}\right)^2\right]}. \qquad (5.13)$$

In equation 7.1.2, the uncertainty in temperature is due to the uncertainty in the intensity ratio (δR) and the uncertainties of the Einstein coefficients $(\delta A_{mp}, \delta A_{nr})$. Most Einstein coefficients are known to a few percent, which means the uncertainty in the intensity causes the most uncertainty in a temperature estimate.

5.2   Spectra Derived Temperature of Lightning Return Strokes

From past studies most of the spectra obtained were from lightning return strokes. Some of those studies not only reported on the emission features of the return stroke spectra, but also performed quantitative spectroscopy by calculating the

return stroke temperature. This was done by using the formulation described in section 5.1 or similar methodology. The first study to calculate the return stroke temperature was *Prueitt* [1963], who estimated the temperature from five return strokes. This was with a time-integrated, slitless spectrograph, and an example
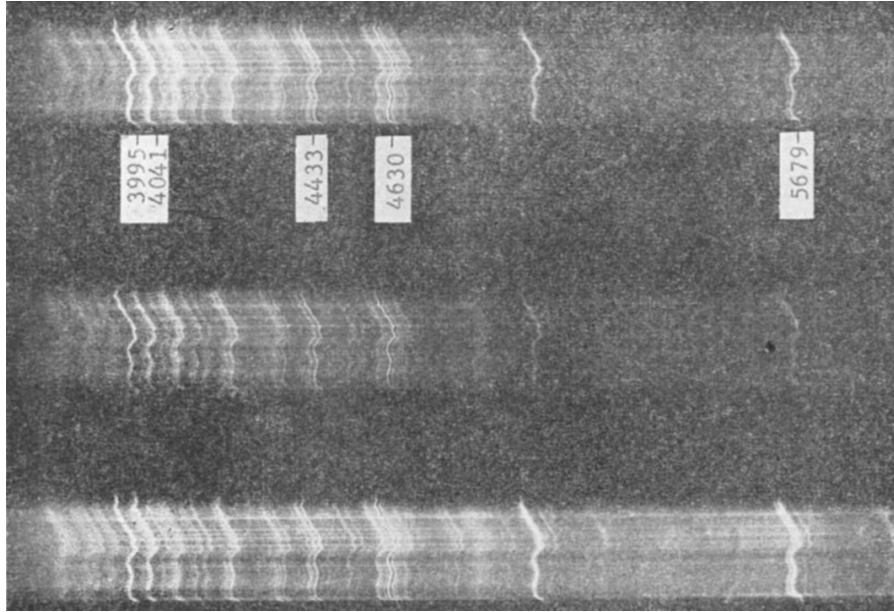
Figure 5.3: Slitless lightning spectra from *Prueitt* [1963]. The labeled numbers represent wavelengths in Angstroms of singly ionized Nitrogen.

spectra is shown in Figure 5.3. The temperature was estimated with the spectral lines 399.5 nm, 404.1 nm, 443.3 nm, 463.0 nm, and 568.0 nm, which are all singly ionized Nitrogen. Calculated temperatures ranged from 24,200 K to 28,400 K, with uncertainties of 400-1,000 K. Considering the spectra were time-integrated, the reported temperatures represented the average temperature of the return stroke [*Uman*, 1964].

The next study to calculate the temperature of lightning return strokes was *Orville* [1968b], using the time-resolved spectrograph shown in Figure 5.1. *Orville* [1968b] reported on the temperatures of ten return strokes, from a 10 m section

of the channel, with 5 μs time resolution. An example spectrum from this study is shown in Figure 5.4. The peak temperatures calculated from this study ranged from 28,000 K to 31,000 K, with uncertainties of 3,000 to 7,000 K. The largest temperature calculated was 36,000 K. With the fine time resolution, the evolution of the return stroke temperature was presented; the return stroke temperatures were found to decrease quickly, by more than 50% 20 to 50 μs after the onset of the peak temperature.

From modern day slitless spectrographs, *Qu et al.* [2011] found the temperatures of three flashes with multiple return strokes ranged from 27,140 K to 33,890 K. The authors did not report which lines they used for the temperature estimation, or what the uncertainty in the temperature calculations were. It was also not reported what portion of the channel they used or what their time resolution was. They found that the total intensity of the spectral lines was proportional to the amplitude of the electric field and the energy transmission of a return stroke. *Walker and Christian* [2019] obtained spectra from rocket-triggered lightning with a slitless spectrograph using a high-speed camera from a flash with multiple return strokes. The spectra ranged from 380 nm to 870 nm, had time resolution of 1.5 μs, and were derived from a small segment of the channel. The spectra are shown in Figure 5.5. The peak currents from the flash and return strokes ranged from 8.1 kA to 17.3 kA. The peak temperatures of the return strokes ranged from 32,000 K to over 40,000 K with uncertainties of 2,000 to 4,000 K, and all of the strokes showing rapid reduction of the temperature after 5 to 10 μs. This study concluded that they observed larger peak temperatures than previous studies due to the smaller integration time (1.5 μs), which was smaller than previous studies by a factor of two or more. A summary of these studies is presented in Table 5.1.
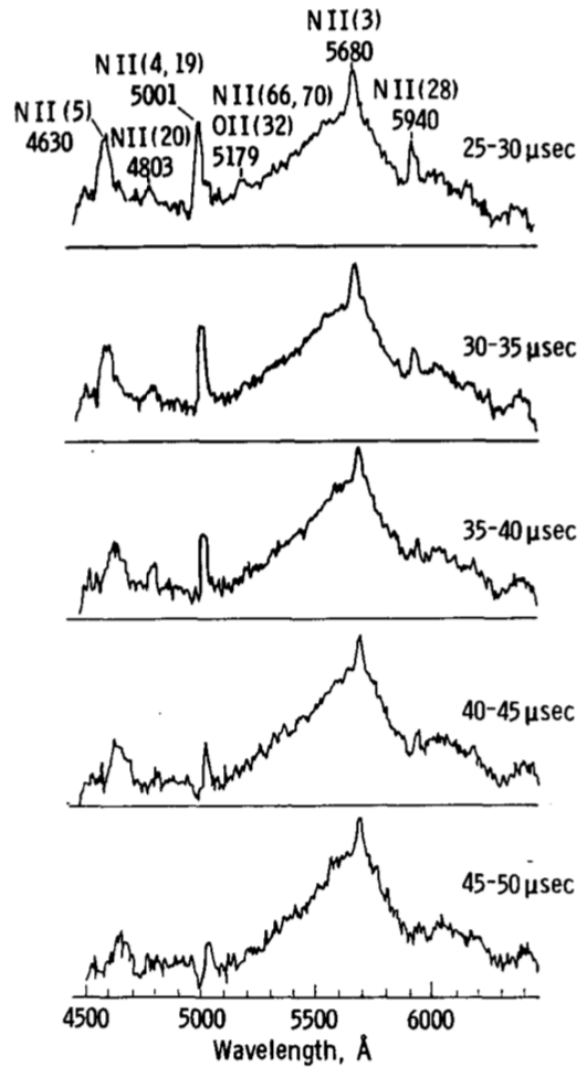
Figure 5.4: Return stroke spectra from *Orville* [1968b].

5.3   Spectrum-Derived Temperature of Lightning Leaders

Studies reporting on the spectra of lightning leaders have been far fewer in the literature, especially those that calculate the temperature of the leader channel. Capturing the lightning leader spectrum is a difficult task, as they are usually much

71
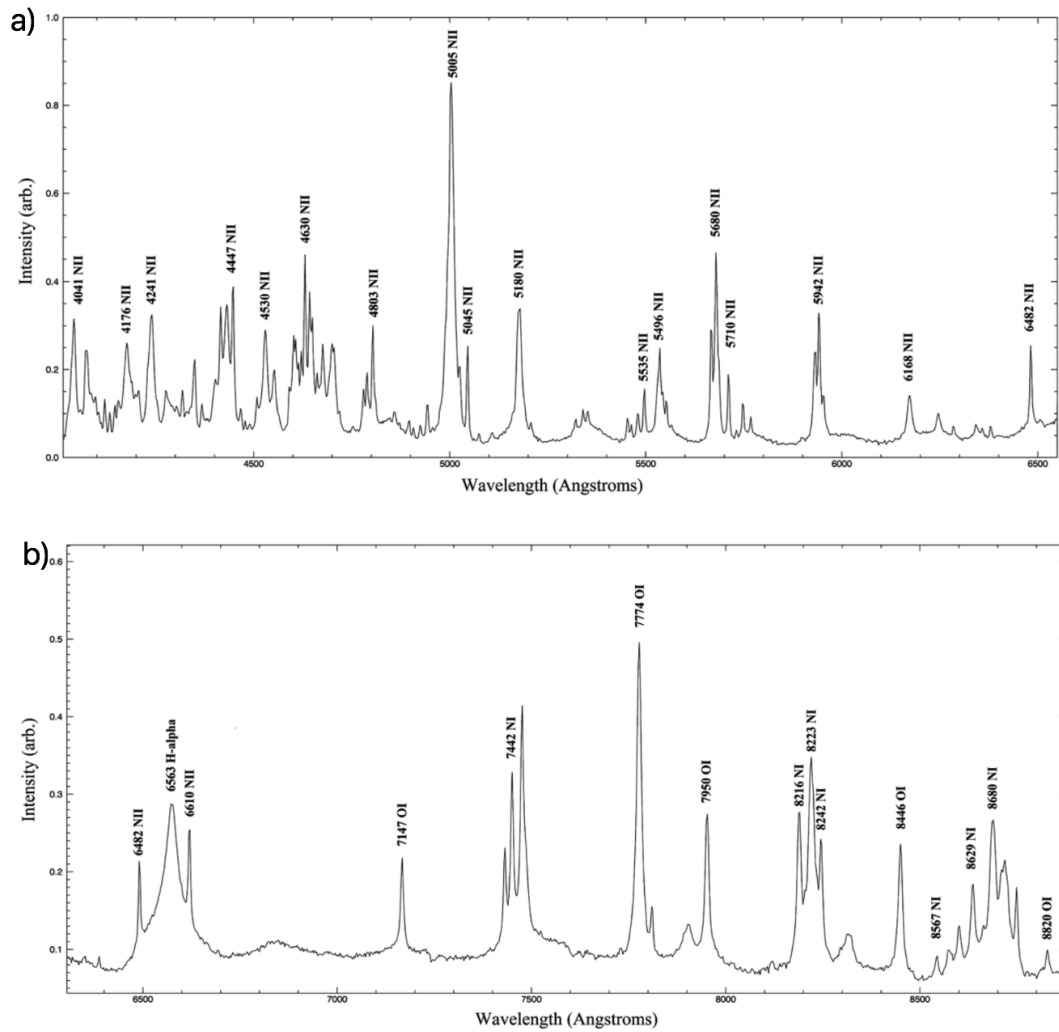
Figure 5.5: Top) Triggered lightning spectra from *Walker and Christian* [2017] for lower optical wavelengths < 650 nm. (Bottom) Triggered lightning spectra from *Walker and Christian* [2017] for upper optical wavelengths > 650 nm.

dimmer than lightning return strokes. The initial stepped lightning leader of a flash is often the most dim, but if there are multiple return strokes, the preceding dart leaders can also appear very dim. From the literature, there are only three studies that estimate the temperature of lightning leaders, with two of those studies from equipment originating from the 1960's.

Table 5.1: Summary of studies reporting on the lightning return stroke channel temperature.

Study	Lines Used (nm)	Time Resolution (μs)	Temperature (K)	Uncertainty (K)
Prueitt [1963]	399.5, 404.1, 443.3, 463.0, 568.0	-	24,200 to 28,400	400 to 1,000
Orville [1968b]	463.0, 500.0	2 to 5	28,000 to 31,000	3,000 to 7,000
Qu et al. [2011]	-	-	27,000 to 33,000	-
Walker & Christian [2019]	648.2, 661.0, 715.7, 777.4	1.5	32,000 to 40,000	2,000 to 4,000
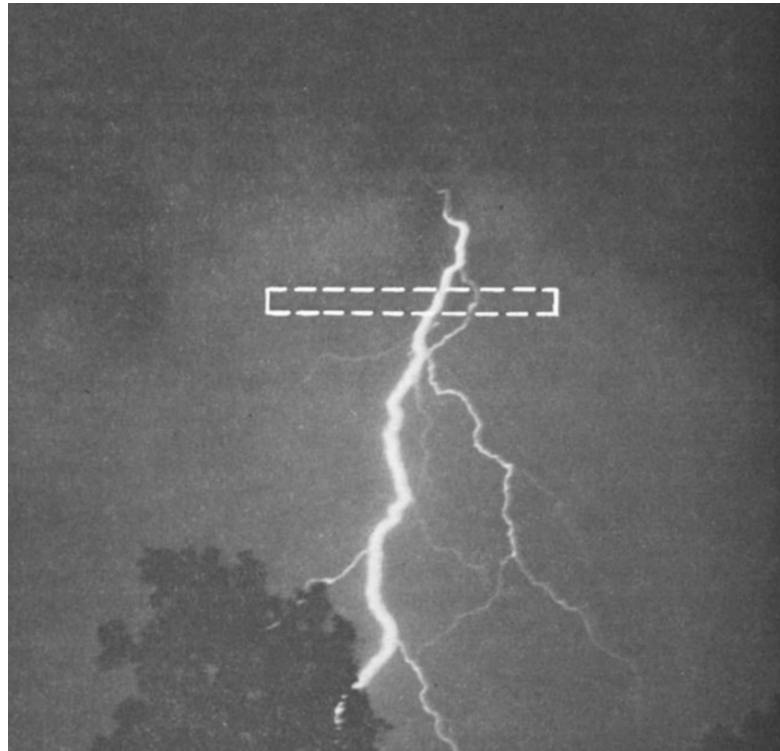
Figure 5.6: Lightning discharge producing the leader spectra in *Orville* [1968]. The dashed white box represents the spectrograph field-of-view.

The first study to report on the spectrum of a lightning stepped leader was *Orville* [1968]. The author analyzed a 2 m section of a downward stepped negative leader, which is shown in Figure 5.6. The equipment used for this study was the same as that used in *Orville* [1968a,b] for lightning return strokes (pictured in Figure 5.1). The leader spectra had 20 μs time resolution, and included wavelengths from 560 to 660 nm. The leader spectra were analyzed about 220 μs before the return stroke, and the leader channel was only visible when it made discrete steps. Five total steps were recorded before the onset of the return stroke, with time between steps of 31 to 42 μs. This spectrum is shown in Figure 5.7. From the emissions, spectral lines were observed at 568.0 nm (NII), 594.2 nm (NII), 615.7 nm (NII), and 656.3 nm (H-alpha). Most of the emissions were from singly ionized Nitrogen except H-alpha, which did not step similar to the other lines, but was observed continuously. Even though the leader was visible for five steps, the temperature was only calculated from one step due to the weak intensities from the other steps. The temperature was calculated from the spectral lines of 568.0 nm and 594.2 nm using the methodology in section 5.1, and was found to be 30,000 K, with uncertainties of 5,000 to 10,000 K. Due to the singly ionized lines getting dimmer and the neutral lines getting brighter, it was concluded that the leader channel was cooling as it approached the ground. It was speculated that during the neutral emissions (OI and NI), the leader channel should have been below 20,000 K. This study also speculated that positive leaders should have cooler temperatures and mostly emit neutral lines, due to positive leaders appearing smooth and continuous, with little variation in light output.

Another study by Richard Orville, using the same equipment, reported on the spectra of five dart leaders [*Orville*, 1975]. The dart leaders were part of a flash
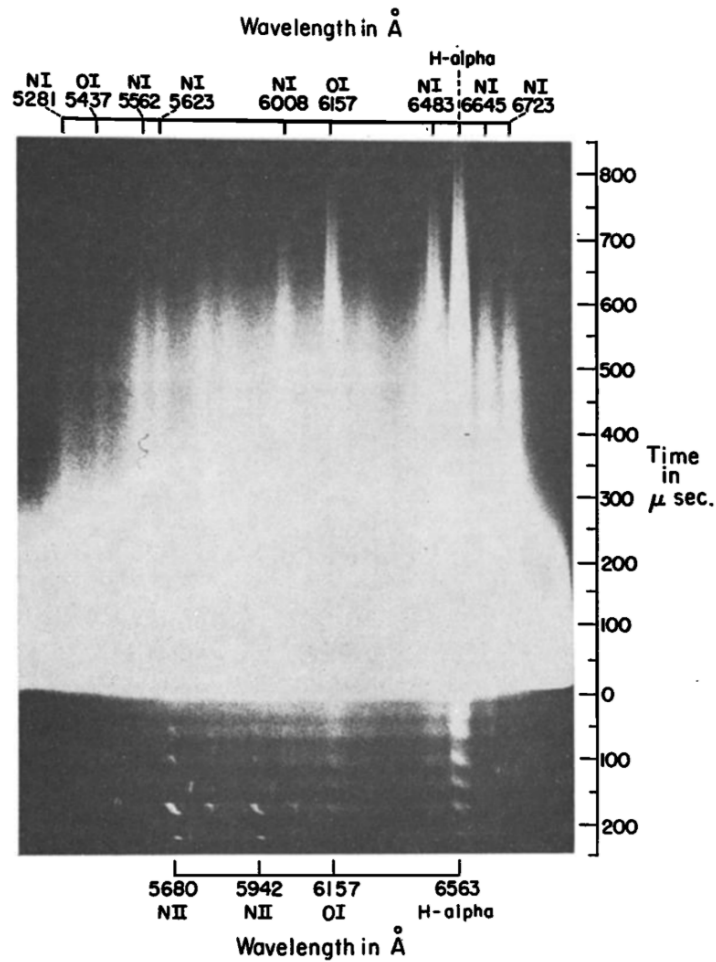
Figure 5.7: Time resolved spectra for the lightning leader and return stroke reported on in *Orville* [1968].

that had at least thirteen return strokes. The original stepped leader was too dim to record, but three of the dart leader spectra were bright enough to calculate the temperature. A 13 m section of the dart channel was analyzed, and each dart leader was analyzed for one time step, with time resolution of 9 μs. The spectra spanned the wavelengths of 390 to 510 nm, and included emissions from 444.7 nm (NII), 463.0 nm (NII), and 500.1 nm (NII). The spectra is shown in Figure 5.8. The lines of 444.7 nm and 463.0 nm were used for the temperature calculation,

75
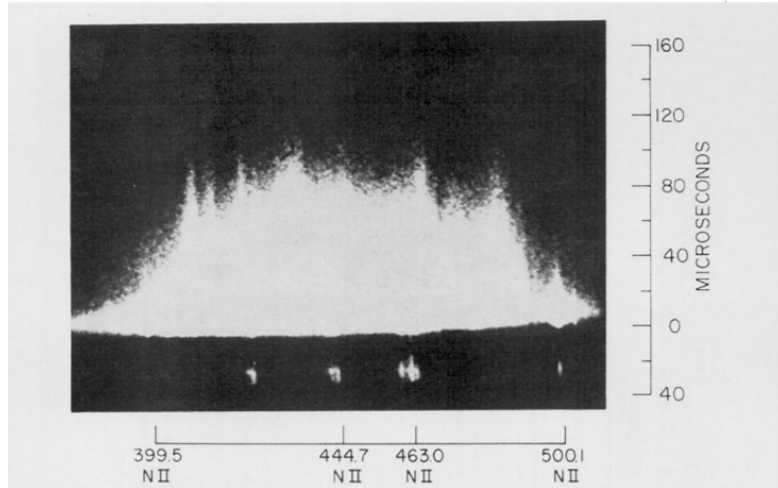
Figure 5.8: Time resolved spectra for a lightning dart leader and return stroke reported on in *Orville* [1975]. The x-axis values are in nm.

finding an average temperature of 20,000 K with 2,000 K uncertainty. The dart leader emissions were observed continuously before the return stroke.
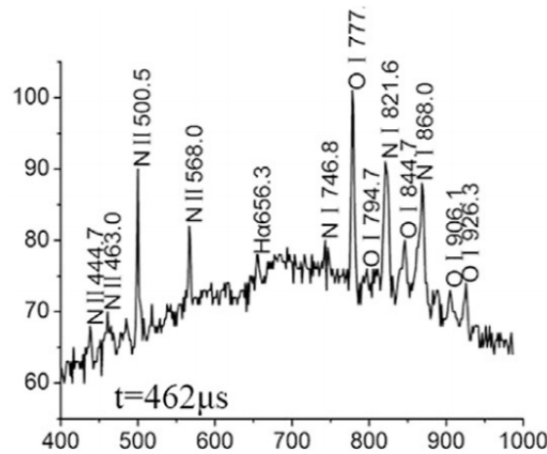
Figure 5.9: Leader spectra from the study of *Chang et al.* [2017].

A study using modern day equipment consisting of a high-speed CCD camera and grating reported on the spectra of a stepped and dart leader [*Chang et al.*, 2017]. The spectra were from the wavelength range of 400-1000 nm with 150 μs time resolution. For the stepped leader spectra, ten frames were analyzed,

76

Table 5.2: Summary of studies reporting on the lightning leader and dart leader channel temperature.

Study	Lines Used (nm)	Time Resolution (μs)	Temperature (K)	Uncertainty (K)
Orville [1968d]	568.0, 594.2	20	30,000	5,000 to 10,000
Orville [1975]	444.7, 463.0	9	20,000	2,000
Chang et al. [2017]	-	150	15,000 (L); 21,000 (DL)	-

and an example spectrum is shown in Figure 5.9. This study did estimate the temperature of the leader channel, but it did not say what spectral lines were used for the calculation or what the uncertainties were. They estimated the leader tip to be 15,000 K and the leader channel to be 14,000 K. For the dart leader, the average temperature found was 21,000 K. A summary of these studies is presented in Table 5.2.

Chapter 6

High-Speed Spectrograph Construction

6.1 Scientific Instrumentation

The spectroscopy system was assembled and designed in order to observe lightning leader and return stroke spectra, as well as spectra from Transient Luminous Events such as starters, jets, gigantic jets, and sprites. From Chapter 5, it is evident that the system needed to detect in the wavelength ranges of approximately 450 nm to 950 nm, which would allow capture of several important spectral lines from lightning leaders and return strokes in order to estimate the lightning channel temperature and electron density. Spectral lines for the lightning channel return stroke that have been used for temperature estimation from the literature are 463.0 nm (NII), 500.0 (NII) nm, 568.0 (NII) nm, 594.2 (NII) nm, 648.2 (NII) nm and 661.0 (NII) nm, which are all singly ionized Nitrogen. For lightning leaders, which primarily radiate neutral Oxygen and Nitrogen, wavelengths used for temperature

estimation are: 715 nm (OI), 777.4 nm (OI triplet), 794.7 nm (OI), 844.6 nm (OI triplet), 882.0 nm (OI), and 926.5 nm (OI triplet). To accurately resolve the lightning leader and return stroke, time resolutions of spectra needed to be on the order of tens of microseconds or less. Considering cloud-to-ground (CG) lightning is primarily oriented vertically and appears thin, a slit was not needed to resolve the discrete spectral lines emitted from the CG discharge channel. But, for TLEs such as gigantic jets and sprites, which appear as wide, highly branched structures, a slit is needed to be able to resolve the discrete spectral line emissions. Also, TLEs appear very dim compared with CG lightning, and often they are very far away. Because of this, an image intensifier is needed to amplify the light, which allows the spectra to be recorded. The intensifier is also needed when using the slit, as the slit blocks a large amount of the incoming light to the camera CMOS detector. For spectral resolution, the spectrograph needed to be able to resolve closely spaced spectral lines, and with better spectral resolution the discrete lightning spectral line emissions could be better resolved. This is especially true for streamer spectra, which compose parts of gigantic jets and sprites.

From the needs listed above, the spectroscopy system was designed to include a high-speed camera, a volume phase holographic (VPH) grism, a photocathode image intensifier, and a vertical slit. Lenses with low f numbers to allow as much light as possible to the camera were also selected. The high-speed camera chosen was a Phantom Vision Research V1210, shown in Figure 6.1. The V1210 is a digital high-speed camera and is capable of recording 12 gigapixels per second of data with its complementary metal-oxide semiconductor (CMOS) sensor. The CMOS sensor has a full resolution of 1280 x 800 pixels (horizontal by vertical). The pixel size is 28 microns allowing high light sensitivity. Each pixel has a bit

Figure 6.1: Phantom V1210 high-speed camera with lens attached.

depth of 12 bits, achieving 4,096 levels with high dynamic range. The sensor is also monochrome, with an ISO of 64,000 T, further improving its sensitivity to light. With the electronic shutter, exposures as fast at 1 microsecond are achievable. At full pixel resolution, the camera can record 12,000 frames per second (about 80 microsecond time resolution). However, with reduced pixel resolution, the camera can record over 200,000 frames per second (5 microsecond time resolution). It has embedded memory of 48 GB, which can be partitioned into smaller segments, allowing for many high-speed videos to be recorded and saved to this memory. The camera also has detachable flash memory with 128 GB capacity (shown as the black rectangle on top of the camera in Figure 6.1). The camera is triggered through a computer running Vision Research's Phantom Camera Control (PCC) software. The software allows the camera to be manually triggered through the press of a button or through automatic triggering, which will trigger when an arbitrary group of pixels exceeds an arbitrary intensity threshold. The camera also can accept IRIG

input from a GPS signal, allowing precise time information. The camera accepts
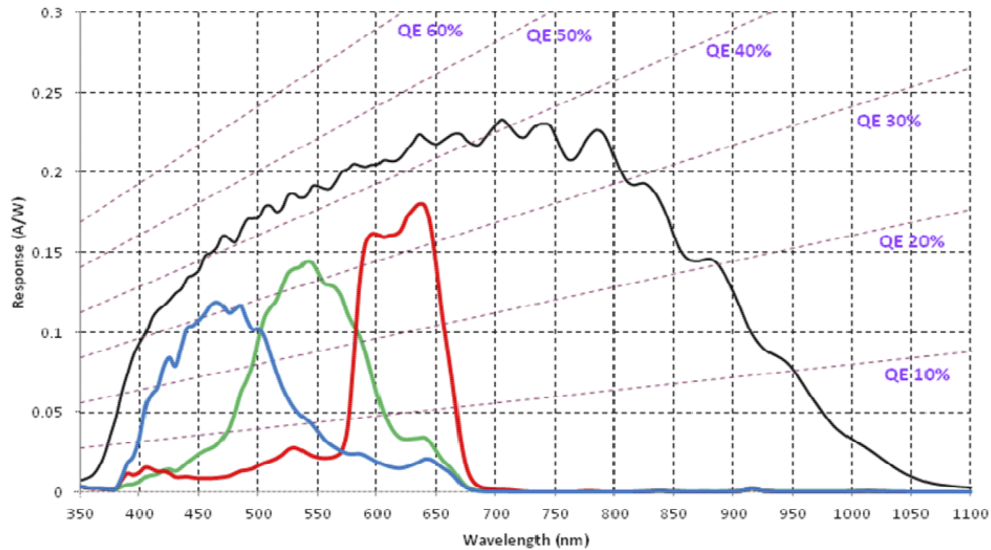
Figure 6.2: Response for the Phantom V1210 high-speed camera.

standard Nikon lenses out of the box, but also has an attachment that allows it to accept Canon lenses. When using the Canon lens attachment and a Canon lens, the lens aperture and focus can be changed remotely through the PCC software. The spectral response of the camera is shown in Figure 6.2 as the thick black line for the monochrome version, which is what was used in the spectroscopy system. The response is strong in the visible wavelengths of 450 nm to 850 nm, with it decreasing outside of this region.

To obtain the lightning spectra, a volume phase holographic (VPH) grism was used, which is a grating between two prisms. The VPH grisms don't have a physical grating, but instead they create diffraction by using a thin film with altered indices of refraction pressed between two plates of glass [*Arns et al.*, 1999]. This allows a higher throughput, allowing dimmer objects to be captured, and better spectral resolution. The VPH grating (thin film) is glued between two prisms, allowing

light to pass straight through the grism to the imaging unit (in this case the high-speed camera), and the whole system can be pointed at the object of interest. The specific grism for the high-speed spectroscopy system used in this study has an approximate spectral range of 500-800 nm for first-order spectra, but this range can be much larger depending on the source geometry related to the grism. The grism was blazed at 630 nm, with 1,257 lines/mm. Combined with the Phantom V1210 high-speed camera, this provides an approximate spectral resolution of 0.5 nm per pixel. The grism is shown in Figure 6.3, placed between a front focusing lens and the high-speed camera. The VPH grating is seen here, diffracting the ambient light in the room. The spectral response of the grism is shown in Figure
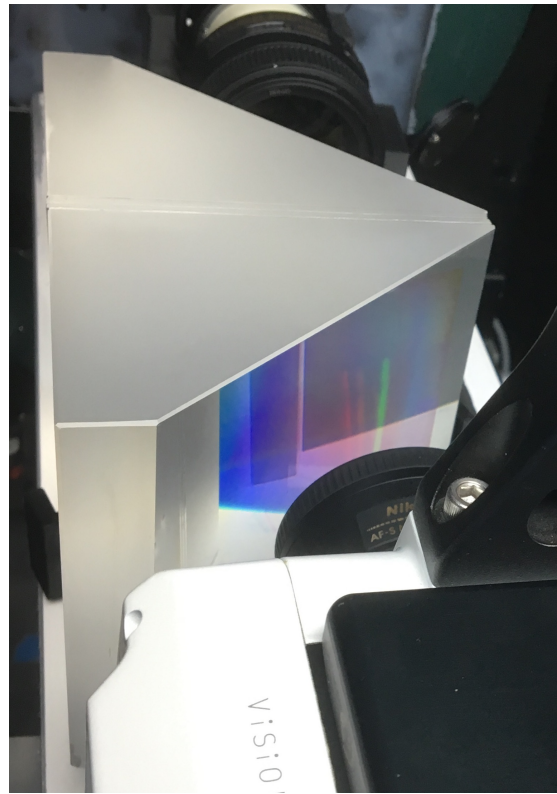
Figure 6.3: VPH grism in between a front lens (top of image) and high-speed camera (bottom of image). Here the two prisms of the grism are seen attached together, with the grating in between producing the colorful diffracted light.

6.4. For first-order spectra, the highest diffraction efficiency is located between the wavelengths of 575 and 750 nm, with it falling off outside of this region.
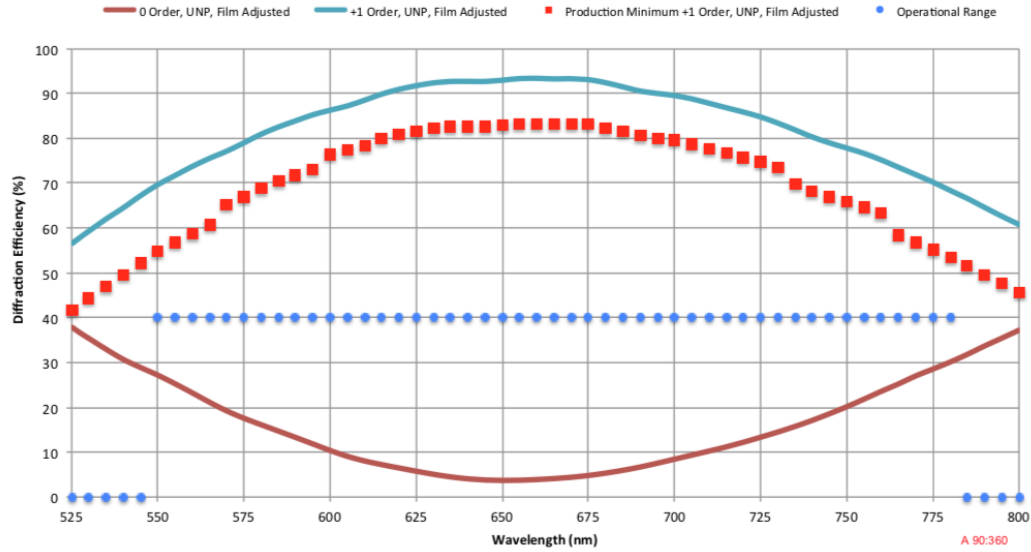
Figure 6.4: Response of the VPH grism.

Figure 6.5: VideoScope VS4-1845-HS-D image intensifier.

The image intensifier used for this study was a Video Scope VS4-1845HS (Figure 6.5). It has a high quantum efficiency that is sensitive to UV with peak blue

response. The intensifier is optimized for ultra-high-speed imaging (greater than 100,000 frames per second), with time resolution of about 3 microseconds. It uses a photocathode to intensify the light, the process of which is shown in Figure 6.6. Photons from a low-light source enter the lens on the left and strike the photocathode, which is the grey colored plate. This causes electrons to be emitted from the photocathode plate, which are accelerated toward the microchannel plate (red plate), which has a higher voltage. When the electrons hit the microchannel plate, each one causes many electrons to be emitted from it. These electrons are now accelerated toward a phosphor screen (green) that has an even higher voltage. When the electrons hit the phosphor screen, photons are emitted that are viewable through the eyepiece. A computer interface was used to control the intensifier, using software that was provided by Video Scope. This software allowed the gain to be controlled, and also the gate timing, which behaves as the frame rate and controls the time resolution of the images.
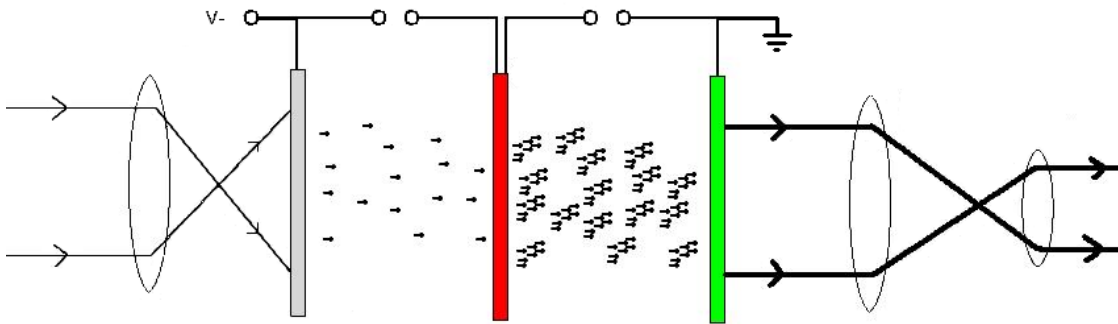
Figure 6.6: Diagram of a photocathode image intensifier. The red object is the microchannel plate and the green object is the phosphor screen.

The spectroscopy system components listed above were configured on the removable tray of the enclosure according to the mission type. For obtaining spectra of CG lightning leaders and return strokes, only the high-speed camera and grism

were used, along with a lens attached to the camera. The lenses used were either a 20 mm, 35 mm or 85 mm Nikon lens, or a 50 mm or 85 mm Canon lens. This setup is shown in Figure 6.7. The grism is placed in front of the camera and is mounted to the tray by a custom 3D printed piece that bolts to the tray. Also securing the grism in place is black industrial duct tape. Figure 6.7b shows a top view of the grism and camera, with a Nikon 35 mm f/1.8 lens attached to the camera. From experimentation, it was found that placing the camera lens as close as possible to the grism gave the best spectral resolution. For the setup to record TLEs such as gigantic jets or sprites, the high-speed camera, intensifier, grism were used, with the option for a slit. These components were all mounted to the tray, similar to in Figure 6.7, only when the intensifier was used, it would mount directly to the front of the high-speed camera, and then the Nikon lens would mount to the front of the intensifier. Then, the grism would be placed in front of the Nikon lens, similar to in Figure 6.7. With this setup, the system can record dimly lit spectra, but the source must be vertically oriented and optically thin, providing sufficient spectral resolution. This is likely ok for recording the bottom portion of gigantic jets, which are similar to a CG lightning leader, but not the tops of gigantic jets. The tops of gigantic jets branch and very wide, similar to sprites. To get sufficient spectral resolution when obtaining their spectra, a slit is needed in addition to the components listed above. The slits used were made of glass, oriented vertically, and had widths of 50 or 100 microns. These slit widths provide spectral resolution similar to the resolution for CG discharges, about 0.5 nm per pixel. A setup showing the slit incorporated in the spectroscopy system is shown in Figure 6.9. This figure does not have the intensifier shown, but it would be placed in between the high-speed camera and the grism. When the slit is used (shown in Figure 6.8), it

Figure 6.7: a) Side view of the high-speed camera and VPH grism mounted on the enclosure tray. b) Top view of the front lens of the high-speed camera and the VPH grism.

is placed between a front collecting lens with a low focal length for a wide field of view and between a collimating lens, in this case with a focal length of 85 mm. It is held in place between these two lenses by a custom made, 3D printed component, shown in Figure 6.9a.

Finally, to record the scene view and the background star map, a low-light Watec 902B camera was installed on the top of the high-speed spectroscopy enclosure, pointing at the same direction as the high-speed system. The Watec 902B

Figure 6.8: The optical slit used for the high-speed spectrograph.
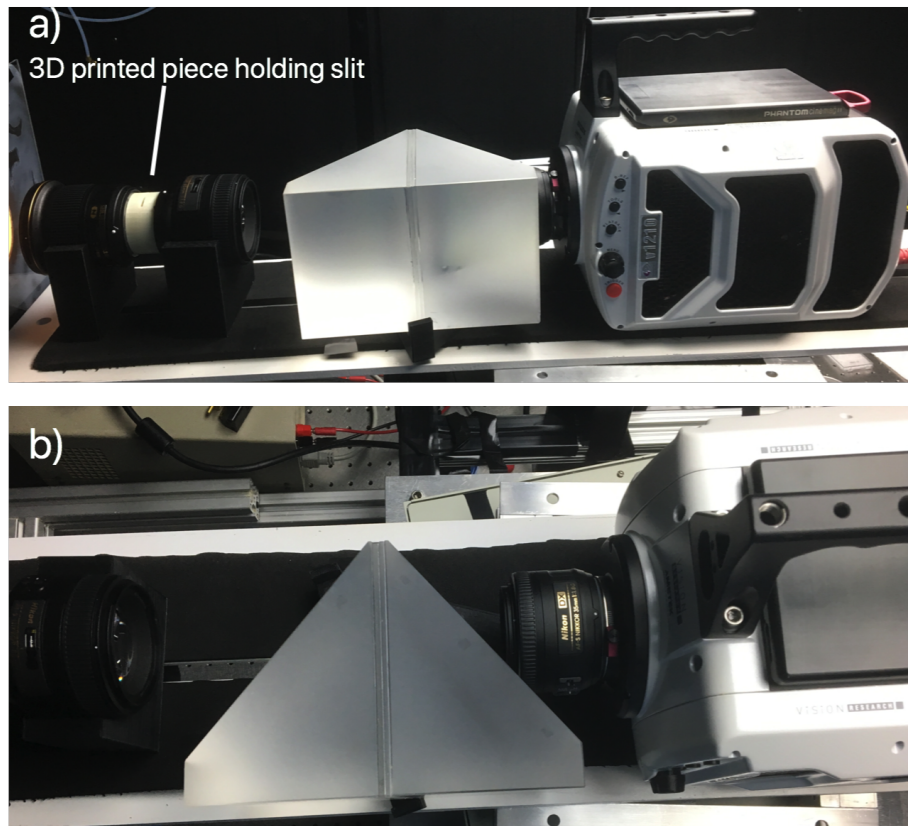
Figure 6.9: a) Side view and b) top view of the high-speed spectrograph with slit installed.

records at 30 frames per second and has a charge coupled device (CCD) sensor with dimensions 768×494 pixels. The pixel size is 8.4 microns horizontally by 9.8 microns vertically. The Watec is also synced to a GPS satellite for precise timing

information, allowing comparison to the high-speed video. To trigger and record videos, the software UFO capture is ran with the Watec input going into a PC. UFO capture has many customizable settings, and allows the Watec videos to be saved to the computer hard drive.

6.2 Enclosure

To allow for continuous observation in thunderstorm conditions, a high-quality, sturdy, weatherproof enclosure was needed to house the spectroscopy system. If the system was put inside an enclosure on a rooftop, with the ability to rotate in azimuth and elevation, the system would have no limits to its field of view and it could also be deployed to different locations. It was important that the enclosure be able to collect data when active thunderstorms were in the area, because the system needed to be as close as possible to the lightning flash. This would enable the system to capture dimly lit lightning leaders, which are drastically dimmer than lightning return strokes, making them difficult to capture. Also, the spectral lines available to estimate the leader channel temperature, which are primarily neutral Oxygen and Nitrogen, radiate dimly when compared to the singly ionized lines. This is especially true for the neutral Oxygen line at 715 nm, which is often needed for temperature estimation.

To understand the needs of the enclosure that would reliably house the system, I first assembled the spectroscopy system in the lab. This allowed me to record the physical dimensions of the system and assess the needed capabilities while the system was fully operational. The key requirements for the enclosure were:

1. The enclosure needed to house all the spectroscopy system components,

which included: the Vision Research Phantom V1210 high-speed camera with flash memory attached (without top handle) and with a lens attached, the Volume Phase Holographic grism, the Video Scope VS4-1845HS intensifier, and the option for a lens/slit assembly.

2. The enclosure needed to secure the spectroscopy system components when the system was operational, not allowing the parts to move relative to one another.

3. The enclosure needed air circulation to prevent the system from overheating.

4. The enclosure needed to have measures to prevent fog and condensation forming on the front viewing piece.

5. The enclosure needed to be waterproof.

6. The enclosure needed to have a way to efficiently thread cables from the spectroscopy instrumentation to outside computers and power sources.

7. The enclosure needed to allow easy access to the inside components for troubleshooting and installing/removing the spectroscopy system instruments.

This information was then passed to Geospace Physics Lab undergraduate researcher Matthew Austin, who has a background in aerospace and mechanical engineering. From the requirements listed above, Matthew first designed the enclosure in Solid Works, which is computer-aided design and computer-aided engineering software. After Matthew and I agreed upon an enclosure design, we next chose the material that would serve as the body and frame. We chose 6061 T6 Aluminium (Al), which is a heat-treated aerospace grade metal. The 6061 T6 Al is

very strong, has corrosion resistance, and is easily machinable. It is also about one-third the weight of stainless steel, making it perfect for our needs. We chose to make the body one-quarter inch thick, which provided adequate strength but still kept the enclosure relatively light. After the metal was obtained, it was machined and welded according to our design specifications. Figure 6.10 shows the
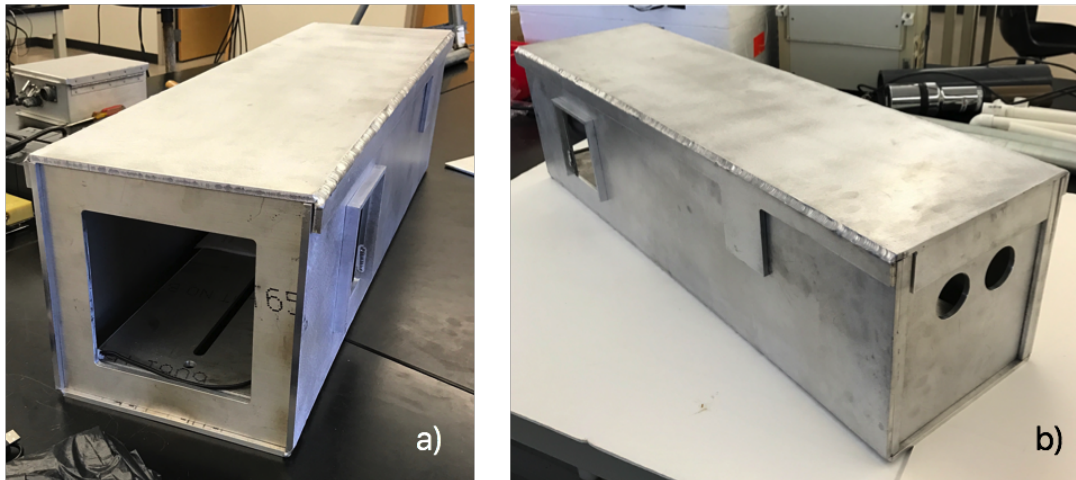
Figure 6.10: Metal frame of the high-speed spectrograph enclosure showing the (a) front and (b) rear.

enclosure after welding the metal frame together. Present in both of these panels is the detachable lid, which can be completely removed to allow easy access to the components of the spectroscopy system. The downward protrusion from the lid on the side in Figure 6.10b is for a pad-lock, which will be mounted here and on the opposite side to lock the lid in place. This allows the lid to be securely fastened during severe storms with gusty winds and also to prevent trespassers from stealing/altering components of the system. Also present in these figures are square holes for a fan. A similar hole is also on the other side, but located near the rear of the enclosure. The fans are located on both sides of the enclosure, one at the

front and one at the rear, to 'snake' the air through the enclosure. The front fan pulls air into the enclosure, and the rear fan blows it out. This allows maximum air flow through the enclosure, cooling the spectroscopy system and reducing fog on the viewing window.
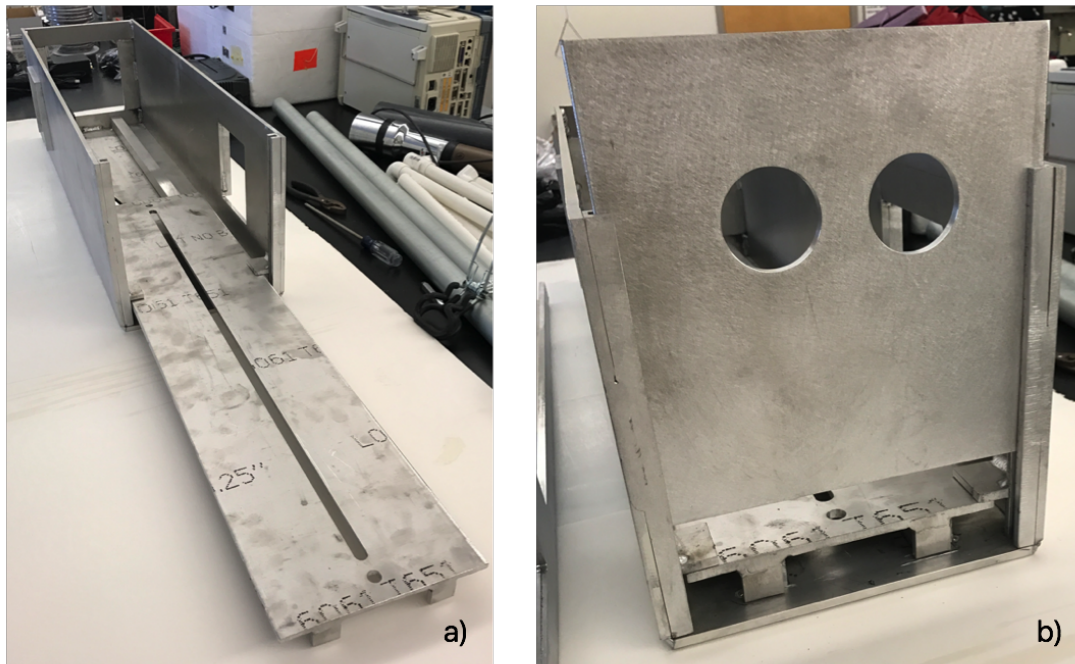
Figure 6.11: a) Enclosure with back and top piece removed and tray pulled out. b) rear piece of the enclosure.

Figure 6.11a shows shows the enclosure with the lid off and the tray pulled out. The final design of the enclosure featured a removable tray, which allows the system to be completely removed for troubleshooting and to bring inside the lab for testing. The tray also has a channel cut into it to allow the spectroscopy system components to be easily mounted at arbitrary positions along the tray, which is done by bolting the components to the tray. The camera already had holes in the bottom of it, allowing easy attachment to the tray, but to securely bolt the other

components of the system custom parts were 3D printed. The back piece of the enclosure was also removable (Figure 6.11b), and had to holes cut in it to allow cables to be passed from outside computers and power sources to the spectroscopy system inside. We had the back piece slide upwards to be removed, which, when in place, locked the removable tray into position. Thus, we did not need to bolt the back piece on, as the grooves at the rear held the back piece securely in place. To keep the system water proof, plastic ducts were adhered to the outside of the
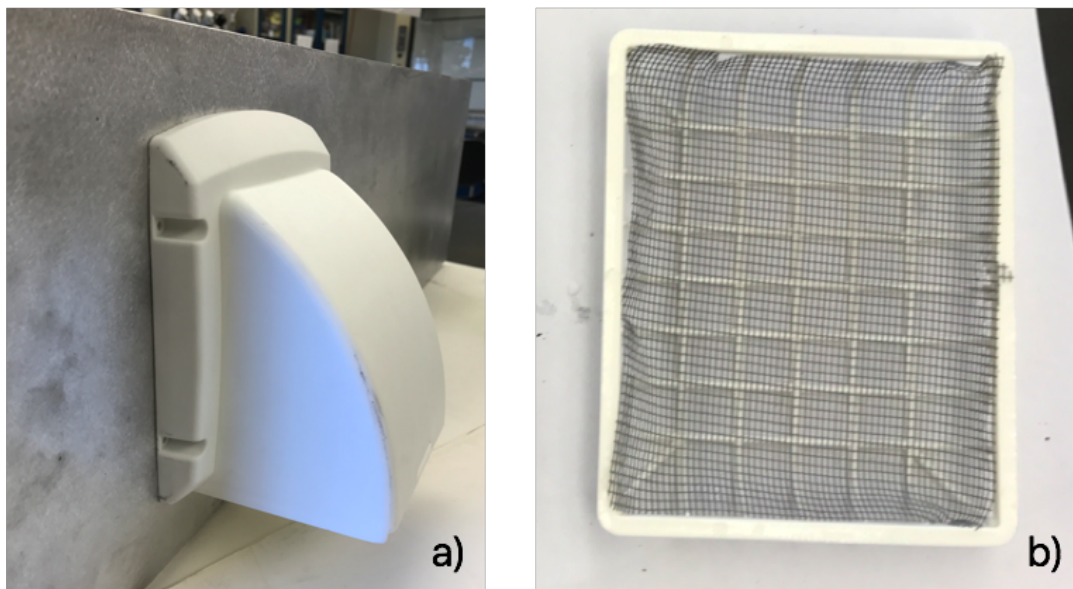
Figure 6.12: a) Plastic duct covering fan hole. b) Fine mesh screen adhered to bottom of removable tray for the plastic fan duct.

enclosure over the holes for the fans (Figure 6.12a). The bottom of the ducts were open, but had a plastic frame that would slide in and out. Fine mesh was adhered to these plastic frames (Figure 6.12b), as this would prevent small debris and bugs from entering through the plastic fan ducts.

After the metal frame was assembled, the inside of the enclosure was painted

matte black to minimize internal light reflections being detected by the system. The outside of the enclosure was painted white, to reflect sunlight and help keep it cool. Next, the fans were installed, along with their control circuit, which was installed at the rear of the enclosure in a plastic case. The control circuit came with the fans and it had wires running to each fan, and it was powered with standard 120 V AC. Finally, the front viewing piece was installed, which was siliconed to

Figure 6.13: Front view of the spectrograph.

the front of the enclosure (Figure 6.13). We chose to use clear acrylic for the front viewing piece, as it has very high transmission from the visible wavelengths we are interested in. It is also shatter proof, which ensures that if debris strikes it from high winds, broken shards will not damage the spectroscopy equipment inside. Black foam was also adhered on the front of the acrylic, except for the circular hole where the spectroscopy system would view. This reduced external light noise from entering the system.

Figure 6.14 shows the final enclosure assembled and mounted to the control motor on the roof of the Olin Physical Science Building at Florida Tech. The
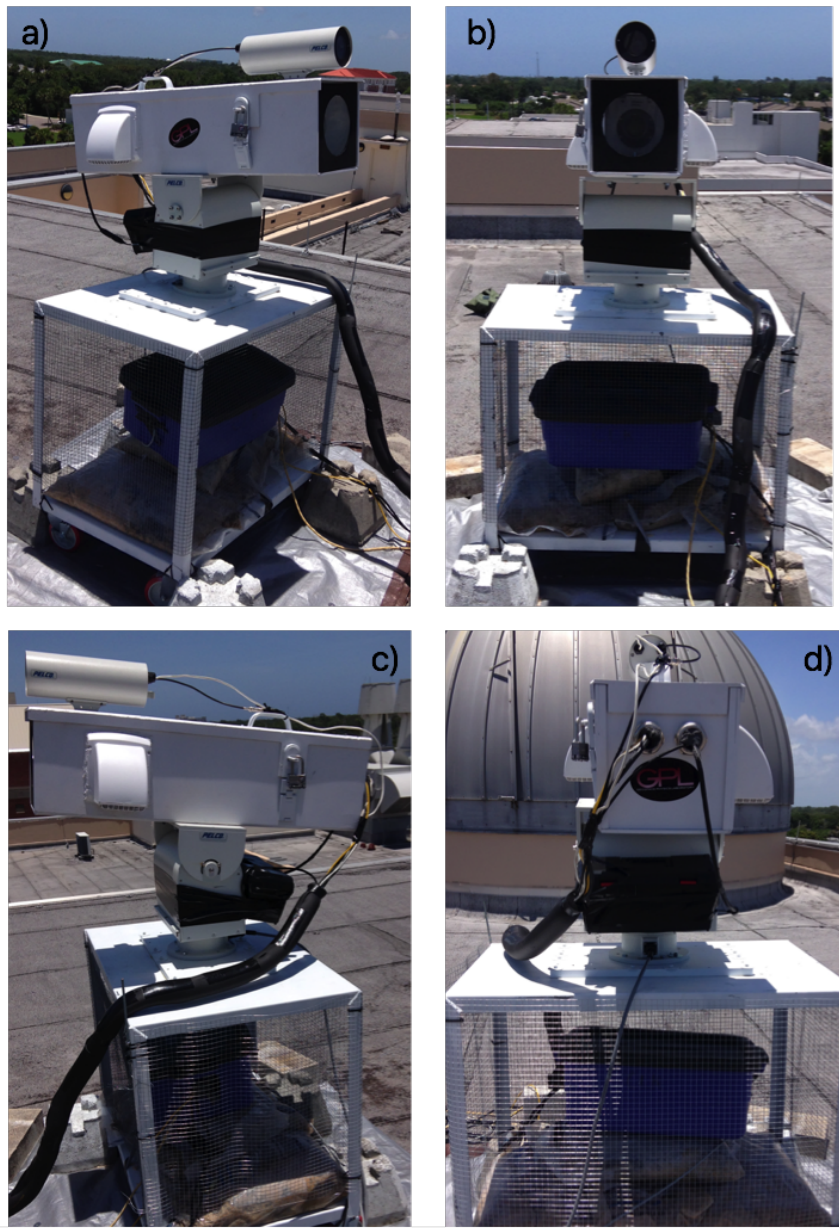
Figure 6.14: The finished high-speed spectrograph system, with a) right side view b) front view c) left side view and d) rear view. The Watec low-light camera enclosure is seen mounted on top. The high-speed spectrograph enclosure is mounted to a Pelco motor, which is then mounted to a metal cart.

padlock is seen securing the lid, with cables coming from the back, which were ran down into the Geospace Physics Lab. The low-light Watec camera enclosure is mounted to the top of the spectroscopy system enclosure, facing the same direction. This enables the Watec camera to obtain a scene view, and also to record the background star map. The spectroscopy system is mounted to the heavy duty motor, which is then mounted to a square metal base with locking wheels to allow movement if desired. To secure the whole setup, heavy sandbags and cement blocks were place on and around the square metal base. The tupperware tub inside the square metal base housed a power-strip, which was used to power the fans inside the spectroscopy enclosure and also the high-speed camera. The power adapter for the high-speed camera was put in the black box seen taped to the motor (Figure 6.14d), which was then sealed and made waterproof. Having the adapter there allowed the system to spin freely in azimuth. The cables from the rear of the enclosure were bound together with foam casing, which helped the cables to not tangle when the motor would spin in azimuth or elevation.

6.3   Control System

As shown above in Figure 6.14, the high-speed spectroscopy system enclosure is attached to a motor, which is used to control the pointing direction of the system, and can rotate in azimuth and elevation. The motor is a Pelco PT1250P and can support weights up to 100 lbs, while maintaining reliable rotation rates, and is powered by 120 V AC (Figure 6.15). We wanted both the capability to control the motor from both inside GPL and remotely, and this resulted in several modifications to Pelco's standard control system circuit. The modified circuit is shown in

Figure 6.15: Heavy-duty Pelco motor for positioning the high-speed spectrograph.

Figure 6.16. First, we purchased a small motor control box with four buttons on it (up, down, left, right). These buttons, when properly wired, allowed us to pan and tilt the motor within GPL, which is useful when monitoring thunderstorms from the Watec camera display, which was also in GPL. This box was intended to be used with a smaller motor that is similar to our heavy-duty Pelco PT1250P, but with an output of 24 V DC instead of 120 V AC from our Pelco motor. Considering the large Pelco PT1250P operated on 120 V AC, we needed a relay to modify the 24 V DC output from the motor control box to 120 V AC. This was done by using a relay box that was sold with the Pelco PT1250P. With the relay box for the large motor installed along with the wires connecting the motor, relay box, and motor control box (with the motor control box plugged into 120 V AC outlet), the motor was controlled from the four buttons on the motor control box successfully (black boxes in Figure 6.16).
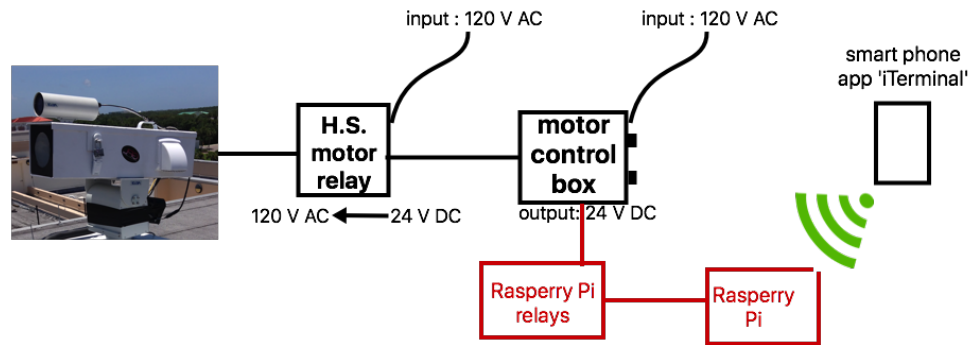
Figure 6.16: Block diagram of the motor control system.

To allow remote control of the motor system, a Rasperry Pi was used in conjunction with the motor control box (red boxes in Figure 6.16). Using the General Purpose Input/Output (GPIO) output bins from the Rasperry Pi, which can be controlled from code on the Rasperry Pi (see Appendix), in conjunction with another set of relays, the Rasperry Pi was able to control the motor control box - in place of someone pressing the physical buttons on the motor control box. Another set of relays was needed to do this, as the output from the GPIO Raspberry Pi pins is 3-6 V DC, and the motor control box operates at 24 V DC. Figure 6.17 shows the actual hardware described in Figure 6.16.

For remote control, first the user runs the Python code on the Rasperry Pi. This code can be executed directly by connecting a keyboard and mouse via USB to the Raspberry Pi, or by remotely connecting to the Raspberry Pi via the internet (the Raspberry Pi has WiFi and also an ethernet port). In the code, the rotation rate of the motor in azimuth and elevation was accounted for, and when the user wants to turn the motor to a desired azimuth and elevation, the code computes the duration it will turn on each output GPIO pin on the Raspberry Pi. The
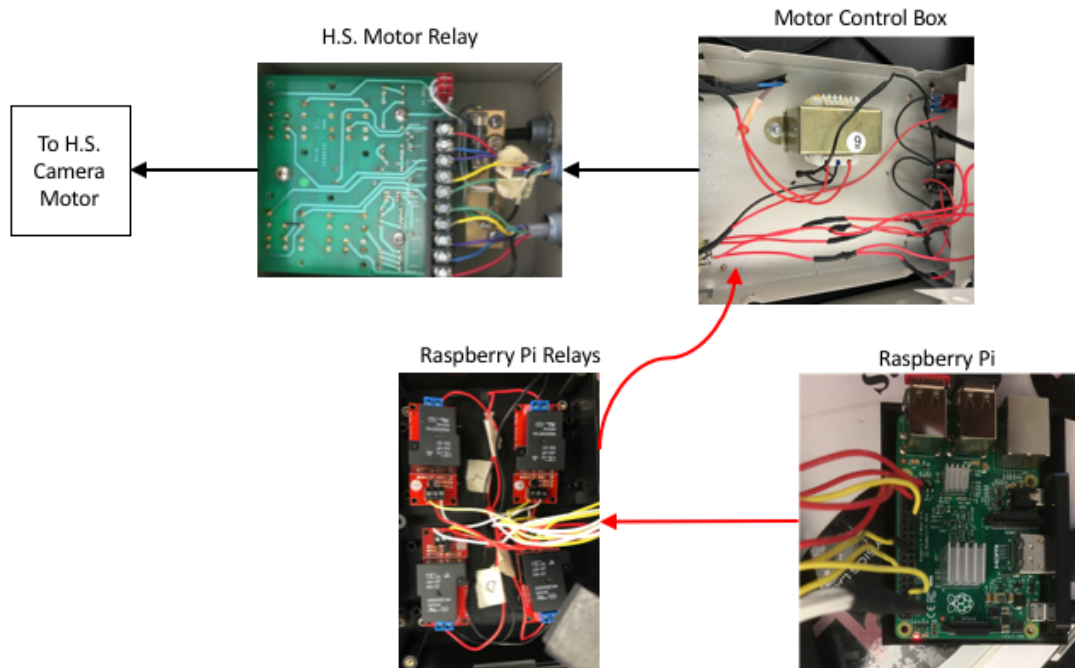
Figure 6.17: Block diagram showing the wiring of the motor control system.

3-6 V DC outputs from the GPIO pins on the Raspberry Pi are connected to the Raspberry Pi relays - one relay for each direction (up, down, left, right). These relays step the voltage to 24 V DC. The output from these relays is spliced directly into the wires in the motor control box that run from the buttons on the front of the box to the output pins on the rear of the box. Next, the 24 V DC output pins from the motor control box rear are connected to the H.S. motor relay box, which takes in the 24 V DC signals and changes it to 120 V AC. Finally, the 120 V AC signals (one for up, down, left, right) are fed into the H.S. camera motor. When the motor receives a voltage signal, it will turn in that direction at a constant rate. Thus, the motor control system was able to be reliable controlled from inside the GPL, or remotely via an internet connection to the Raspberry Pi. The remote connection to the Raspberry Pi can be done via a desktop computer or via an SSH

client smartphone app such as Terminus (https://termius.com/). In the Python code controlling the motor, a log file was created that was appended to every time the user executed the code with the azimuth, elevation, and time that the code was executed.

Chapter 7

High-Speed Spectroscopy Results

In this chapter, the results from an observational campaign from the summer of 2017 to the fall of 2019 are presented using the high-speed spectrograph discussed in Chapter 6. The campaign took place in Melbourne, FL and the spectrograph was located on the roof of the Florida Institute of Technology Olin Physical Science building. The lightning spectra presented here were recorded by the high-speed spectrograph setup used for cloud-to-ground lightning, which consisted of the Phantom V1210 high-speed camera and the VPH grism. These components were bolted to the tray as shown in Figure 6.7 and the tray was inserted into the spectrograph enclosure. To make observations, the front of the spectrograph was positioned to face a thunderstorm with frequent lightning, and lightning spectra were saved when the Phantom V1210 high-speed camera was triggered. The triggering was done by using the Phantom Camera Control (PCC) software, which uses arbitrary pixel area and intensity thresholds to trigger the system. Due to the system being able to be operated remotely, it was frequently operated from off-campus, which greatly expanded the detection capability over previous systems.

The spectra presented here consists of intracloud, stepped, and dart leaders. The spectral analysis focused on calculating the lightning leader channel temperature as described in Chapter 5. Considering the temperature analysis consisted of dimly lit lightning leaders as opposed to bright return strokes, the spectral lines used for the temperature estimates were 715.0 nm and 777.4 nm, which are both neutral Oxygen (OI). They have a difference in excitation energy of about 4 eV, which allows them to provide good estimates of the channel temperature. For reference, *Uman* [1966] and *Orville* [1968b] have found that to obtain reliable temperature estimates, the difference in excitation energy should at least be 1 eV. For the spectra reported here, the uncertainties were relatively small (7 to 10%) due to an improvement of the signal-to-noise ratio (SNR) by coherently integrating the spectra (discussed in the next section).

This observational campaign produced six flashes with intracloud leader spectra, nine stepped leader spectra (from nine flashes), and eighteen dart leader spectra (from seven flashes). The spectra were recorded with a spectral resolution of 0.3 to 0.5 nm/pixel, and with time resolutions of 62 and 200 μs (IC leaders); 16 and 32 μs (stepped leaders); and 16, 32, and 62 μs (dart leaders). For some of the stepped and dart leaders, spectra of large sections of the visible channel were obtained. By using digital signal processing techniques, temperature estimates were made for these large sections of the channel (discussed in the next section). Also, many of the stepped and dart leaders were observed for many subsequent frames (images), allowing the time evolution of the channel temperature to be analyzed.

7.1 Analysis Methods

This section describes the digital signal processing techniques to estimate the temperature for the lightning leader spectra. Considering the CG setup of the spectrograph was slitless, to estimate the temperature for the whole lightning channel, digital signal processing techniques were used to correct for the system response, align the spectra, and improve the SNR of the spectra.

7.1.1 Correcting for System Response

The spectroscopy system has a response associated with it that is not flat, meaning it detects some wavelengths better than others. Figure 7.1 shows a spectral profile for a typical lightning spectra, showing intensity as a function of wavelength. The discrete spectral lines are due to the lightning channel and are seen superimposed on a large, continuous background emission feature that peaks around wavelength 750 nm. This parabolic shaped continuous background is caused by the spectroscopy system preferentially detecting the wavelengths near the center of the horizontal axis in Figure 7.1. In order to perform accurate intensity measurements of spectral lines, the system response should known and accounted for.
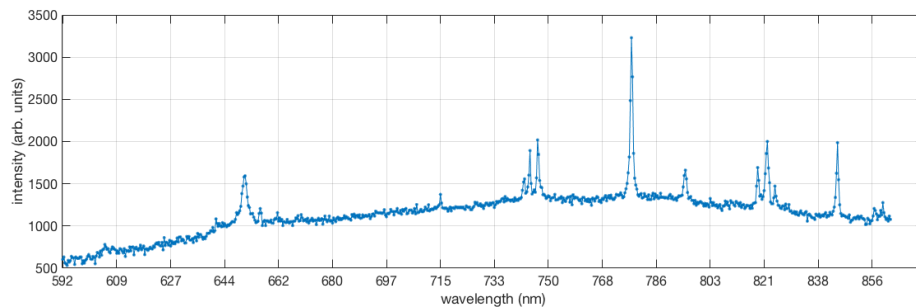
Figure 7.1: Spectral profile of a raw lightning spectra without correction for the system response.

To correct for the response, the discrete spectral emissions due to lightning were removed by using a hampel median filter. The filter computes the median of a window composed of the sample ± 3 samples (length = 7). If the sample is outside the bounds of the median ± c×Median Absolute Deviation (MAD, c = scaling constant), then it is replaced by the median. This filter is used to remove outliers, which in this context the spectral lines can be viewed as outliers superimposed onto the background emission feature. After the hampel outlier filter, the data is smoothed using a moving average filter with a window length of 7. The result of these filtering procedures is the orange line in Figure 7.2, which represents the background emission spectrum multiplied with the spectroscopy system response. Finally, to correct for the system response, the spectrum of the
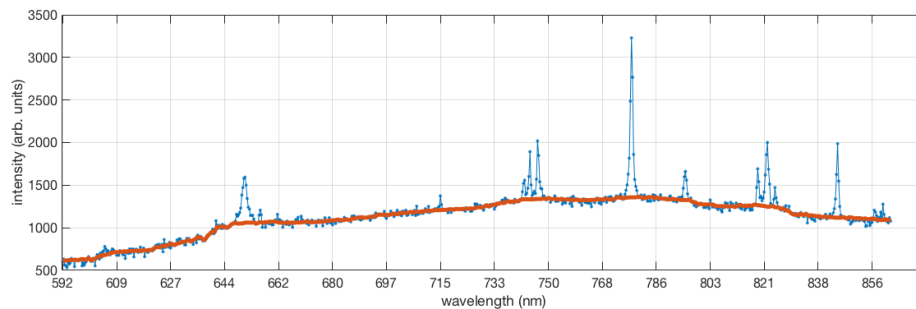
Figure 7.2: Spectral of Figure 7.1 with the background emission spectra (orange line) overlaid.

background emission is subtracted from the lightning emission spectrum, and then the lightning emission spectrum is divided by the background emission spectrum. This is shown in Figure 7.3. Now the spectral lines have been adjusted for the system response and the relative spectral line intensities can be estimated. It should be noted that this method assumes the background emission has a flat spectral shape (white).
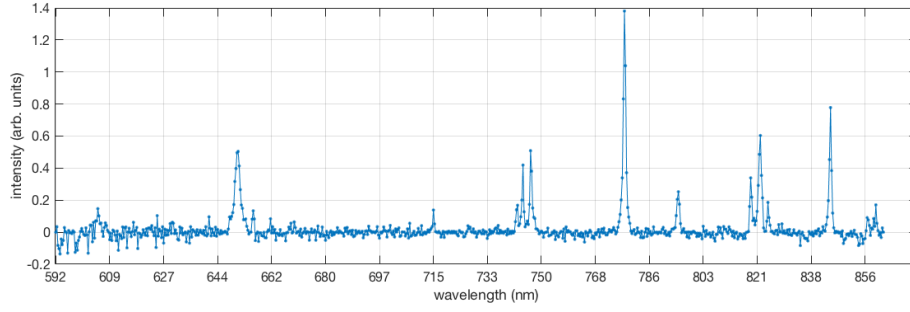
Figure 7.3: Spectral profile corrected for the system response.

7.1.2 Estimating Background Noise and Temperature Uncertainty

In order to calculate the uncertainty of a temperature estimate, the variation of the background noise needs to be quantified. As shown in section 5.1 and equation 5.12, the uncertainty in the temperature estimate is

$$\delta T = \left(\frac{E_m - E_n}{k ln^2 (RG\frac{A_{mp}}{A_{nr}})} \right) \sqrt{\left[\left(\frac{\delta R}{R} \right)^2 + \left(\frac{\delta A_{mp}}{A_{mp}} \right)^2 + \left(\frac{\delta A_{nr}}{A_{nr}} \right)^2 \right]}$$

where E_n (E_m) is the excitation energy on the nth (mth) level, k is the Boltzmann constant, $G = \frac{\nu_{mp} g_m}{\nu_{nr} g_n}$ where g_n (g_m) is the statistical weight of the nth (mth) level and ν_{nr} (ν_{mp}) is the frequency of the emitted photon, $R = \frac{I_{nr}}{I_{mp}}$ (the ratio of line intensities, and A_{nr} (A_{mp}) is the Einstein coefficients for transition probability. From this equation, the everything outside of the radical is a constant, meaning that the uncertainty in temperature is only a function of the error in the intensity ratios (δR) and the Einstein coefficients (δA). Considering most Einstein coefficients are known to a few percent, the dominating factor contributing to the temperature uncertainty is the the error in the intensity ratios. This error results from the variation of the background noise of the spectra. Thus, if a weakly emitting spectral

104

line is barely above the variation of the background noise, then the uncertainty in the intensity ratio will be large.
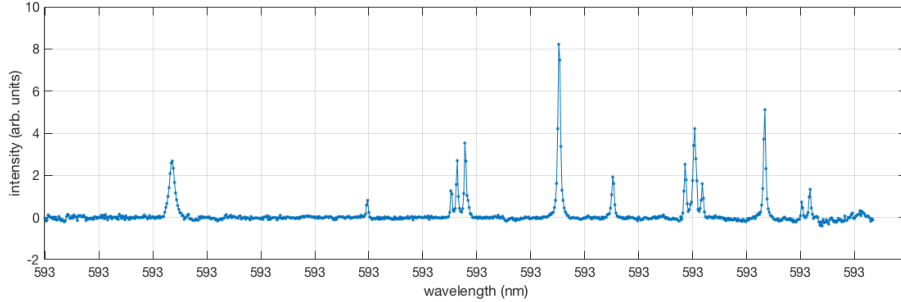
Figure 7.4: Spectral profile from Figure 7.3 after coherent integration of five rows.

For the temperature calculations presented here, the standard deviation was used as an estimator of the variation of the background noise for a spectral profile with the discrete lightning emission lines removed. This procedure was done for each row of the spectral image (each row is a spectral profile), resulting in each row having a single value associated with the variation of the background noise. These standard deviations were used as the δR term in the above equation. Considering the temperature estimates used the weakly emitting 715.0 nm emission line, which is barely above the background noise in Figure 7.3, additional techniques were used to improve the SNR and decrease the temperature uncertainties. Most of the spectral images contained spectral information for tens to hundreds of rows (spectral profiles), and these profiles were aligned (see next section) coherently integrated (averaged) over an arbitrary number of rows to improve the SNR. Coherent integration of N rows results in a $\sqrt{N}$ improvement in the SNR [*Cochocki and Unbehauen*, 1993; *Mitra and Kaiser*, 1993; *Meyr et al.*, 1997], where N is the number of rows integrated. For the spectra presented in this dissertation, N ranged from 5 to 20, resulting in SNR improvements of 2 to 4.5 over that back-

ground noise. An example of a spectral profile after coherent integration is shown in Figure 7.4.

7.1.3 Aligning the Spectra

In order to analyze the spectra over an image with many rows (many spectral profiles), the analysis is accomplished by aligning the spectral lines from the lightning emissions. This is needed as the spectroscopy system does not use a slit, so as the lightning channel moves erratically in front of the camera, the location of the spectral lines also move across the CMOS sensor, meaning each row will have the spectrum shifted in relation to the source location. An example of a lightning flash that is not aligned is shown in Figure 7.5. The alignment is achieved by using a
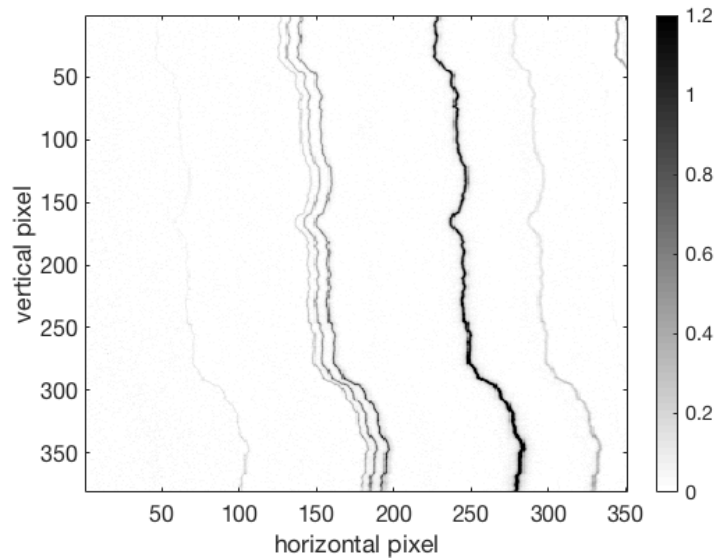
Figure 7.5: Spectral image of a raw, unaligned lightning flash. The intensity scale is in arbitrary units.

matched filter, which correlates each row with a 'template' of the spectrum. The template used was the first row of the image that had strong spectral features.
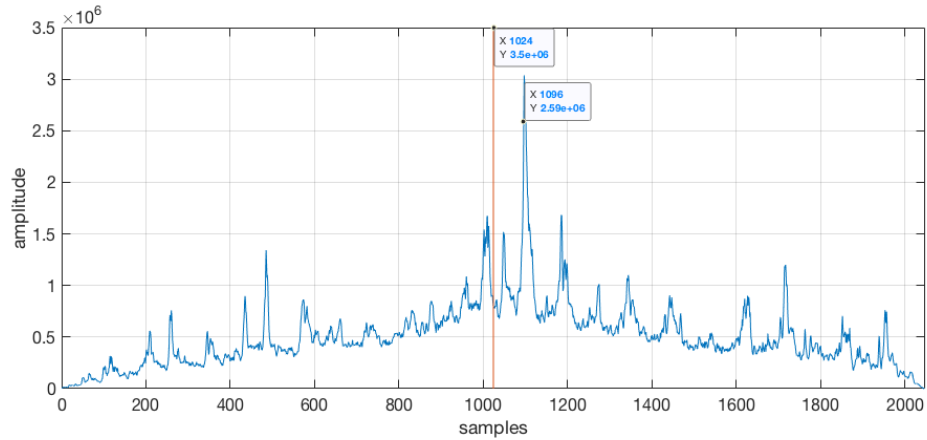
Figure 7.6: Matched filter output shown in blue. The vertical orange line represents where the peak of the matched filter output should be to be aligned with the template of the matched filter.

To align the spectra, first the difference between adjacent pixels for each row of the image is calculated and the absolute value is taken. Next, the matched filtering is performed. This involves convolving a flipped version of the ith difference row with the difference of the template (the first row). The output of this is shown in Figure 7.6. Considering the length of each row for this example is 1024 samples, the x-axis in Figure 7.6 goes from 0 to 2048 samples ($2 \times$ the row length). If the spectral lines from the ith row were aligned with the template, then the peak from the matched filter output would be at the center of the x-axis in Figure 7.6, which is indicated by the vertical orange line at x-axis $= 1024$. But, the example presented in Figure 7.6 shows the peak at x-axis $= 1096$, meaning this row is shifted 72 pixels (1096-1024). To align this row with the template, the row is shifted 72 pixels to align it with the template. This results in the spectral lines of the ith row being aligned with the first row of the image. An aligned spectral image is shown in Figure 7.7. This alignment of the spectral lines over multiple rows allows the spectra to be coherently integrated as described above in section 7.3.

107
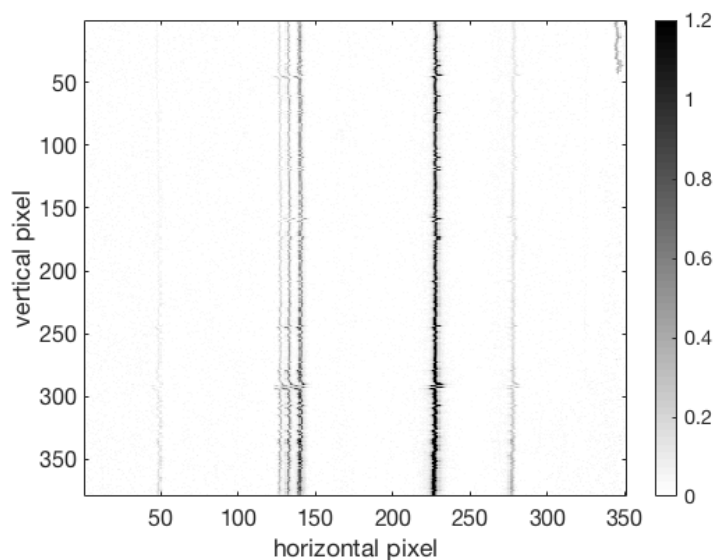
Figure 7.7: Spectral image of an aligned lightning flash. The intensity scale is in arbitrary units.

7.2 Intracloud Leaders

Due to the limitations of past observations (hardware, lack of automation) there have not been any reported spectra of IC lightning leaders in the literature. From the observational campaign described in this dissertation, six different IC flashes were recorded, all producing several frames containing lightning leader spectra. These flashes were identified as IC because the events had no ground termination points and the visible lightning leaders were all well above the surface, with some protruding through the side of the thundercloud. An image showing an example of the lightning, cloud, and ground is shown in Figure 7.8. Many of the flashes resembled 'spider' lightning from stratiform charge regions, and are thus likely negative leaders in a stratiform area of positive charge. However, their polarity has not been confirmed due to lack of GPS synchronized time. The flashes all produced bright spectra at discrete intervals, filled between with dark sky. These bright

108
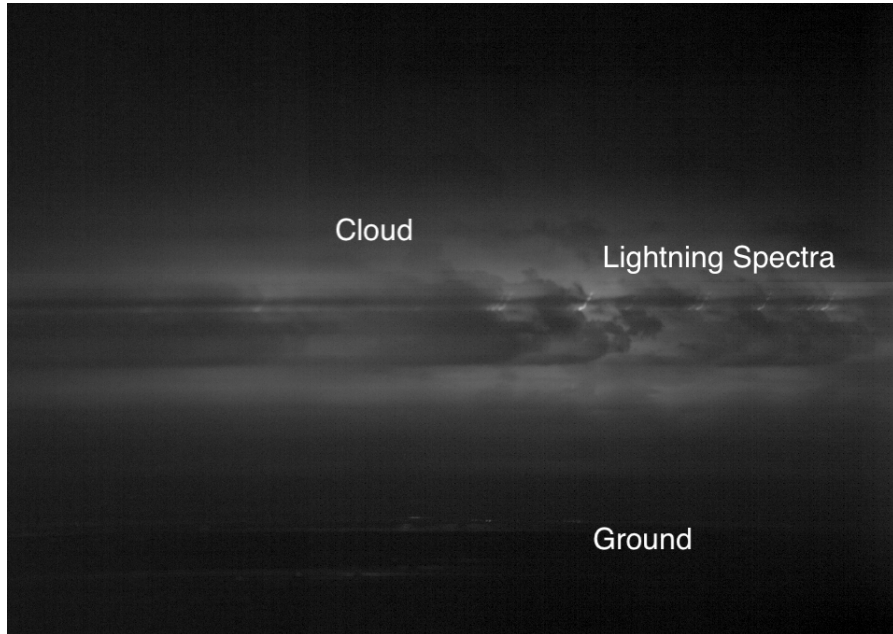
Figure 7.8: High-speed spectral image of an intracloud flash.

intervals resemble K-changes or recoil events [*Winn et al.*, 2011] from negative

leaders in a stratiform charge region. Considering IC leaders propagate primarily in

the horizontal direction, spectra were only analyzed when the leaders bent upward

(vertically), resulting in clear, reliable spectral lines of the leader. Also, since the

channel segments were small, the captured spectra were aligned and coherently

integrated as described in section 7.1, only integrating over the entire channel

segment. An example of an IC spectra is shown in Figure 7.9. The image in

Figure 7.9a was recorded with a 62 μs exposure. A spectral profile from the red

line in Figure 7.9 is shown in Figure 7.9b. The dominant features are neutral

spectral lines, which are neutral Oxygen (OI) and neutral Nitrogen (NI), as well as

H-alpha at 656.3 nm. As mentioned above, the temperature was calculated using

the lines 715.0 and 777.4 nm, but notice how weak the 715.0 nm line is in Figure

7.9. This was after coherent integration of the short channel segment (several rows

of pixels), increasing the signal-to-noise ratio. Past equipment was likely unable to observe this line due to less sensitive equipment and without the ability to perform digital signal processing [*Orville and Salanave*, 1970].
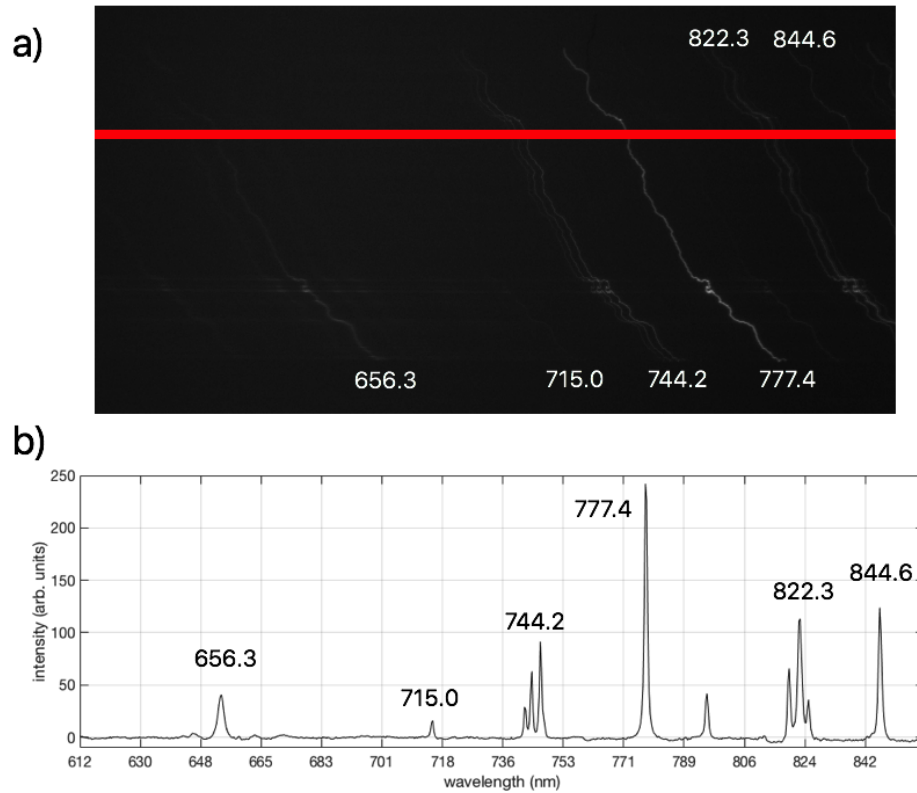
Figure 7.9: a) High-speed spectral image of an IC leader. The red bar represents the location where the spectra in b) was taken. b) Spectra of the IC leader. The labels are wavelengths in nm.

The evolution of the leader channel temperature for two flashes is shown in Figure 7.10. These two flashes had the largest number of frames with clear lightning spectra, and it should be noted that the samples in Figure 7.10 are not consecutive. As mentioned above, the spectra were emitted at discrete intervals with dark sky in between. In the top panel of Figure 7.10, the temperature ranges from about 12,000 K to over 18,000 K. The bottom panel shows much hotter temperatures,

with values ranging from 19,000 K to 25,000 K. This flash was the hottest IC flash observed during the observational campaign, with temperatures close to those of CG return strokes [*Prueitt*, 1963; *Orville*, 1968a]. Figure 7.11 shows the mean
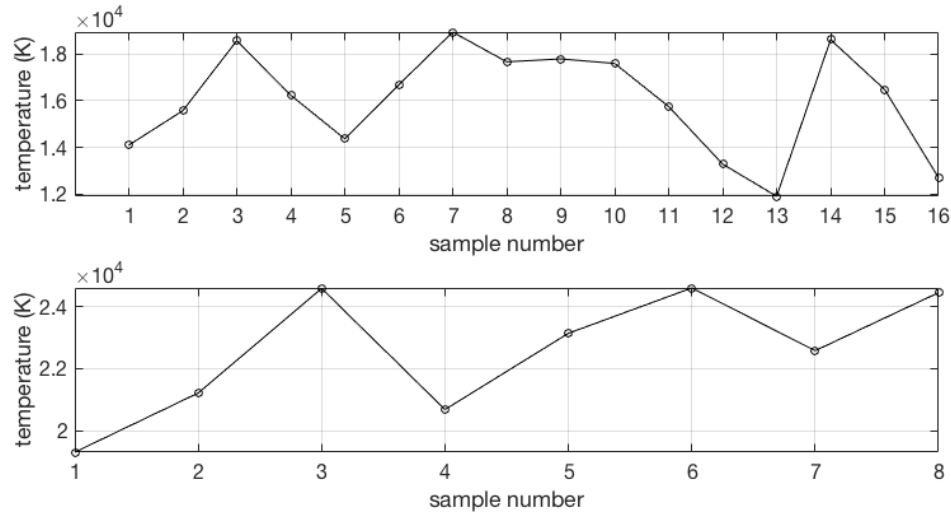
Figure 7.10: Temperature as a function of sample (spectral image number) for two IC flashes. Note: the samples are not consecutive in time.

temperature for each of the flashes producing IC leaders recorded by the high-speed spectrograph. The mean temperatures ranged from approximately 15,000 K to 24,000 K. From all six flashes, the mean temperature was 18,800 K with a standard deviation of 2,200 K.

7.3 Stepped Leaders

Similar to the observational constraints listed above for IC leaders, stepped leaders have been difficult to capture in the past. As mentioned in Chapter 5, only two studies have reported on the optical spectrum of a stepped leader. It is difficult to get quantitative temperature estimates as stepped leaders strongly radiate neutral
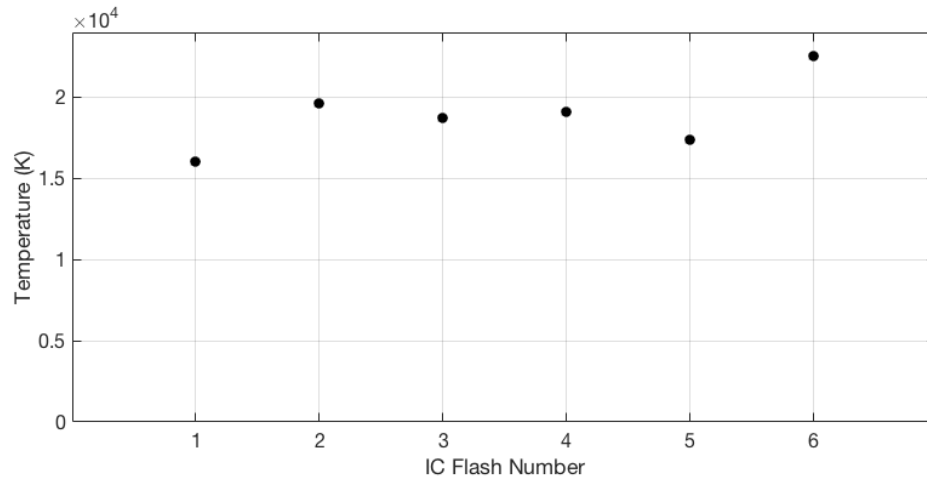
Figure 7.11: Mean temperatures for all six IC flashes from the observational campaign.

emission lines, similar as the IC leader. Making matters worse, stepped leaders often have several branches from the main leader channel, and often have more than one leader channel emerging from the bottom of the cloud simultaneously. This is a problem for slitless spectrographs, because the spectra from the branch-
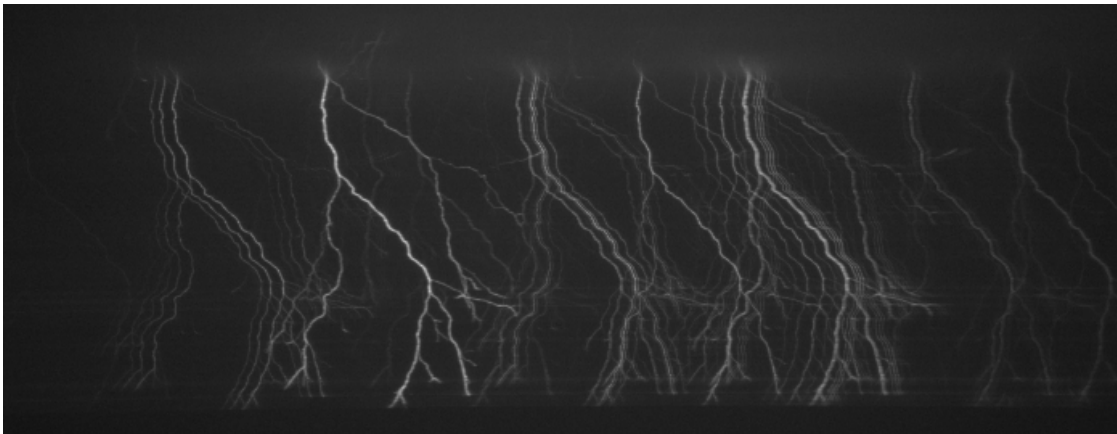
Figure 7.12: Spectral image of a downward stepped leader.

es/additional channels overlap, making it very difficult to discern which emissions belong to which spectral lines. It also artificially inflates the intensity values for

a spectral line, essentially making accurate temperature estimates impossible. An example of this is shown Figure 7.12. In this image, it is difficult to observe a clear spectra at any given row, and the branches from the leader channel overlap other spectra. However, for the large dataset from the work in this dissertation, nine stepped leaders were able to be clearly imaged with clear spectral lines. An example of one of these clear spectra is shown in Figure 7.13. Notice that this
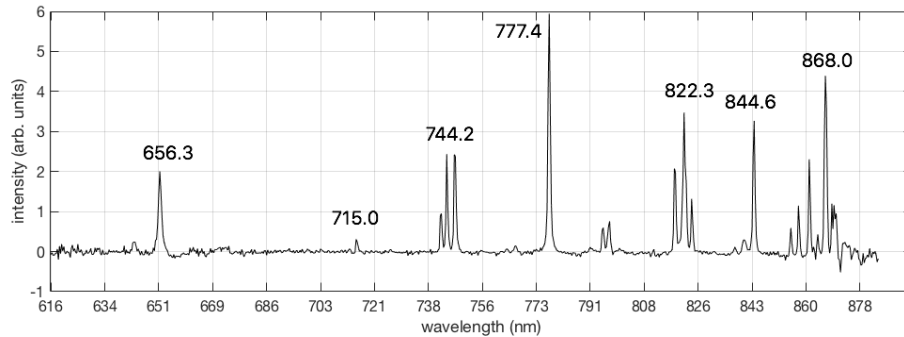
Figure 7.13: Spectral profile of a downward stepped leader.

spectrum closely resembles the spectrum for an IC leader (Figure 7.9b). It also is very similar to the spectra of triggered lightning return strokes from *Walker and Christian* [2017], shown in Figure 5.5 (bottom panel), except without the emission lines of singly ionized Nitrogen (NII) at 648.2 and 661.0 nm.

From the nine leader spectra, two of them contained clear spectra for a large portion of the downward stepped leader channel. These spectra were aligned in accordance to section 7.1, and the number of rows integrated to improve the SNR was 5. Thus, a coherently integrated spectra was produced every 5 rows for the length of the leader channel, which for the two flashes presented here, resulted in about forty data points for each frame. Images of the first flash are shown in Figure 7.14. This stepped leader spectra was observed for three consecutive frames, each with a duration of 32 μs. The channel segment analyzed was bounded by the
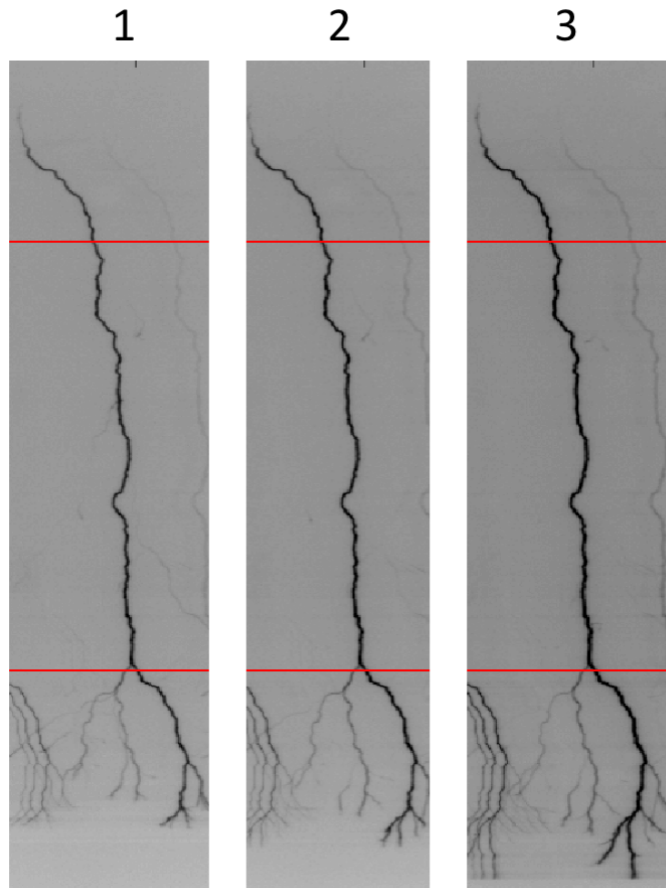
Figure 7.14: Images of a stepped leader channel that was visible for three frames (32 μs time resolution). The red lines bound the region used to calculate the leader channel temperature.

red lines in Figure 7.14. The associated temperature estimates for each frame are shown in Figure 7.15. The panels in Figure 7.15 show the temperature as a function of vertical pixel, with the initial and final vertical pixel indicated by the top and bottom red lines bounding the channel in Figure 7.14. The temperature plots are relatively smooth and continuous, with little variation for each frame. Each frame shows the temperature increase with increasing vertical pixel, which corresponds to a lower altitude in Figure 7.14. Thus, the temperature along the channel at each

time period (frame) is lowest at the top of the channel and highest at the bottom of the channel. The mean temperature of the channel also increases with each frame, with values of 13,600 K, 14,700 K, and finally 16,000 K. The maximum and minimum temperatures also increase with increasing frame. The last frame (frame
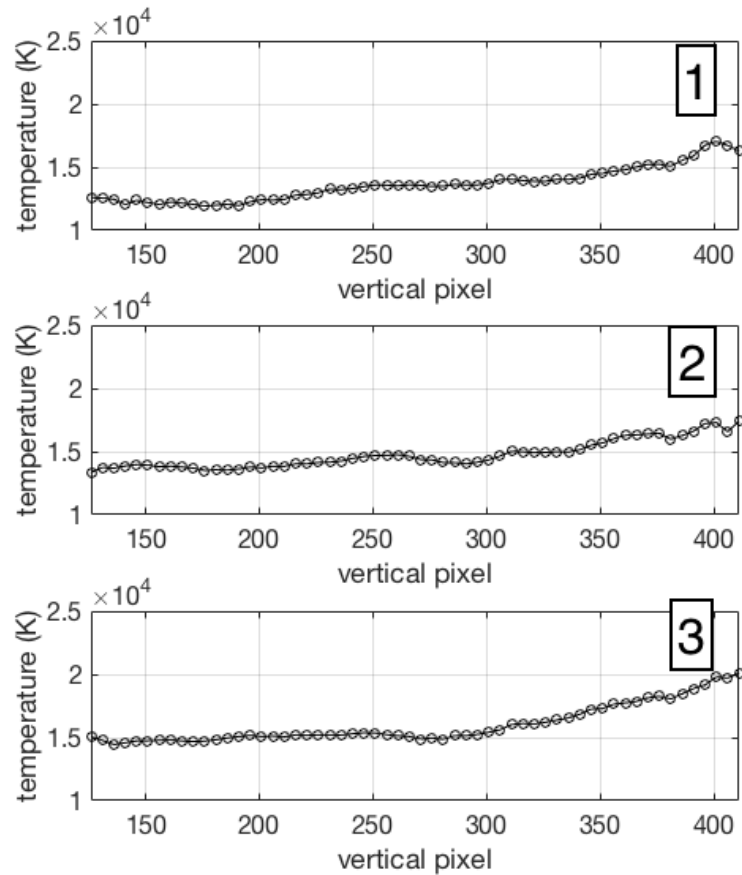
Figure 7.15: Stepped leader channel temperature for the flash in Figure 7.14. The number to the upper right of the panel indicates the frame number shown in Figure 7.14.

3) occurs right before the return stroke takes place, which means the temperature of the leader channel increased in time up until the onset of the return stroke. Due to the sensitive spectrograph settings to capture the dimly lit lightning leader, the

115

return stroke saturated the CMOS sensor of the high-speed camera, which did not
allow the associated return stroke temperature to be calculated.
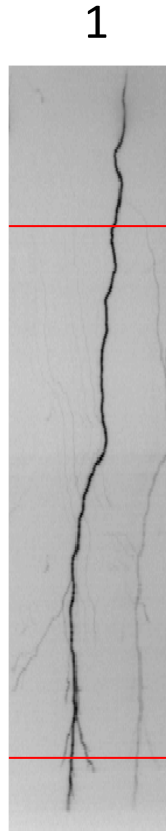
Figure 7.16: Image of a downward stepped leader visible for a single frame (32 μs
time resolution). The red lines bound the temperature shown in Figure 7.17.

The other downward stepped leader with a large portion of a leader channel
spectrum is shown in Figure 7.16. This flash only produced a single frame with
clear spectra for quantitative temperature analysis, and this frame occurred right
before the onset of the return stroke. This image was captured with the same
time exposure as Figure 7.14. Once again, the temperature was calculated for
the region bounded by the horizontal red lines. The temperature as a function of

vertical pixel is shown in Figure 7.17. Notice, that this stepped leader shows the opposite behavior to that of other stepped leader, in that the temperature decreases with decreasing altitude. The mean temperature of the channel is similar to the other leader, being 15,400 K.
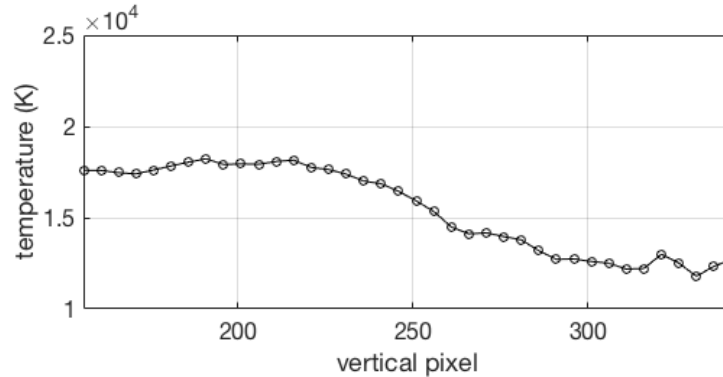
Figure 7.17: Stepped leader channel temperature for the flash in Figure 7.16.

For five of the stepped leaders, enough successive frames of each leader showed clear spectra to allow the temperature to be calculated as a function of time. These spectra were not visible for large sections of the leader channel such as Figures 7.14 and 7.16, but small vertical segments of each stepped leader were used to calculate the leader temperature. These segments were also coherently integrated to improve the SNR, with the row integrations of around ten for each spectra. The time-evolved spectra are shown in Figure 7.18. The exposure for each frame was the same as the stepped leaders in figures above, which was 32 μs. The successive time steps ranged from four to six frames. All of the stepped leaders show the temperature increase with time as the leader approaches the ground. Each leader in Figure 7.18 connects with the ground with the onset of the return stroke at the end of the last time step. The amount of temperature increase as a function of time ranges from about 1,000 K for some of the leaders to almost 7,000 K for

117
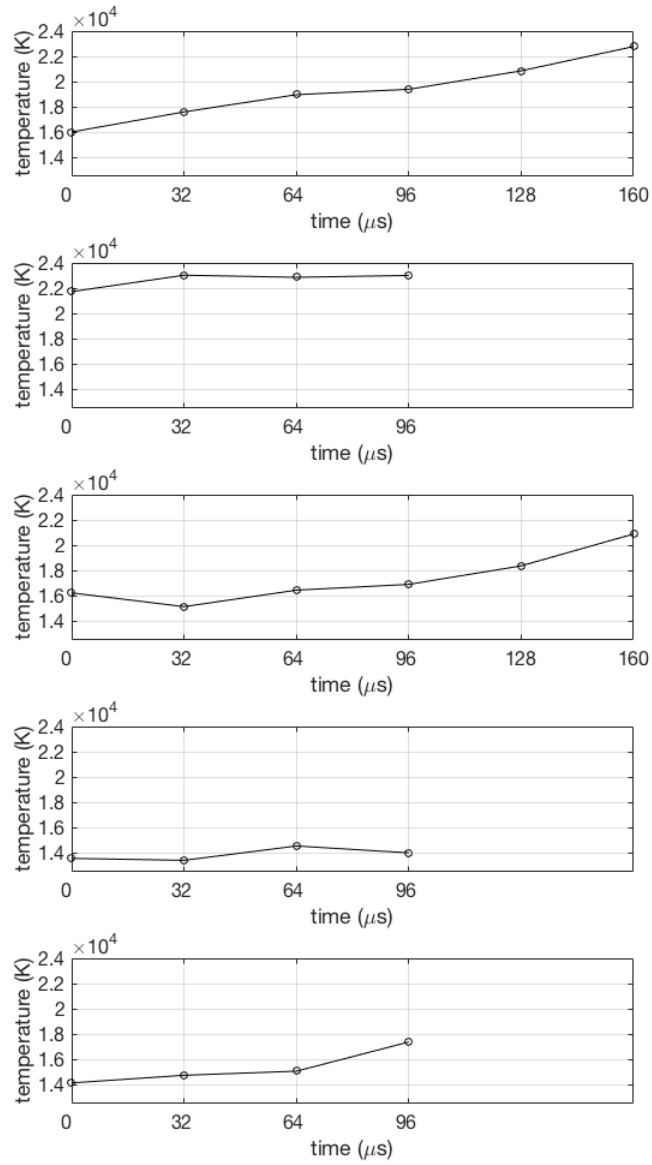
Figure 7.18: Panels showing the time evolution of temperature for five stepped leaders.

118

others.

Finally, Figure 7.19 shows the mean temperature for all the stepped leaders from this study. The values ranged from approximately 13,000 K to as large as 24,000 K. The mean temperature across all the leaders was 16,700 K, with a standard deviation of 3,200 K. This mean is colder than the IC leaders from section 7.2, and both the standard deviation and range is larger than the IC leaders.
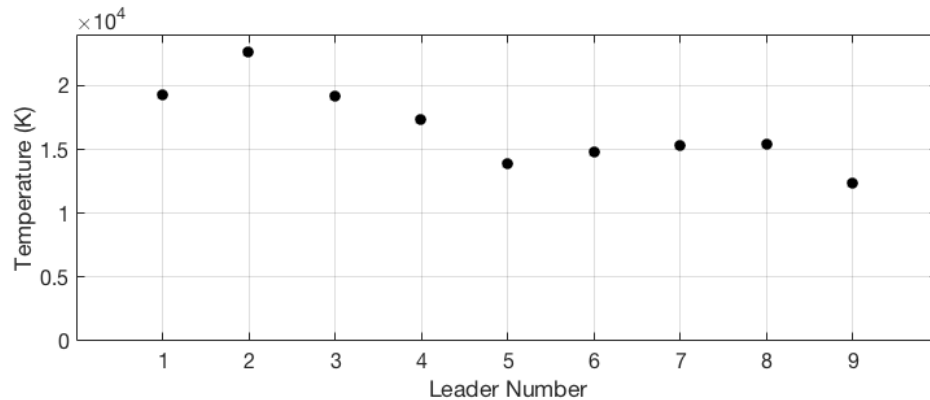
Figure 7.19: Mean temperatures for all of the stepped leaders from this study.

7.4   Dart Leaders

Clear dart leader spectra were much easier to obtain than the stepped leader spectra due to the dart leaders having fewer branches and the dimly lit 715.0 nm (OI) spectral line was much more visible. For the stepped leaders, the 715.0 nm (OI) emission line was typically only visible as the leader tip was close to the ground. An example a dart leader spectra is shown in Figure 7.20. Notice the lack of branches and overlapping spectra compared with the stepped leader (Figure 7.12). An example of a typical dart leader spectral profile is shown in Figure 7.21. Notice that this spectrum is very similar to the IC and stepped leader spectra, with

119

the neutral Oxygen and Nitrogen emission lines dominating. Out of the eighteen dart leaders, six of them had clear and unambiguous spectra for large sections of the dart leader channel. All of the dart leader channels showed similar behavior, and thus only three dart leaders from the same flash are presented here.
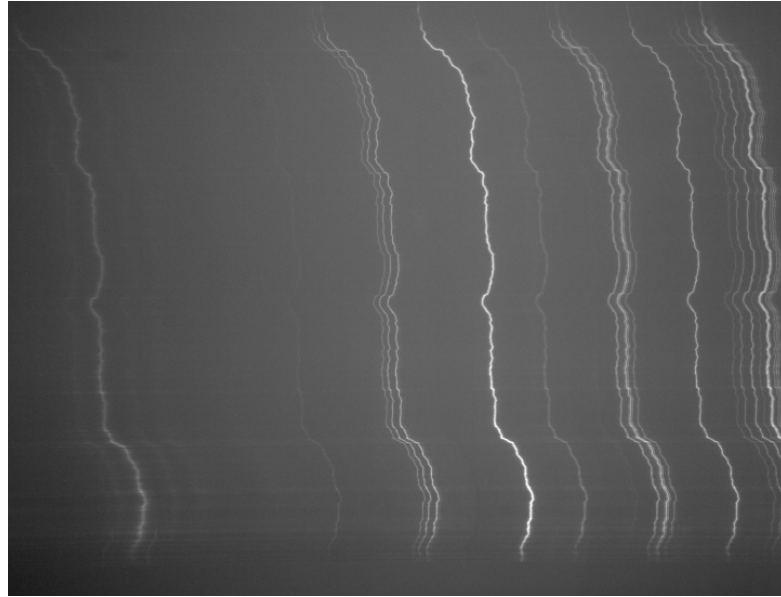
Figure 7.20: Spectral image of a dart leader.
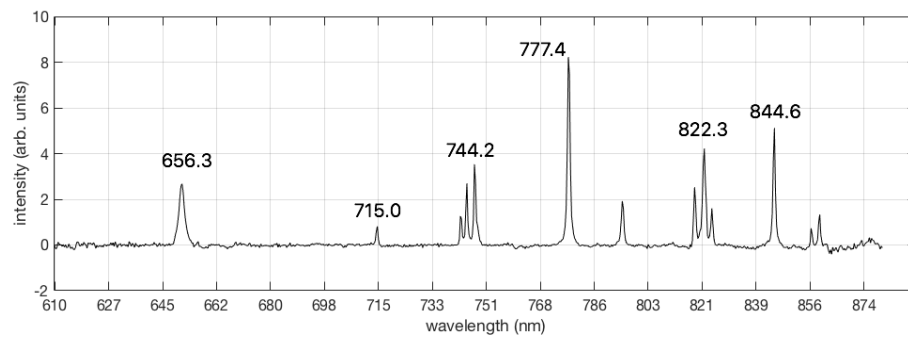
Figure 7.21: Spectral profile of a dart leader.

The first dart leader with clear spectra for a large section of the channel is shown in Figure 7.22. This dart leader was observed for nine frames, each with

32 μs resolution. Due to the relatively large speed of the dart leader compared to the stepped leader, clear propagation and extension of the dart leader channel is observed with each consecutive frame in Figure 7.22. Similarly as the temperature estimates for the stepped leaders, the red lines in Figure 7.22 show the bounded region where the temperature was calculated for the dart leader channel. The temperature profiles for each frame are shown in Figure 7.23. With the exception of frames 4 and 5, the temperature increases with increasing vertical pixel (decreasing altitude), similar to the stepped leader in Figure 7.15. Although, the dart leader channel at higher altitudes (smaller vertical pixel) cools off with each frame, which is opposite of the stepped leader in Figure 7.15. This creates a large temperature contrast between lower and upper altitudes along the dart leader channel, with minimums of the frames in Figure 7.23 being around 12,000 K and the maximums around 20,000 K. This information is supported by the time evolution of the dart leader shown in Figure 7.24. The temperature in Figure 7.24 were created by averaging over the entire channel for each frame in Figure 7.23. The overall cooling of the dart channel is reflected by the upper panel in Figure 7.24, with the mean channel temperature decreasing from 17,000 K to about 14,000 K over the duration of the dart leader propagation. After this last time step the dart leader connects with ground and the return stroke ensues. Interestingly, the maximum temperature along the channel actually has an overall increasing trend as it evolves with time and the minimum temperature along the channel decreases over time. This means that as the dart leader propagates toward the ground, the temperature gradient along the channel increases, and with the hottest temperatures closest to ground and the coldest temperatures at higher altitudes. This is contrary to the stepped leader from Figure 7.15, which shows the entire stepped leader channel increasing

121
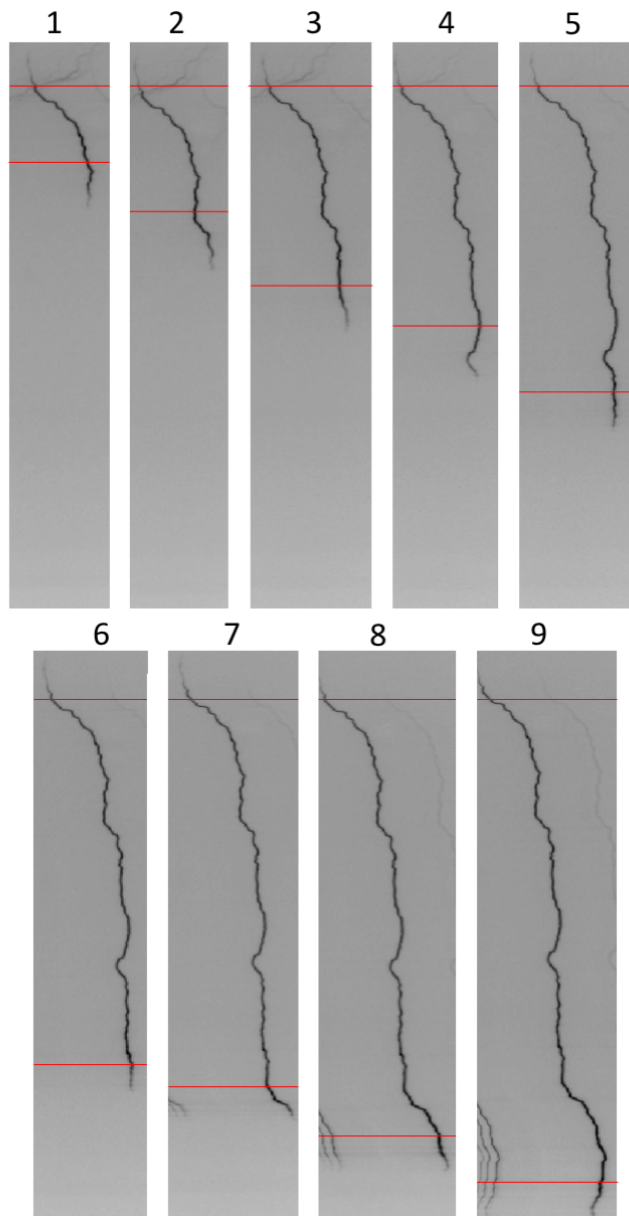
Figure 7.22: Images of a dart leader channel that was visible for nine frames (32 μs time resolution). The red lines bound the region used to calculate the dart leader channel temperature.

in temperature as the leader approached the ground, effectively maintaining a constant temperature gradient across the length of the channel.
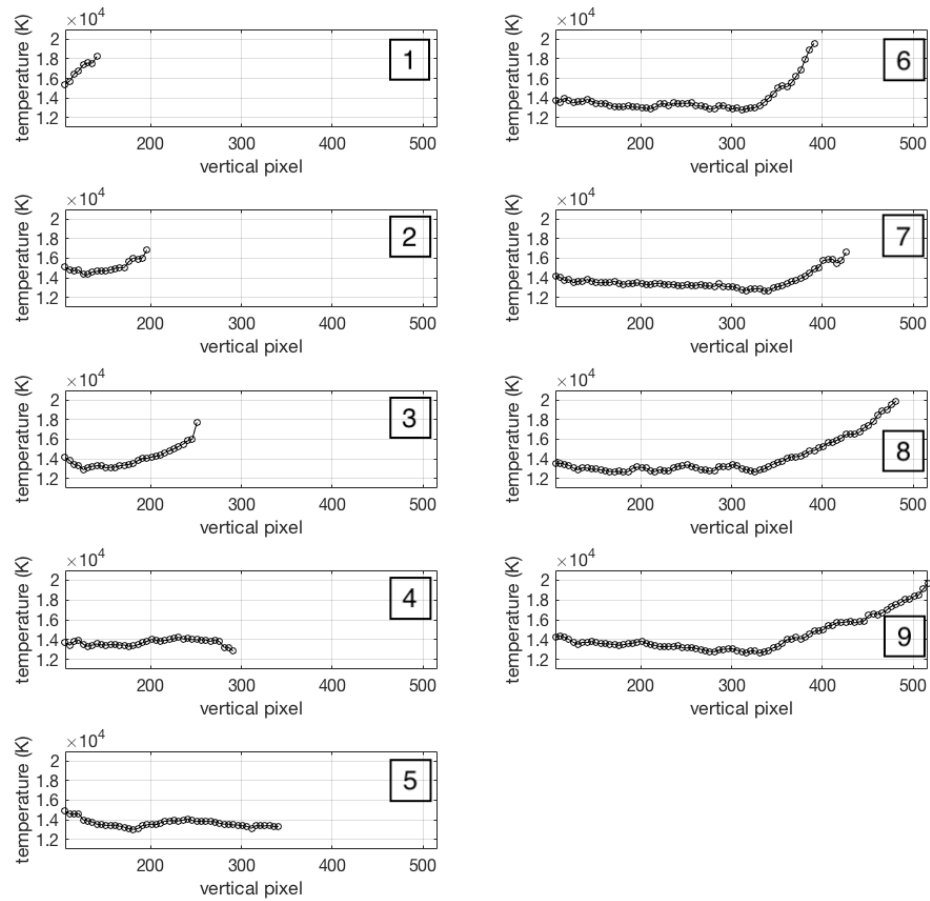
Figure 7.23: Dart leader channel temperature for the flash in Figure 7.22. The number to the upper right of the panel indicates the frame number shown in Figure 7.22.

The second dart leader of the same flash is shown in Figure 7.25. This dart leader was only observed for five frames instead of nine over the same spatial domain, implying it moved faster toward the ground. Figure 7.26 shows similar features as that observed in Figure 7.23, with the temperature being hottest from the channel that is nearest the ground (larger vertical pixel). Again, the dart leader channel shows a smooth increase in temperature along the length of the

123
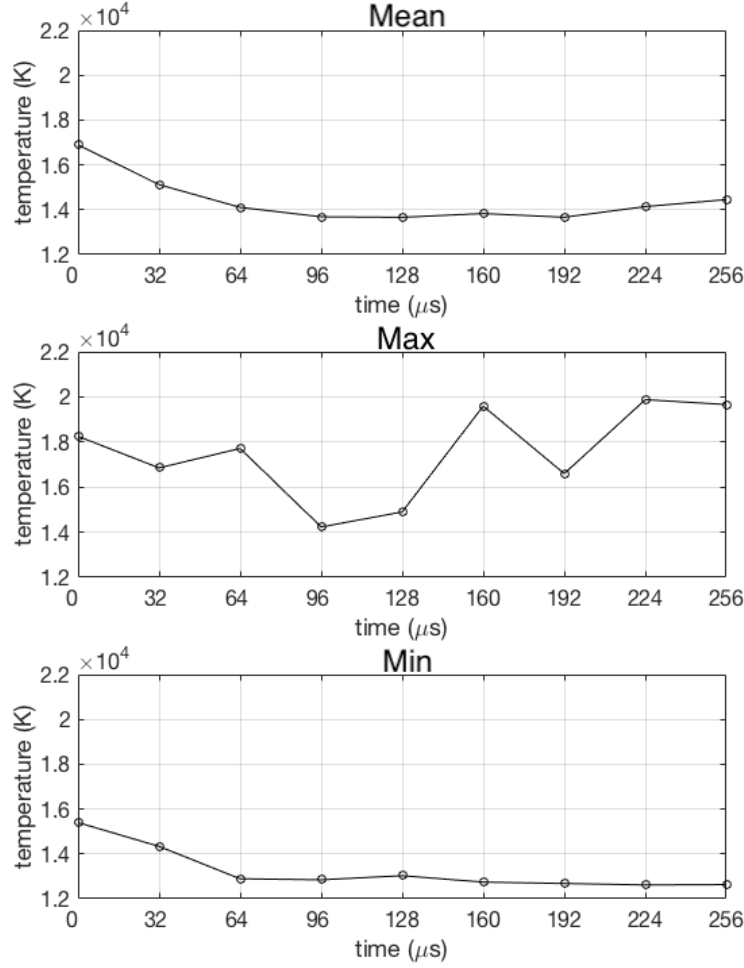
Figure 7.24: Time evolution of the temperature for the dart leader in Figure 7.22.

channel. The decrease in channel temperature for the upper portion of the channel (smaller vertical pixel) with increasing frame (time) is also evident. Supporting this is the time evolution of the leader shown in Figure 7.27. The upper panel of Figure 7.27 shows the mean temperature of the dart leader channel for each frame, indicating a decreasing trend as the leader approaches the ground. The maximum temperature again increases and the minimum decreases with time,
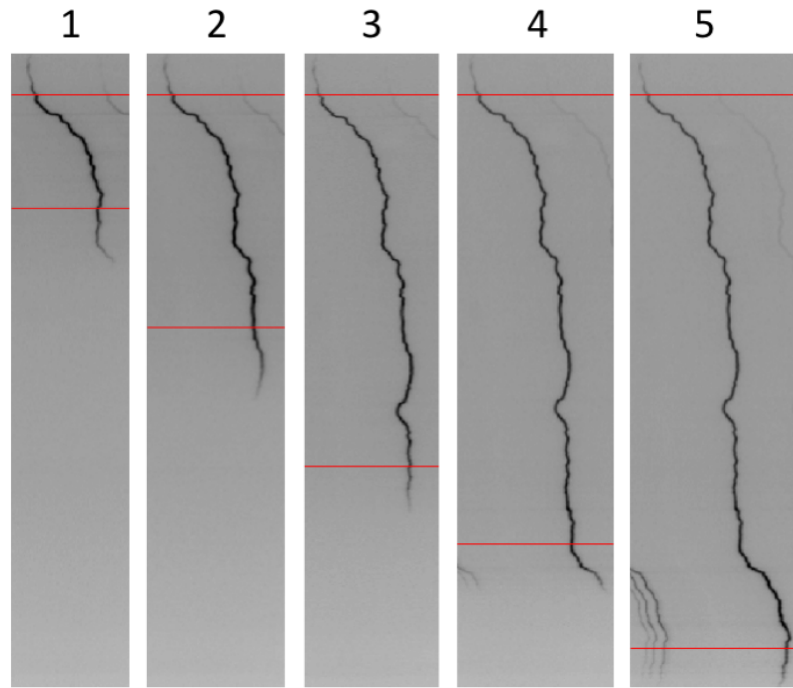
Figure 7.25: Images of the second dart leader channel from the flash producing the initial dart leader in Figure 7.22. The red lines bound the region used to calculate the dart leader channel temperature.

similar to Figure 7.24. However, the minimum temperature has a sharper decrease, beginning at a temperature of about 18,000 K and ending with a temperature of about 11,000 K. This is much greater than the decrease in Figure 7.24, which had a decrease of about 2,000 K over the nine frames of propagation. This means the temperature gradient along the channel for the second dart leader was even more drastic than the initial dart leader. Although the maximum temperatures from the first two dart leaders were about the same, and both mean temperatures decreased with time, the second dart leader had an overall hotter temperature than the first. The average temperature over the length of the channel and over all the frames for the first leader was 14,300 K compared with almost 16,000 K for the second dart leader.
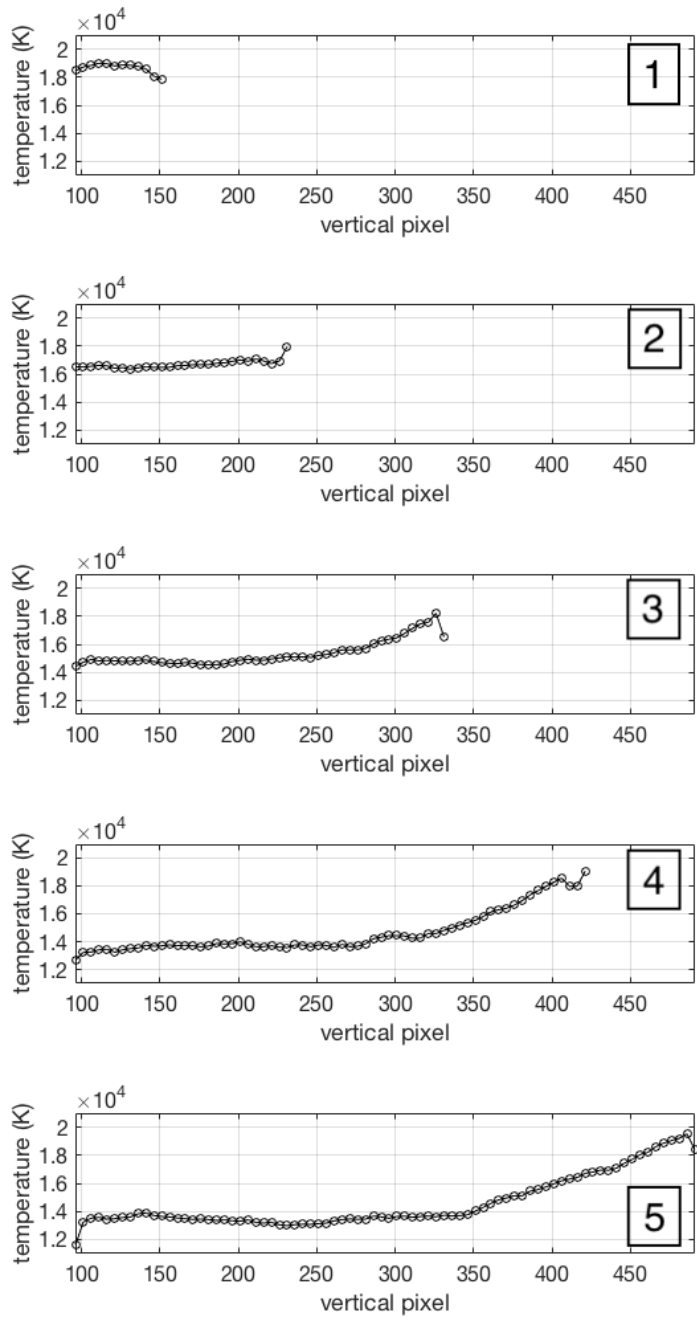
Figure 7.26: Dart leader channel temperature for the flash in Figure 7.25. The number to the upper right of the panel indicates the frame number shown in Figure 7.25.

126
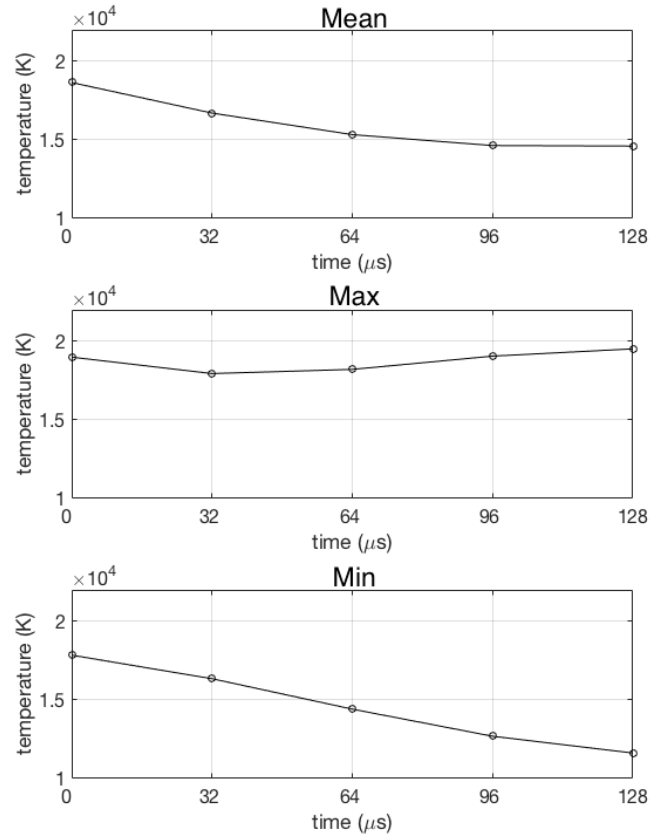
Figure 7.27: Time evolution of the temperature for the dart leader in Figure 7.25.

The last dart leader for this flash is shown in Figure 7.28. Notice that this dart leader only took two frames to connect with the ground, compared to the first and second dart leaders of nine and five frames. This suggests that each subsequent dart leader propagates with a faster speed toward the ground. The associated dart leader channel temperature is shown in Figure 7.29. The initial frame of this dart leader shows modest temperature values, but this may be due to it just barely emerging from the cloud. The last frame before the dart leader connects with ground (frame 2) shows a steady temperature value for a large section of
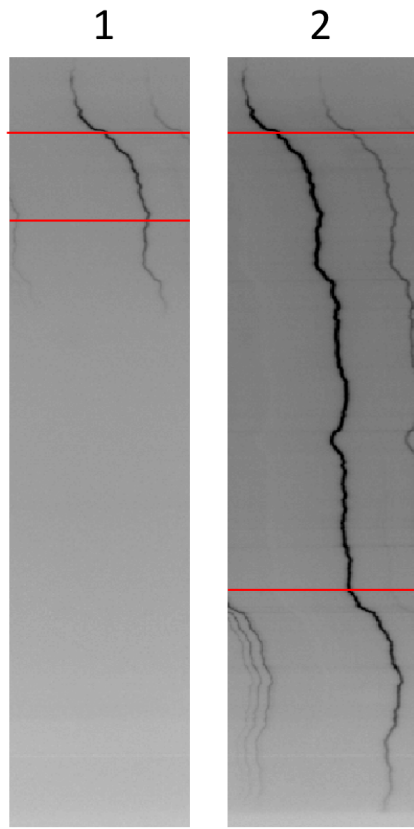
Figure 7.28: Images of the last dart leader channel from the flash producing the initial dart leader in Figure 7.22. The red lines bound the region used to calculate the dart leader channel temperature.

the channel, with a much hotter temperature than previous dart leaders (around 21,000 K). At the section of the dart leader closest to ground (vertical pixel 320 to 450) there is a an increase in temperature to a local maximum of about 23,000 K before dropping a local minimum of about 18,000 K for the lowest altitude of the channel. This contrasts the previous two dart leaders, which showed the maximums of the dart channel being closest to the ground (larger in vertical pixel). Also different is the dart leader temperature increases in overall temperature from frame 1 to frame 2, although as mentioned before, this could be due to the initial

128
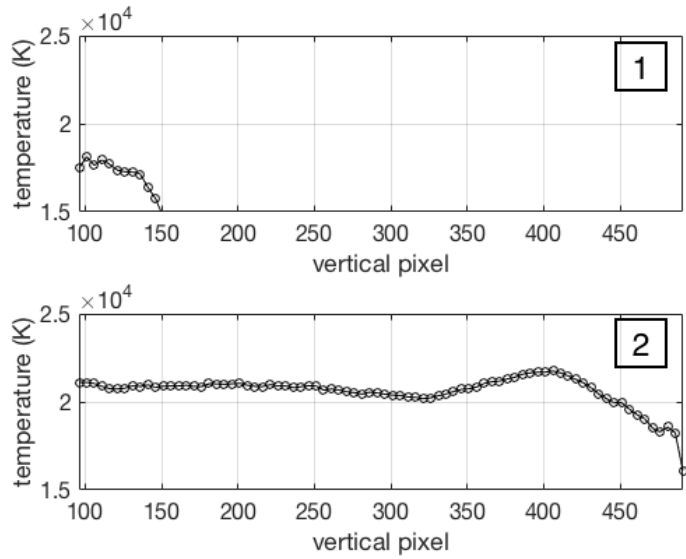
Figure 7.29: Dart leader channel temperature for the flash in Figure 7.28. The number to the upper right of the panel indicates the frame number shown in Figure 7.28.

frame only capturing a tiny portion of the dart leader channel.
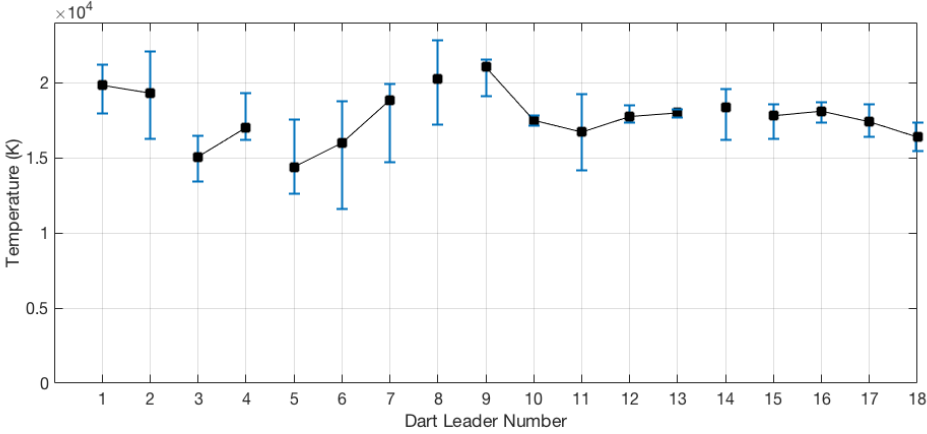
Figure 7.30: Mean temperature for all the dart leaders from this study. The black box represents the mean along the channel and across all the frames for each dart leader, with the brackets representing the maximum and minimum temperatures for each dart leader. The lines connecting each dart leader indicate the dart leaders were part of the same flash.

Figure 7.30 shows the average, maximum, and minimum temperatures for all

129

the dart leaders from this study. The average temperatures ranged from approximately 15,000 K to 22,000 K. Interestingly, there seems to not be any correlation between dart leader order of the same flash with temperature. The dart leaders presented above in Figures 7.22, 7.25, and 7.28 are shown as dart leader numbers 5-7 in Figure 7.30, and thus they show a hotter temperature with each subsequent dart leader. However, the flashes composing dart leader numbers 1-2, 9-13, and 15-18 show that subsequent dart leaders decrease in temperature. The mean temperature of all the dart leaders is 17,800 K with a standard deviation of 6,600 K. This mean is between the IC and stepped leader means, but the standard deviation is much larger. This may be due to the sample size being larger for the dart leaders.

7.5   Summary of Spectroscopy Results

From this observational campaign, the spectra of six IC leaders (six flashes), nine stepped leaders (nine flashes), and eighteen dart leaders (seven flashes) were studied. These spectra showed clear emissions lines from neutral Oxygen and Nitrogen and H-alpha and did not show any singly ionized emission lines. The spectral profiles of the IC, stepped, and dart leaders all were very similar, and had clear lines of 715 nm (OI) and 777.4 nm (OI) to be used for temperature calculations. This study was the first to report on IC leader temperatures, with values ranging from 12,000 K to 25,000 K. This study also provided the most complete analysis of stepped and dart leaders, showing the evolution of the leader channel temperatures as a function of space and time. The uncertainties for the temperature estimates in this dissertation ranged from 7 to 10%, translating to values of 1,000 to 2,500

K. The relatively low uncertainties were in part due to digital signal processing techniques to improve the SNR of the lightning spectral emission lines.

The stepped leader channel temperatures reported here range from approximately 12,000 K to 24,000 K. These values are lower than the study of *Orville* [1968], who found a stepped leader temperature of 30,000 K. However, the uncertainty in that study was relatively large, with values up to 10,000 K. This puts the temperature of *Orville* [1968] within range of the leader temperatures here. However, it should be noted that the study of *Orville* [1968] used instrumentation that was novel at the time, but had limitations compared to the modern high-speed spectrograph built for this dissertation, such as underexposure of images and non-linear wavelength reaction of the film used to produce the spectra. That study also only captured a single measurement from a 2 meter section of the leader channel, which may have contributed to the temperature calculation found in that study to differ from the temperatures reported in this dissertation. A modern spectroscopic study of lightning leaders found leader temperatures of the leader tip and channel to range from 13,000 to 16,000 K [*Chang et al.*, 2017]. These values align with the temperature estimates found from the work presented here. However, *Chang et al.* [2017] found that the stepped leader temperature increased with time and then decreased with time for the same leader. This is not consistent with the findings of this dissertation, which found that the leader temperature increased with time for all the stepped leaders analyzed. Also, for the first time, this dissertation reported on the leader channel temperature over a long channel segment, finding that the temperature is hottest for the segment nearest the ground for one leader, while another showed cooling near the ground. It should be noted that *Chang et al.* [2017] used much larger exposures of the leader channel than the results from this

dissertation (150 μs compared to 32 μs), did not say which emission lines they used for their calculations, and did not report on the temperature uncertainties in their calculations. This may explain the differences found between that study and this dissertation.

This dissertation also presented spectral and temperature characteristics for several dart leaders belonging to several different flashes. The dart leader temperatures from this study ranged from 13,000 K to 24,000 K, similar to stepped leaders. This values encompass the dart leader temperatures reported in the literature from *Orville* [1975] and *Chang et al.* [2017], which found both found values around 20,000 K. This dissertation also reported on the temperature variation along the dart leader channel and how this channel varies with time and from across multiple dart leaders of the same flash. For the dart leader channel, *Chang et al.* [2017] found similar results of the dart leader channel being hotter in temperature for the channel section closest to the ground, only they found temperature differences along the channel of about 100 K for a single frame (200 μs). The work from this dissertation found temperature differences of up to 7,000 K, significantly greater. Also, this dissertation was the first to report the evolution of the dart leader channel for multiple frames and for multiple dart leaders of the same flash. The flashes with detailed results of large portions of the dart leader channel show that the average channel temperature decreases with time as the dart leader approaches the ground, opposite of stepped leaders. But, the overall average temperature of the dart channel increases with subsequent darts of the same flash.

In summary, these results indicate that IC, stepped, and dart leaders all have similar temperatures, with mean overall sample values around 16,600 to 18,900 K. Also, for stepped and dart leader channels, the temperature is not uniform

across the channel, but hotter temperatures are closest to the ground. This has implications for spectroscopy systems that only observe a small portion of the leader channel, due to the spectra-derived temperature being altitude dependent. Also, for negative stepped leaders, the temperature gradient across the channel remains nearly constant, and the mean temperature increases as the stepped leader approaches the ground. This is different from dart leaders, that have a temperature gradient across the channel that increases with time, and a mean channel temperature that decreases as the leader approaches the ground.

Chapter 8

Conclusions

This Chapter summarizes the scientific contributions of the dissertation and provides suggestions for future work.

8.1 Thunderstorm Charge Structures Producing Gigantic Jets

Chapter 3 provided rigorous data analysis of gigantic jet producing thunderstorms and numerical modeling of gigantic jet discharges. The data analysis involved combining weather radar variables such as base reflectivity, radial velocity, and spectrum width with low frequency and very high frequency lightning data to identify common features that lead to gigantic jet formation. This study found that thunderstorms producing gigantic jets exhibit an intense convective pulse during the time of the gigantic jet, and this pulse is associated with strong storm top divergence and storm top mixing as identified by large values of radial velocity

134

differential and spectrum width. These features are also associated with a narrow upper positive charge region during the time of the gigantic jet, as found from VHF lightning data. This charge structure with narrow upper positive charge was then used as an input to a stochastic fractal model that simulates lightning discharge trees. The discharge trees closely matched observations of gigantic jet lightning, as opposed to charge structures with wide upper positive charge, which were also simulated. In conclusion, this study found that gigantic jet charge structures consist of a narrow upper positive charge region above a wide middle negative charge region and they are a result of an intense convective pulse.

8.2 Satellite and Video Observations of Gigantic Jets

In Chapter 4, satellite observations from GOES-16 were made of several gigantic jet discharges that were simultaneously recorded from a ground-based low-light-level video camera. The satellite instruments used for the study were the Advanced Baseline Imager (ABI) and the Geostationary Lightning Mapper (GLM). The ABI provided infrared (IR) data for cloud top estimates and storm structure information, and the GLM recorded the optical emissions (777.4 nm) associated with the gigantic jets. The gigantic jet lightning exhibited larger peak flash energies, longer durations of continuous emissions, and smaller lateral propagation distances than other lightning observed by GLM. The largest optical energies of each gigantic jet were concentrated in a single GLM pixel throughout the durations the gigantic jets. The peak in optical energy occurred during the video frame when the gigantic jet connected with the ionosphere.

8.3 Quantitative Lightning Spectroscopy

In Chapter 7, spectra of intracloud, stepped, and dart leaders were presented. These spectra were recorded by a high-speed spectroscopy system that was built as part of the work for this dissertation. The lightning spectra were recorded at spectral resolutions of 0.25 nm/pixel and time resolutions ranging from 16 to 200 μs. For some of the stepped and dart leader spectra, large segments of the leader channel were recorded. Using the spectral lines of 715.0 (OI) and 777.4 nm (OI), the temperature was calculated for the leader spectra. All of the leader spectra had mean temperature values ranging from 16,000 to 19,000 K. For stepped and dart leaders, the temperature was not uniform across the channel, but was hotter for the channel segment closest to ground. For stepped leaders, the temperature gradient across the channel was nearly constant, with the mean temperature increasing as the leader approached ground. This was different from dart leaders, which had a temperature gradient across the channel that increased and a mean temperature that decreased as the leader approached the ground.

8.4 Future Work

For the studies completed in this dissertation, meaningful future work would involve extending the GLM observations of gigantic jets to allow for automated detection by GLM. Considering GLM has a large field-of-view (nearly a hemisphere) and continuous observations during both day and night, it is ideal for monitoring and detections of gigantic jets. Future work on this topic would involve writing algorithms to automatically detect gigantic jets, such as filtering for detections that have long continuous emissions and large integrated optical energies of a single

pixel for a given GLM detected flash. This data could be correlated with other data, such as LF lightning networks, which would help filter the GLM detections because gigantic jet lightning should only be assoicated with intracloud events. To better construct the GLM detection algorithms, larger datasets of ground truth could be obtained from utilizing all-sky camera networks across the United States.

Another area of future work would involve correlating the lightning leader spectra to other measurements, such as LF and VHF lightning data and ELF magnetic field data. The LF lighting data would provide the peak current of the flashes and the polarity, allowing for correlations with the temperature of the lightning leaders. The ELF data would provide the charge moment change, which provides the amount of charge transferred by a discharge, allowing correlation with the leader temperature. The electron density of the lightning leaders could also be calculated and correlated with these measurements. The spectroscopy observations could also be extended to upward discharges such blue and gigantic jets. The system has the capability to observe these events with the inclusion of a vertical slit and an image intensifier. Spectra of these discharges would be novel and never before captured, and provide insightful information about the plasma nature of these events.

Bibliography

Arns, J. A., W. S. Colburn, and S. C. Barden (1999), Volume phase gratings for spectroscopy, ultrafast laser compressors, and wavelength division multiplexing, in *Current Developments in Optical Design and Optical Engineering VIII*, vol. 3779, pp. 313–323, International Society for Optics and Photonics.

Bazelyan, E. M., and Y. P. Raizer (1998), *Spark Discharge*, Chemical Rubber Company Press, New York, NY.

Bazelyan, E. M., and Y. P. Raizer (2000), *Lightning Physics and Lightning Protection*, IoP Publishing Ltd, Bristol, UK.

Behnke, S. A., R. J. Thomas, P. R. Krehbiel, and W. Rison (2005), Initial leader velocities during intracloud lightning: Possible evidence for a runaway breakdown effect, *J. Geophys. Res.*, *110*(D12), D10207, doi:10.1029/2004JD005312.

Bitzer, P. M. (2017), Global distribution and properties of continuing current in lightning, *Journal of Geophysical Research: Atmospheres*, *122*(2), 1033–1041.

Blake, E., and D. Zelinsky (2017), National hurricane center tropical cyclone report, hurricane harvey, *Tech. Rep. AL092017*, NOAA.

Blakeslee, R. J., H. J. Christian, and B. Vonnegut (1989), Electrical measurements over thunderstorms, *J. Geophys. Res.*, *94*, 13,135–13,140.

Blyth, A. M., W. A. Cooper, and J. B. Jensen (1988), A study of the source of entrained air in montana cumuli, *Journal of the atmospheric sciences*, *45*(24), 3944–3964.

Boggs, L. D., N. Y. Liu, M. Splitt, S. Lazarus, C. Glenn, H. K. Rassoul, and S. A. Cummer (2016), An analysis of five negative sprite-parent discharges and their associated thunderstorm charge structures, *J. Geophys. Res.*, *121*(2), 759–784, doi:10.1002/2015JD024188.

Boggs, L. D., N. Y. Liu, J. A. Riousset, F. Shi, S. Lazarus, M. Splitt, and H. K. Rassoul (2018), Thunderstorm charge structures producing gigantic jets, *Scientific Reports*, *8*, 18,085.

Boggs, L. D., N. Liu, M. Peterson, S. Lazarus, M. Splitt, F. Lucena, A. Nag, and H. K. Rassoul (2019), First observations of gigantic jets from geostationary orbit, *Geophysical Research Letters*, *46*(7), 3999–4006.

Brewster, K. A., and D. S. Zrnic (1986), Comparison of eddy dissipation rates from spatial spectra of doppler velocities and doppler spectrum widths, *Journal of Atmospheric and Oceanic Technology*, *3*(3), 440–452.

Brown, R. A., and K. L. Torgerson (2003), Interpretation of single-Doppler radar signatures in a V-shaped hailstorm: Part I-Evolution of reflectivity-based features, *Natl. Wea. Dig.*, *27*, 3–14.

Bruning, E. C., W. D. Rust, D. R. MacGorman, M. I. Biggerstaff, and T. J. Schuur (2010), Formation of charge structures in a supercell, *Monthly Weather Review*, *138*(10), 3740–3761.

Buechler, D., T. Varghese, P. Armstrong, J. Bremer, R. Lamb, J. Fulbright, and S. Goodman (2018), On-orbit validation of the geolocation accuracy of goes-16 geostationary lightning mapper (glm) flashes using ground-based laser beacons, in *Earth Observing Systems XXIII*, vol. 10764, p. 107640J, International Society for Optics and Photonics.

Byrne, G. J., A. A. Few, and M. E. Weber (1983), Altitude, thickness and charge concentration of charged regions of four thunderstorms during trip 1981 based upon in situ balloon electric field measurements, *Geophys. Res. Lett.*, *10*, 39–42.

Calhoun, K. M., D. R. MacGorman, C. L. Ziegler, and M. I. Biggerstaff (2013), Evolution of lightning activity and storm charge relative to dual-doppler analysis of a high-precipitation supercell storm, *Monthly Weather Review*, *141*(7), 2199–2223.

Cen, J., P. Yuan, S. Xue, and X. Wang (2015), Spectral characteristics of lightning dart leader propagating in long path, *Atmospheric Research*, *164*, 95–98.

Chang, X., P. Yuan, J. Cen, and X. Wang (2017), Variation of the channel temperature in the transmission of lightning leader, *Journal of Atmospheric and Solar-Terrestrial Physics*, *159*, 41–47.

Chen, A. B., C.-L. Kuo, Y.-J. Lee, H.-T. Su, R.-R. Hsu, J.-L. Chern, H. U. Frey, S. B. Mende, Y. Takahashi, H. Fukunishi, Y. S. Chang, T.-Y. Liu, and L.-C. Lee (2008), Global distributions and occurrence rates of transient luminous events, *J. Geophys. Res.*, *113*, A08306, doi:10.1029/2008JA013101.

Chou, J. K., C. L. Kuo, L. Y. Tsai, A. B. Chen, H. T. Su, R. R. Hsu, S. A. Cummer, J. Li, H. U. Frey, S. B. Mende, Y. Takahashi, and L. C. Lee (2010), Gigantic jets with negative and positive polarity streamers, *J. Geophys. Res.*, *115*, A00E45, doi:10.1029/2009JA014831.

Christian, H., R. Blakeslee, S. Goodman, D. Mach, M. Stewart, D. Buechler, W. Koshak, J. Hall, W. Boeck, K. Driscoll, et al. (1999), The lightning imaging sensor, in *NASA conference publication*, pp. 746–749, NASA.

Christian, H. J., R. J. Blakeslee, and S. J. Goodman (1989), The detection of lightning from geostationary orbit, *Journal of Geophysical Research: Atmospheres*, *94*(D11), 13,329–13,337.

Cochocki, A., and R. Unbehauen (1993), *Neural networks for optimization and signal processing*, John Wiley & Sons, Inc.

Crum, T. D., and R. L. Alberty (1993), The wsr-88d and the wsr-88d operational support facility, *Bulletin of the American Meteorological Society*, *74*(9), 1669–1688.

Cummer, S. A., J. Li, F. Han, G. Lu, N. Jaugey, W. A. Lyons, and T. E. Nelson (2009), Quantification of the troposphere-to-ionosphere charge transfer in a gigantic jet, *Nat. Geosci.*, *2*, 617–620, doi:10.1038/ngeo607.

Cummins, K., and M. Murphy (2009), An overview of lightning locating systems: History, techniques, and data uses, with an in-depth look at the U.S. NLDN, *IEEE Trans. Electromagn. Compat.*, *51*(3), 499–518.

da Silva, C. L., and V. P. Pasko (2013), Vertical structuring of gigantic jets, *Geophys. Res. Lett.*, *40*, 3315–3319, doi:10.1002/grl.50596.

da Silva, C. L., and V. P. Pasko (2013), Dynamics of streamer-to-leader transition at reduced air densities and its implications for propagation of lightning leaders and gigantic jets, *J. Geophys. Res.*, *118*(24), 13,561–13,590, doi:10.1002/2013JD020618.

Doviak, R. J., et al. (2006), *Doppler radar and weather observations*, Courier Corporation.

Dwyer, J. R. (2003), A fundamental limit on electric fields in air, *Geophys. Res. Lett.*, *30*(20), 2055, doi:10.1029/2003GL017781.

Dwyer, J. R., M. A. Uman, H. K. Rassoul, M. Al-Dayeh, L. Caraway, J. Jerauld, V. A. Rakov, D. M. Jordan, K. J. Rambo, V. Corbin, and B. Wright (2003), Energetic radiation during rocket-triggered lightning, *Science*, *299*(5607), 694–697, doi:10.1126/science.1078940.

Emersic, C., P. Heinselman, D. MacGorman, and E. Bruning (2011), Lightning activity in a hail-producing storm observed with phased-array radar, *Monthly Weather Review*, *139*(6), 1809–1825.

Fang, M., R. J. Doviak, and V. Melnikov (2004), Spectrum width measured by wsr-88d: Error sources and statistics of various weather phenomena, *Journal of Atmospheric and Oceanic Technology*, *21*(6), 888–904.

Fox, P. (1903), *Astrophys. J., 294.*

Gallimberti, I., G. Bacchiega, A. Bondiou-Clergerie, and P. Lalande (2002), Fundamental processes in long air gap discharges, *C. R. Physique, 3*(10), 1335–1359, doi:10.1016/S1631-0705(02)01414-7.

Goodman, S. J., D. Mach, W. J. Koshak, and R. J. Blakeslee (2012a), Algorithm theoretical basis document, *NOAA NESDIS Center for Satellite Applications and Research, 3.0.*

Goodman, S. J., R. J. Blakeslee, W. J. Koshak, D. Mach, J. Bailey, D. Buechler, L. Carey, C. Schultz, M. Bateman, E. McCaul Jr, et al. (2013), The goes-r geostationary lightning mapper (glm), *Atmospheric research, 125*, 34–49.

Huang, S.-M., R.-R. Hsu, L.-J. Lee, H.-T. Su, C.-L. Kuo, C.-C. Wu, J.-K. Chou, S.-C. Chang, Y.-J. Wu, and A. B. Chen (2012), Optical and radio signatures of negative gigantic jets: Cases from Typhoon Lionrock (2010), *J. Geophys. Res., 117*, A08307, doi:10.1029/2012JA017600.

Israel, H., and K. Wurm (1941), *Naturwissenshaften, 52*(778).

Istok, M. J., and R. J. Doviak (1986), Analysis of the relation between doppler spectral width and thunderstorm turbulence, *Journal of the atmospheric sciences, 43*(20), 2199–2214.

Kanmae, T., H. C. Stenbaek-Nielsen, and M. G. McHarg (2007), Altitude resolved sprite spectra with 3 ms temporal resolution, *Geophys. Res. Lett., 34*, L07810, doi:doi:10.1029/2006GL028608.

Kanmae, T., H. C. Stenbaek-Nielsen, M. G. McHarg, and R. K. Haaland (2010), Observation of sprite streamer head's spectra at 10,000 fps, *J. Geophys. Res.*, *115*, A00E48, doi:10.1029/2009JA014546.

Kollias, P., B. Albrecht, R. Lhermitte, and A. Savtchenko (2001), Radar observations of updrafts, downdrafts, and turbulence in fair-weather cumuli, *Journal of the atmospheric sciences*, *58*(13), 1750–1766.

Krehbiel, P. R. (1986), The electrical structure of thunderstorms, in *The Earth's Electrical Environment*, pp. 90–113, National Academy Press, Washington, D.C.

Krehbiel, P. R., R. J. Thomas, W. Rison, T. Hamlin, J. Harlin, and M. Davis (2000), Gps-based mapping system reveals lightning inside storms, *Eos, Transactions American Geophysical Union*, *81*(3), 21–25.

Krehbiel, P. R., J. A. Riousset, V. P. Pasko, R. J. Thomas, W. Rison, M. A. Stanley, and H. E. Edens (2008), Upward electrical discharges from thunderstorms, *Nat. Geosci.*, *1*, 233–237, doi:10.1038/ngeo162.

Krider, E. P. (1965), Time-resolved spectral emissions from individual return strokes in lightning discharges, *Journal of Geophysical Research*, *70*(10), 2459–2460.

Kuo, C. L., J. K. Chou, L. Y. Tsai, A. B. Chen, H. T. Su, R. R. Hsu, S. A. Cummer, H. U. Frey, S. B. Mende, Y. Takahashi, and L. C. Lee (2009), Discharge processes, electric field, and electron energy in ISUAL-recorded gigantic jets, *J. Geophys. Res.*, *114*(A13), A04314, doi:10.1029/2008JA013791.

Lang, T. J., L. J. Miller, M. Weisman, S. A. Rutledge, L. J. Barker III, V. Bringi, V. Chandrasekar, A. Detwiler, N. Doesken, J. Helsdon, et al. (2004), The severe thunderstorm electrification and precipitation study, *Bulletin of the American Meteorological Society*, *85*(8), 1107–1125.

Lazarus, S., M. Splitt, J. Brownlee, N. Spiva, and N. Y. Liu (2015), A thermodynamic, kinematic and microphysical analysis of a jet and gigantic jet-producing Florida thunderstorm, *J. Geophys. Res.*, *120*(16), 8469–8490, doi: 10.1002/2015JD023383, 2015JD023383.

Liu, N. Y., J. R. Dwyer, H. C. Stenbaek-Nielsen, and M. G. McHarg (2015a), Sprite streamer initiation from natural mesospheric structures, *Nat. Commun.*, *6*, 7540, doi:10.1038/ncomms8540.

Liu, N. Y., M. G. McHarg, and H. C. Stenbaek-Nielsen (2015b), High-altitude electrical discharges associated with thunderstorms and lightning, *J. Atmos. Solar Terr. Phys.*, doi:10.1016/j.jastp.2015.05.013.

Liu, N. Y., N. Spiva, J. R. Dwyer, H. K. Rassoul, D. Free, and S. A. Cummer (2015c), Upward electrical discharges observed above Tropical Depression Dorian, *Nat. Commun.*, *6*, 5995, doi:10.1038/ncomms6995.

López, J. A., J. Montanyà, O. A. van der Velde, N. Pineda, A. Salvador, D. Romero, D. Aranguren, and J. Taborda (2019), Charge structure of two tropical thunderstorms in colombia, *Journal of Geophysical Research: Atmospheres*, *124*(10), 5503–5515.

Lu, G., S. A. Cummer, W. A. Lyons, P. R. Krehbiel, J. Li, W. Rison, R. J. Thomas, H. E. Edens, M. A. Stanley, W. Beasley, D. R. MacGorman, O. A. van der Velde, M. B. Cohen, T. J. Lang, and S. A. Rutledge (2011), Lightning development associated with two negative gigantic jets, *Geophys. Res. Lett.*, *38*, L12801, doi:10.1029/2011GL047662.

MacGorman, D. R., and W. D. Rust (1998), *The Electrical Nature of Storms*, Oxford Univ. Press, New York, NY.

MacGorman, D. R., W. D. Rust, C. L. Ziegler, E. R. Mansell, T. J. Schuur, M. I. Biggerstaff, J. M. Straka, E. C. Bruning, K. M. Kuhlman, N. R. Lund, et al. (2008), Telex the thunderstorm electrification and lightning experiment, *Bulletin of the American Meteorological Society*, *89*(7), 997–1013.

MacGorman, D. R., M. S. Elliott, and E. DiGangi (2017), Electrical discharges in the overshooting tops of thunderstorms, *J. Geophys. Res.*

Mach, D. M., H. J. Christian, R. J. Blakeslee, D. J. Boccippio, S. J. Goodman, and W. L. Boeck (2007), Performance assessment of the optical transient detector and lightning imaging sensor, *Journal of Geophysical Research: Atmospheres*, *112*(D9).

Mackerras, D., M. Darveniza, R. E. Orville, E. R. Williams, and S. J. Goodman (1998), Global lightning: Total, cloud and ground flash estimates, *Journal of Geophysical Research: Atmospheres*, *103*(D16), 19,791–19,809.

Mansell, E. R., D. R. MacGorman, C. L. Ziegler, and J. M. Straka (2002), Simulated three-dimensional branched lightning in a numerical thunderstorm model, *J. Geophys. Res.*, *107*(D9), 4075, doi:10.1029/2000JD000244.

Mansell, E. R., C. L. Ziegler, and E. C. Bruning (2010), Simulated electrification of a small thunderstorm with two-moment bulk microphysics, *Journal of the Atmospheric Sciences*, *67*(1), 171–194.

Markson, R. (1976), Ionospheric potential variations obtained from aircraft measurements of potential gradient, *Journal of Geophysical Research*, *81*(12), 1980–1990.

Marshall, T. C., and W. D. Rust (1991), Electric field soundings through thunderstorms, *J. Geophys. Res.*, *96*, 22,297–22,306.

Marshall, T. C., M. P. McCarthy, and W. D. Rust (1995), Electric field magnitudes and lightning initiation in thunderstorms, *J. Geophys. Res.*, *100*(D4), 7097–7104, doi:10.1029/95JD00020.

Melnikov, V. M., and R. J. Doviak (2009), Turbulence and wind shear in layers of large doppler spectrum width in stratiform precipitation, *Journal of Atmospheric and Oceanic Technology*, *26*(3), 430–443.

Meyer, T. C., T. J. Lang, S. A. Rutledge, W. A. Lyons, S. A. Cummer, G. Lu, and D. T. Lindsey (2013), Radar and lightning analyses of gigantic jet-producing storms, *J. Geophys. Res. Atmos.*, *118*(7), 2872–2888, doi:10.1002/jgrd.50302.

Meyr, H., M. Moeneclaey, and S. Fechtel (1997), *Digital communication receivers: synchronization, channel estimation, and signal processing*, John Wiley & Sons, Inc.

Mitra, S. K., and J. F. Kaiser (1993), *Handbook for digital signal processing*, John Wiley & Sons, Inc.

Murphy, M. J., A. Nag, J. A. Cramer, and A. E. Pifer (2014), Enhanced cloud lightning performance of the us national lightning detection network following the 2013 upgrade, in *23rd International Lightning Detection Conference & 5th International Lightning Meteorology Conference*, pp. 18–21.

Nag, A., and V. A. Rakov (2009), Some inferences on the role of lower positive charge region in facilitating different types of lightning, *Geophysical Research Letters*, *36*(5).

Nag, A., S. Mallick, V. Rakov, J. Howard, C. Biagi, D. Hill, M. Uman, D. Jordan, K. Rambo, J. Jerauld, et al. (2011), Evaluation of nldn performance characteristics using rocket-triggered lightning data acquired in 2004–2009, *J. Geophys. Res*, *116*, D02,123.

Orville, R., and L. Salanave (1970), Lightning spectroscopy–photographic techniques, *Applied optics*, *9*(8), 1775–1781.

Orville, R. E. (1968a), A high-speed time-resolved spectroscopic study of the lightning return stroke: Part i. a qualitative analysis, *Journal of the Atmospheric Sciences*, *25*(5), 827–838.

Orville, R. E. (1968b), A high-speed time-resolved spectroscopic study of the lightning return stroke: Part ii. a quantitative analysis, *Journal of the Atmospheric Sciences*, *25*(5), 839–851.

Orville, R. E. (1968), Spectrum of the lightning stepped leader, *J. Geophys. Res.*, *73*, 6999–7008, doi:10.1029/JB073i022p06999.

Orville, R. E. (1975), Spectrum of the lightning dart leader, *Journal of the Atmospheric Sciences*, *32*(9), 1829–1837.

Orville, R. E. (1994), Cloud-to-ground lightning flash characteristics in the contiguous united states: 1989–1991, *Journal of Geophysical Research: Atmospheres*, *99*(D5), 10,833–10,841.

Orville, R. E. (2008), Development of the national lightning detection network, *Bulletin of the American Meteorological Society*, *89*(2), 180–190.

Pasko, V. P. (2010), Recent advances in theory of transient luminous events, *J. Geophys. Res.*, *115*, A00E35, doi:10.1029/2009JA014860.

Pasko, V. P., M. A. Stanley, J. D. Matthews, U. S. Inan, and T. G. Wood (2002), Electrical discharge from a thundercloud top to the lower ionosphere, *Nature*, *416*, 152–154, doi:10.1038/416152a.

Peterson, M., and S. Rudlosky (2018), The time evolution of optical lightning flashes, *Journal of Geophysical Research: Atmospheres*.

Peterson, M., W. Deierling, C. Liu, D. Mach, and C. Kalb (2017a), The properties of optical lightning flashes and the clouds they illuminate, *Journal of Geophysical Research: Atmospheres*, *122*(1), 423–442.

Peterson, M., S. Rudlosky, and W. Deierling (2017b), The evolution and structure of extreme optical lightning flashes, *Journal of Geophysical Research: Atmospheres*, *122*(24).

Peterson, M., S. Rudlosky, and W. Deierling (2018), Mapping the lateral development of lightning flashes from orbit, *Journal of Geophysical Research: Atmospheres*, *123*(17), 9674–9687.

Pickering, E. (1901), *Astrophys. J.*, *14*(367).

Poehler, H., and C. Lennon (1979), Lightning detection and ranging system (LDAR): System description and performance objectives, *Tech. rep.*, NASA TM-74105.

Poelman, D. R., W. Schulz, and C. Vergeiner (2013), Performance characteristics of distinct lightning detection networks covering belgium, *Journal of Atmospheric and Oceanic Technology, 30*(5), 942–951.

Prentice, S., and D. Mackerras (1977), The ratio of cloud to cloud-ground lightning flashes in thunderstorms, *Journal of Applied Meteorology, 16*(5), 545–550.

Prueitt, M. L. (1963), The excitation temperature of lightning, *J. Geophys. Res., 68*, 803–811, doi:10.1029/JZ068i003p00803.

Qu, H., P. Yuan, T. Zhang, and Z. Chang (2011), Analysis on the correlation between temperature and discharge characteristic of cloud-to-ground lightning discharge plasma with multiple return strokes, *Physics of Plasmas, 18*(1), 013,504.

Rakov, V. A., and M. A. Uman (2003), *Lightning: Physics and Effects*, Cambridge Univ. Press, Cambridge, U.K.; New York.

Riousset, J. A., V. P. Pasko, P. R. Krehbiel, R. J. Thomas, and W. Rison (2007), Three-dimensional fractal modeling of intracloud lightning discharge in a New Mexico thunderstorm and comparison with lightning mapping observations, *J. Geophys. Res.*, accepted.

Riousset, J. A., V. P. Pasko, and A. Bourdon (2010a), Air-density-dependent model for analysis of air heating associated with streamers, leaders, and transient luminous events, *J. Geophys. Res., 115*, A12321, doi:10.1029/2010JA015918.

Riousset, J. A., V. P. Pasko, P. R. Krehbiel, W. Rison, and M. A. Stanley (2010b), Modeling of thundercloud screening charges: Implications for blue and gigantic jets, *J. Geophys. Res.*, *115*, A00E10, doi:10.1029/2009JA014286.

Rison, W., R. J. Thomas, P. R. Krehbiel, T. Hamlin, and J. Harlin (1999), A GPS-based three-dimensional lightning mapping system: Initial observations in central New Mexico, *Geophys. Res. Lett.*, *26*(23), 3573–3576, doi:10.1029/ 1999GL010856.

Rudlosky, S. D., S. J. Goodman, K. S. Virts, and E. C. Bruning (2018), Initial geostationary lightning mapper observations, *Geophysical Research Letters*.

Rust, W. D., D. R. MacGorman, E. C. Bruning, S. A. Weiss, P. R. Krehbiel, R. J. Thomas, W. Rison, T. Hamlin, and J. Harlin (2005), Inverted-polarity electrical structures in thunderstorms in the severe thunderstorm electrification and precipitation study (STEPS), *Atmos. Res.*, *76*(1–4), 247–271.

Said, R., M. Cohen, and U. Inan (2013), Highly intense lightning over the oceans: Estimated peak currents from global gld360 observations, *Journal of Geophysical Research: Atmospheres*, *118*(13), 6905–6915.

Salanave, L. E. (1961), The optical spectrum of lightning, *Science*, *134*(3488), 1395–1399.

Schmit, T. J., P. Griffith, M. M. Gunshor, J. M. Daniels, S. J. Goodman, and W. J. Lebair (2017), A closer look at the abi on the goes-r series, *Bulletin of the American Meteorological Society*, *98*(4), 681–698.

Shao, X. M., and P. R. Krehbiel (1996), The spatial and temporal development of intracloud lightning, *J. Geophys. Res.*, *101*(D21), 26,641–26,668.

Slipher, V. M. (1917), The spectrum of lightning, *Lowell Obs. Bull. No 79, Flagstaff, Ariz., 55.*

Soula, S., O. Van Der Velde, J. Montanya, P. Huet, C. Barthe, and J. Bór (2011), Gigantic jets produced by an isolated tropical thunderstorm near réunion island, *Journal of Geophysical Research: Atmospheres, 116*(D19).

Stith, J. L. (1992), Observations of cloud-top entrainment in cumuli, *Journal of the atmospheric sciences, 49*(15), 1334–1347.

Su, H. T., R. R. Hsu, A. B. Chen, Y. C. Wang, W. S. Hsiao, W. C. Lai, L. C. Lee, M. Sato, and H. Fukunishi (2003), Gigantic jets between a thundercloud and the ionosphere, *Nature, 423*, 974–976, doi:10.1038/nature01759.

Tessendorf, S. A., S. A. Rutledge, and K. C. Wiens (2007), Radar and lightning observations of normal and inverted polarity multicellular storms from steps, *Monthly Weather Review, 135*(11), 3682–3706.

Thomas, R. J., P. R. Krehbiel, W. Rison, T. Hamlin, J. Harlin, and D. Shown (2001), Observations of vhf source powers radiated by lightning, *Geophysical research letters, 28*(1), 143–146.

Uman, M. (1966), Quantitative lightning spectroscopy, *IEEE, Spectr., 3*(8), 102–110, doi:10.1109/MSPEC.1966.5217654.

Uman, M. A. (1964), The peak temperature of lightning, *Journal of Atmospheric and Terrestrial Physics, 26*(1), 123–128.

Uman, M. A. (1974), The earth and its atmosphere as a leaky spherical capacitor, *American Journal of Physics, 42*(11), 1033–1035.

Uman, M. A. (2001), *The Lightning Discharge*, unabridged ed., Dover, Mineola, NY.

Uman, M. A., and R. E. Orville (1965), The opacity of lightning, *Journal of Geophysical Research*, *70*(22), 5491–5497.

Van Der Velde, O. A., J. Bór, J. Li, S. A. Cummer, E. Arnone, F. Zanotti, M. Füllekrug, C. Haldoupis, S. NaitAmor, and T. Farges (2010), Multi-instrumental observations of a positive gigantic jet produced by a winter thunderstorm in europe, *Journal of Geophysical Research: Atmospheres*, *115*(D24).

Vonnegut, B., C. Moore, R. Espinola, and H. Blau Jr (1966), Electric potential gradients above thunderstorms, *Journal of the Atmospheric Sciences*, *23*(6), 764–770.

Walker, T. D., and H. J. Christian (2017), Triggered lightning spectroscopy: Part 1. a qualitative analysis, *Journal of Geophysical Research: Atmospheres*, *122*(15), 8000–8011.

Walker, T. D., and H. J. Christian (2019), Triggered lightning spectroscopy: 2. a quantitative analysis, *Journal of Geophysical Research: Atmospheres*, *124*(7), 3930–3942.

Wang, P. K., S.-H. Su, M. Setvak, H. Lin, and R. M. Rabin (2010), Ship wave signature at the cloud top of deep convective storms, *Atmospheric Research*, *97*(3), 294–302.

Warner, T. A., R. E. Orville, J. L. Marshall, and K. Huggins (2011), Spectral (600-1050 nm) time exposures (99.6 μs) of a lightning stepped leader, *J. Geophys. Res. Atmos.*, *116*, D12210, doi:10.1029/2011JD015663.

Weiss, S. A., W. D. Rust, D. R. MacGorman, E. C. Bruning, and P. R. Krehbiel (2008), Evolving complex electrical structures of the steps 25 june 2000 multicell storm, *Monthly Weather Review*, *136*(2), 741–756.

Wiens, K. C., S. A. Rutledge, and S. A. Tessendorf (2005), The 29 june 2000 supercell observed during steps. part ii: Lightning and charge structure, *Journal of the atmospheric sciences*, *62*(12), 4151–4177.

Williams, E., and S. Heckman (2012), Polarity asymmetry in lightning leaders: The evolution of ideas on lightning behavior from strikes to aircraft, *AerospaceLab*, (5), p–1.

Williams, E. R. (1989), The tripole structure of thunderstorms, *Journal of Geophysical Research: Atmospheres*, *94*(D11), 13,151–13,167.

Williams, E. R. (2006), Problems in lightning physics–the role of polarity asymmetry, *Plasma Sources Sci. Technol.*, *15*(2), S91–S108, doi:10.1088/0963-0252/15/2/S12.

Winn, W. P., C. Moore, C. Holmes, and L. Byerley (1978), Thunderstorm on july 16, 1975, over langmuir laboratory: A case study, *Journal of Geophysical Research: Oceans*, *83*(C6), 3079–3092.

Winn, W. P., C. B. Moore, and C. R. Holmes (1981), Electric Field Structure in an active part of a small, isolated thundercloud, *J. Geophys. Res.*, *86*, 1187–1193.

Winn, W. P., G. D. Aulich, S. J. Hunyady, K. B. Eack, H. E. Edens, P. R. Krehbiel, W. Rison, and R. G. Sonnenfeld (2011), Lightning leader stepping, K changes, and other observations near an intracloud flash, *J. Geophys. Res.*, *116*, D23115, doi:10.1029/2011JD015998.

Witt, A., and S. P. Nelson (1991), The use of single-doppler radar for estimating maximum hailstone size, *Journal of Applied Meteorology*, *30*(4), 425–431.

Appendix A

AILLAE Python Code

Below is the Python code to that is loaded onto the Raspberry Pi to control the heavy-duty pelco motor.

```python
from datetime import datetime
import RPi.GPIO as GPIO
import time


Vp = 10.9                    #Rotational velocity of motor PAN in degrees/sec
Vt = 3.7                     #Rotational velocity of motor TILT in degrees/sec


GPIO.setmode(GPIO.BOARD)     #Refer to GPIO pins with pin numbers read from board
                                  #The following initializes GPIO pin outputs for each
direction
u = 29                       #u = Up
GPIO.setup(u, GPIO.OUT)


d = 31                       #d = Down
GPIO.setup(d, GPIO.OUT)


l = 32                       #l = left
GPIO.setup(l, GPIO.OUT)


r = 33                       #r = right
GPIO.setup(r, GPIO.OUT)


Az = 0                       #Initializes Az (azimuth in degrees) as 0. Camera must be pointing
                                  #North with motor turned fully counter-clockwise at
start up.
Alt = 30                     #Initializes Alt (altitude in degrees) as 30 **(Check average central
                                  #altitude(*Use lowest possible desired setting and
possibly make a hard stop there*))**. Camera must be at a 30 degree tilt at start up.


#Functions--------------------------------------------------------------
def Reset():                 #Function to reset camera to (Alt,Az)=(35,0). Does nothing if
already in this position.
    if (Alt!=30):
        print('Repositioning Altitude to 30 degrees. \n')
        Ontime=(int(Alt)-30)/int(Vt) #Time to tilt down to 35 degrees = degrees to tilt / rate of
tilt (possibly add 1 second to account for error? What issues does this cause, if any?)
            GPIO.output(d, GPIO.HIGH)        #Turn on 'down' pin
            time.sleep(Ontime)
            GPIO.output(d, GPIO.LOW)         #Turn off 'down' pin after waiting appropriate time.

    if (Az!=0):
        print('Repositioning Azimuth to 0 degrees. \n')
        Ontime = int(Az) / int(Vp)           #Time to pan left to North = degrees to pan / rate
of pan (possibly add 1 second to account for error? What issues does this cause, if any?)
```

```python
        GPIO.output(l, GPIO.HIGH)              #Turn on 'left' pin
        time.sleep(Ontime)
        GPIO.output(l, GPIO.LOW)               #Turn off 'left' pin after waiting appropriate time.

def Reposition():
    currenttime = [int(datetime.now().year) , '-' , int(datetime.now().month) , '-' ,
int(datetime.now().day) , ' ' , int(datetime.now().hour) , ':' , int(datetime.now().minute)]
    position = ['Alt: ' , Alt , '          ' , 'Az: ' , Az , '\n']
    my_file.write(str(currenttime))
    my_file.write('          ')
    my_file.write(str(position))
    my_file.write('\n')

    if (Alt!=30):
        Ontime = (int(Alt)-30) / int(Vt)            #Time to tilt up to desired altitude angle.
        GPIO.output(u, GPIO.HIGH)           #Turn on 'up' pin
        time.sleep(Ontime)
        GPIO.output(u, GPIO.LOW)             #Turn off 'up' pin after waiting appropriate time.

    if (Az!=0):
        Ontime = int(Az) / int(Vp)             #Time to pan right to desired azimuth angle.
        GPIO.output(r, GPIO.HIGH)           #Turn on 'right' pin
        time.sleep(Ontime)
        GPIO.output(r, GPIO.LOW)             #Turn off 'right' pin after waiting appropriate time.

#---------------------------------------------------------------------------

print('Welcome to AILLAE\'s RPi Control System. \n')       #add in all possible commands

my_file = open("positiondata.txt", "a")
w = 'Start'

while (w!='End'):                              #Allows user to input End for either Az or Alt in order to
terminate the program.

    print('Would you like to reposition the camera now or at a later time? (Up to 3 delayed
commands may be set.) \n')
    w = raw_input('Enter \'N\' for Now, \'L\' for Later, or \'End\' to Terminate Program: ')
    print('\n')

    if (w == 'N'):
        Altn = raw_input('Enter an altitude angle (in degrees) between 30 and 50: ')
        print('\n')
        Azn = raw_input('Enter an azimuth angle (in degrees) between 0 and 360: ')
```

```
        print('\n')

        if ((int(Az)>=0) and (int(Az)<=360) and (int(Alt)>=30) and (int(Alt)<=50)):
            Reset()
            Alt = Altn
            Az = Azn
            print('The camera will now move to an altitude of ', Alt, ' degrees and an azimuth
of ', Az, 'degrees... \n')
            Reposition()
            print('Repositioning complete. \n \n')

        elif ((int(Az)<0) or (int(Az)>360) or (int(Alt)<30) or (int(Alt)>50)):
            print('Invalid input. \n', 'Azimuth must be an integer between 0 and 360 degrees.
\n', 'Altitude must be an integer between 35 and 50 degrees. \n', 'Try again. \n \n')

    elif (w == 'L'):
        print('For delayed commands, the system must be left alone until the final command
has been completed. \n')
        c = raw_input('How many delayed repositioning commands would you like to set? (3
Max) ')

        if ((int(c)>3) or (int(c)<1)):
            print('Invalid number of commands. Try again. \n \n')

        else:
            print('\n \n', 'Position 1 \n')
            time1 = raw_input('Enter when to execute Command 1 (Enter as YYYY-MM-DD
HH:MM): ')        #Double MM ok?
            yr, mnth, day, hr, minute = time1.replace('-', ' ').replace(':', ' ').split()
            time1 = float(yr) + float(mnth)/12 + float(day)/365 + float(hr)/8760 +
float(minute)/525600
            print('\n')
            Alt1 = raw_input('Enter an altitude angle (in degrees) between 30 and 50: ')
            print('\n')
            Az1 = raw_input('Enter an azimuth angle (in degrees) between 0 and 360: ')
            print('\n \n')

            if ((int(Az1)>=0) and (int(Az1)<=360) and (int(Alt1)>=30) and (int(Alt1)<=50)):
                if (int(c)>1):
                    print('\n \n', 'Position 2 \n')
                    time2 = raw_input('Enter when to execute Command 2 (Enter as YYYY-
MM-DD HH:MM): ')
                    yr, mnth, day, hr, minute = time2.replace('-', ' ').replace(':', ' ').split()
```

```
                              time2 = float(yr) + float(mnth)/12 + float(day)/365 + float(hr)/8760 +
float(minute)/525600
                              print('\n')
                              Alt2 = raw_input('Enter an altitude angle (in degrees) between 30 and 50:
')
                              print('\n')
                              Az2 = raw_input('Enter an azimuth angle (in degrees) between 0 and 360:
')
                              print('\n \n')

                              if ((int(Az2)>=0) and (int(Az2)<=360) and (int(Alt2)>=30) and
(int(Alt2)<=50)):
                                    if (int(c)>2):
                                          print('\n \n', 'Position 3 \n')
                                          time3 = raw_input('Enter when to execute Command 3 (Enter as
YYYY-MM-DD HH:MM): ')
                                          yr, mnth, day, hr, minute = time3.replace('-', ' ').replace(':', '
').split()
                                          time3 = float(yr) + float(mnth)/12 + float(day)/365 +
float(hr)/8760 + float(minute)/525600
                                          print('\n')
                                          Alt3 = raw_input('Enter an altitude angle (in degrees) between
30 and 50: ')
                                          print('\n')
                                          Az3 = raw_input('Enter an azimuth angle (in degrees) between 0
and 360: ')
                                          print('\n \n')

                                          if ((int(Az3)<0) or (int(Az3)>360) or (int(Alt3)<30) or
(int(Alt3)>50)):
                                                print('Invalid input. \n', 'Azimuth must be an integer
between 0 and 360 degrees. \n', 'Altitude must be an integer between 35 and 50 degrees. \n',
'Time must be a 4-digit number between 0000 and 2359. /n', 'Try again. \n \n')

                              elif ((int(Az2)<0) or (int(Az2)>360) or (int(Alt2)<30) or (int(Alt2)>50)):
                                    print('Invalid input. \n', 'Azimuth must be an integer between 0 and
360 degrees. \n', 'Altitude must be an integer between 35 and 50 degrees. \n', 'Time must be a
4-digit number between 0000 and 2359. /n', 'Try again. \n \n')

                       elif ((int(Az1)<0) or (int(Az1)>360) or (int(Alt1)<30) or (int(Alt1)>50)):
                              print('Invalid input. \n', 'Azimuth must be an integer between 0 and 360
degrees. \n', 'Altitude must be an integer between 35 and 50 degrees. \n', 'Time must be a 4-
digit number between 0000 and 2359. /n', 'Try again. \n \n')
```

```
            print('Delayed commands are now set. The system will reset once the final
position has been reached. \n', 'Awaiting commands...')

            nowtime =
(float(datetime.now().year))+(float(datetime.now().month)/12)+(float(datetime.now().day)/365
)+(float(datetime.now().hour)/8760)+(float(datetime.now().minute)/525600)

            if (int(c)==1):
                while (nowtime<=time1):
                    if (nowtime==time1):
                        Reset()
                        Alt = Alt1
                        Az = Az1
                        Reposition()
                        print('Command 1 has been completed. \n')
                        time.sleep(60)

                nowtime =
(float(datetime.now().year))+(float(datetime.now().month)/12)+(float(datetime.now().day)/365
)+(float(datetime.now().hour)/8760)+(float(datetime.now().minute)/525600)

            elif (int(c)==2):
                while (nowtime<=time1) or (nowtime<=time2):
                    if (nowtime==time1):
                        Reset()
                        Alt = Alt1
                        Az = Az1
                        Reposition()
                        print('Command 1 has been completed. \n')
                        time.sleep(60)

                    elif (nowtime==time2):
                        Reset()
                        Alt = Alt2
                        Az = Az2
                        Reposition()
                        print('Command 2 has been completed. \n')
                        time.sleep(60)

                nowtime =
(float(datetime.now().year))+(float(datetime.now().month)/12)+(float(datetime.now().day)/365
)+(float(datetime.now().hour)/8760)+(float(datetime.now().minute)/525600)

            elif (int(c)==3):
```

```python
                    while (nowtime<=time1) or (nowtime<=time2) or (nowtime<=time3):
                        if (nowtime==time1):
                            Reset()
                            Alt = Alt1
                            Az = Az1
                            Reposition()
                            print('Command 1 has been completed. \n')
                            time.sleep(60)

                        elif (nowtime==time2):
                            Reset()
                            Alt = Alt2
                            Az = Az2
                            Reposition()
                            print('Command 2 has been completed. \n')
                            time.sleep(60)

                        elif (nowtime==time3):
                            Reset()
                            Alt = Alt3
                            Az = Az3
                            Reposition()
                            print('Command 3 has been completed. \n')
                            time.sleep(60)

                        nowtime =
(float(datetime.now().year))+(float(datetime.now().month)/12)+(float(datetime.now().day)/365
)+(float(datetime.now().hour)/8760)+(float(datetime.now().minute)/525600)

                    print('All delayed commands have been completed. \n \n')

my_file.close()

print('The system has been shut down.')
```